Spectral and Thermodynamical Properties of non-Hermitian Photon Gases

Emiel Slootman

UU Supervisors
prof. dr. Cristiane Morais Smith
dr. Rodrigo Arouca
Lumen Eek, MSc.

UT Supervisors
dr. Jan Klärs
prof. dr. Pepijn Pinkse

July, 2023

Abstract

We present a study of the spectral and thermodynamic properties of non-Hermitian photon gases, with a particular focus on the impact of loss engineering in tight-binding models. The scope of applications of these systems is multifold. First, we show theoretically and experimentally the existence of topological monomodes in non-Hermitian SSH models (in 1D and 2D) created by loss engineering. This challenges the idea that edge states always come in pairs in $\mathbb{Z}_2$ symmetry-protected topological systems [1]. Then we explore the quantum metric tensor, which gives a geometric interpretation to the Hilbert space in which states live. We produce phase diagrams for the given models and confirm that these are in agreement with known literature. Finally, we explore the occurrence of an imaginary time crystal phase in these systems, by studying the two-point correlation functions and the behaviour of thermodynamical properties. This analysis offers theoretical predictions that can be experimentally validated to confirm the existence of this intriguing phase of matter.

Contents

Chapter 1

Introduction

Conservation of energy is a criterion often demanded in physics. Energy can be transferred into other types of energy or even mass, but it cannot simply disappear. The physical laws used to describe nature are based on this principle. In quantum mechanics, this is done by making sure that the Hamiltonian is Hermitian. As a consequence, the eigenvalues of this operator are real, and energy is conserved. This poses a problem when studying a smaller system embedded in an environment with which it is interacting. To accurately describe the system, one cannot leave the environment out of the model. Depending on the environment and the type of interactions, this can greatly complicate the physics. As a solution, one can instead deal with non-Hermitian Hamiltonians. These act as an effective description of an open system because, in an open system, particles or energy can flow in and out, not conserving probability. As a result of non-Hermitian Hamiltonians, the states of the system acquire imaginary energies and finite lifetimes.

In addition to quantum mechanics, non-Hermitian components in their Hamiltonians also found wide application in different fields of physics, such as mechanics, where it provides a natural method of implementing friction [2]. Similarly, electronics has been used as a platform for realising non-Hermitian systems. For example, resistors have been used to model $\mathcal{PT}$-symmetry breaking [3] and diodes to model non-reciprocity [4]. In acoustics, gain and loss have been used to achieve unidirectional invisibility [5], meaning that the wave is supressed in one direction, but not in the other. It has also been used to create acoustic sensors to measure sound waves without perturbing the wave [6]. Even in biophysics non-Hermiticity has found its application, for example, in modelling non-reciprocal stochastic processes, where it has led to topological modes [7], it has also been used in population biology [8], and in relaxing connectivity constraints in artificial neural network [9].

In this thesis, we will focus on optical gain and loss systems. These systems are non-Hermitian because of the addition of gain and loss, and exhibit a complex spectrum. However, since loss is always present in optical systems. It makes more sense to consider only the loss as part of the model. Besides the previously outlined issues of complex energies and finite lifetimes, non-Hermitian Hamiltonians can also host a special phase: the imaginary time crystal [10]. Time crystals are a special phase of matter proposed by Wilczek and Shapere in 2012 [11]. This phase breaks time translation invariance, in the same way that a crystal breaks spatial translation invariance. Analogously to a crystal, this translation can be broken to a discrete translation invariance, characterized by persistent oscillations. In the same work that proposed the existence of quantum time crystals, Wilczek comments that due to the equivalence between time and imaginary time in the description of quantum systems, an imaginary time crystal could also be possible [10]. Imaginary time is a mathematical tool, often used in statistical field theory, to describe the thermodynamic behaviour of a quantum system [12], and is related to real time by $t = -i\tau$.

To this time, only two works have been done in imaginary time crystals. One by *Cai et al.* [13], which showed that an open system of hard-core bosons could host this phase. Another, by *Arouca et al.* [14],

considered the conditions for the appereance of this phase for a generic non-interacting non-Hermitian Hamiltonian, focusing on the Hatano-Nelson model. These imaginary time crystals were shown to oscillate at specific frequencies called *Matsubara frequencies*. Matsubara frequencies are a mathematical tool used in statistical field theory. They represent quantised frequencies in imaginary time. In statistical field theory, the Matsubara modes are used to solve integrals using the residue theorem [12]. However, the imaginary time crystal phase could act as a platform to measure the Matsubara frequencies of a system, revealing a physical truth to the seemingly mathematical construct.

In this work, we will study the properties of these optical gain and loss systems, specifically focusing on their spectrum. This will act as a foundation to further study the occurrence of the imaginary time crystal phase in these systems. To this aim, we will calculate properties that can be experimentally measured, in order to experimentally validate the existence of the imaginary time crystal phase and the Matsubara frequencies.

In order to have a good understanding of non-Hermitian quantum physics and the consequences it has, we will start with an introduction to the topic in Chapter 2. Here, we will show that eigenstates are no longer orthogonal when a matrix becomes non-Hermitian, and that instead we have to use a biorthogonal basis. We also introduce the notion of pseudo-Hermitian operators, and specifically $\mathcal{PT}$-symmetric operators, which play an important role in optical gain and loss systems. The notion of non-Hermitian physics will be introduced as an effective description of open quantum systems. Then, we will discuss exceptional points, which are special points in parameter space that occur in non-Hermitian systems. Finally, the Hatano-Nelson model will be discussed, which is also a non-Hermitian model, but due to a mechanism substantially different from the gain and loss systems.

After this, the thesis has been split into two parts. In the first part, we will discuss multiple aspects of the effect of gain and loss on the spectrum of tight-binding models. In Chapter 3, the spectra of different variations of tight-binding models with gain and loss will be discussed at length. The influence of the hopping strength compared to the gain and loss will be discussed, and we will characterise the parameter space of this model. We will also show how the boundary conditions influence the behaviour of the model. We will discuss a special case in Chapter 4, where we introduce the SSH model [15]. This model has (in 1D) two topologically protected edge states. We find that the addition of loss to the model can destroy one of these edge states. This is special because it has long been believed that in $\mathbb{Z}_2$ models, edge modes always come in pairs. This is shown for both the 1D SSH model and for the 2D SSH model. This chapter has been submitted for publication in *Nature Communications* [1]. In Chapter 5, a different method is considered to explore the parameter space of a model, namely the quantum geometric tensor. This method allows for the measurement of the distance between eigenstates in the Hilbert space using a different technique. Here, we produce a phase diagram, which we also found in Chapter 3. We do this for both the 1D and 2D SSH models. This part is also original research performed during this Master.

Part II focusses on the imaginary time crystal. In Chapter 6, it is shown how the gain and loss systems of part I lead to imaginary time crystal phases. Specifically, we calculate the Green's functions of the models. These can be interpreted as two-point correlation functions, which can be experimentally verified. We start by reproducing the result for the Hatano-Nelson model, followed by novel calculations for gain and loss systems. The chapter ends with a discussion of the thermodynamic effect of the imaginary time crystal phase. This manifests itself as an oscillation in thermodynamic quantities such as entropy and internal energy.

Chapter 2

Non-Hermitian Quantum Physics

Operators and their eigenvalues play an important role in quantum mechanics. One of these important operators is the Hamiltonian, which provides the total energy of a system. Its spectrum, the set of all of its eigenvalues, corresponds to the possible energy states of the system. In 'ordinary' quantum mechanics, observables, such as the energy of a system, are represented by Hermitian operators [16–20]. There are multiple reasons why we want to ensure that these operators are Hermitian. First, we want to ensure that the outcome of measurements are real, and not complex numbers. A Hermitian operator would guarantee this,

$$\left\langle \psi \middle| \hat{A}\psi \right\rangle = a \left\langle \psi | \psi \right\rangle = a^* \left\langle \psi | \psi \right\rangle = \left\langle \hat{A}\psi \middle| \psi \right\rangle = \left\langle \psi \middle| \hat{A}^\dagger \psi \right\rangle, \tag{2.1}$$

which results in A being Hermitian: $A^\dagger = A$. Second, if the operator is Hermitian, its eigenvectors will be orthogonal. When we perform a measurement on a system, we want the system to be in a distinct state. If the eigenvectors were not orthogonal, we would not be able to tell with certainty in which state the system is after the measurement. Hermiticity ensures this by

$$a_1 \left\langle \psi_1 | \psi_2 \right\rangle = \left\langle A\psi_1 | \psi_2 \right\rangle = \left\langle \psi_1 | A\psi_2 \right\rangle = a_2 \left\langle \psi_1 | \psi_2 \right\rangle \rightarrow (a_1 - a_2) \left\langle \psi_1 | \psi_2 \right\rangle = 0. \tag{2.2}$$

Because the eigenvalues a_1 and a_2 can be different in general, this means that the two states ψ_1 and ψ_2 must be orthogonal. Finally, a Hermitian Hamiltonian guarantees unitary time evolution. That is to say, we want the probability to be conserved over time [19, 20]. From the time-dependent Schrödinger equation,

$$i\hbar \frac{\partial}{\partial \mathfrak{t}} \left| \psi \right\rangle = \hat{H} \left| \psi \right\rangle,$$

where $\mathfrak{t}$ is time, we can determine the time evolution operator, which is given by $\hat{U} = e^{-\frac{i}{\hbar}\hat{H}\mathfrak{t}}$. Hence, the probability (as a function of time) is given by

$$\left| \left\langle \psi(\mathfrak{t}) | \psi(\mathfrak{t}) \right\rangle \right|^2 = \left| \left\langle \psi | \hat{U}^\dagger \hat{U} | \psi \right\rangle \right|^2 = \left| \left\langle \psi | e^{-\frac{i}{\hbar}\hat{H}\mathfrak{t}} e^{\frac{i}{\hbar}\hat{H}^\dagger \mathfrak{t}} | \psi \right\rangle \right|^2.$$

Thus, it is clear that this quantity is conserved if the Hamiltonian is Hermitian: $\hat{H} = \hat{H}^\dagger$.

So far, we have discussed why we would need operators to be Hermitian if they describe observables. Nevertheless, non-Hermitian Hamiltonians can also be a useful tool. Hermitian Hamiltonians describe closed quantum systems because the probability is conserved within the system. However, in reality, systems are rarely closed, especially when dealing with quantum states, where even the act of performing a measurement affects the system [19]. Accordingly, non-Hermitian quantum mechanics can be seen as a method of describing the quantum behaviour of an open system. In an open system, which is a system which interacts with an environment, particles can 'leak' in and out of the system, which means that

probability is not conserved. However, one has to keep in mind that the Hamiltonian of the full system still conserves probability and is Hermitian. Using non-Hermitian Hamiltonians to look at the system can be beneficial, as it can simplify calculations. It can also uncover new effects, such as the non-Hermitian skin effect, which we will discuss in Sec. 2.5. This effect depends on the boundary conditions of a system. A fundamental effect of non-Hermitian operators, which has not been explicitly mentioned until now, is that their spectrum can be imaginary. We can see this in Eq. (2.1), as the second equality then no longer holds. Later in this chapter, we will discuss the consequences of this.

We will start by presenting the basics of non-Hermitian quantum physics in Sec. 2.1. After this, we shall discuss pseudo-Hermitian systems in Sec. 2.2. Then, we will explain how one would obtain non-Hermitian Hamiltonians in Sec. 2.3 and exceptional points in Sec. 2.4. We will finish with a short overview of the Hatano-Nelson model in Sec. 2.5.

2.1 Biorthogonal Basis

A consequence of an operator being Hermitian is that the 'right' and 'left' eigenstates are directly related: they are Hermitian conjugates. Let $|\psi\rangle$ be an eigenstate of $\hat{\Lambda}$, where $\hat{\Lambda}$ is a Hermitian operator. Therefore, the eigenvalues of $\hat{\Lambda}$, λ, are real,

$$\hat{\Lambda} |\psi\rangle = \lambda |\psi\rangle .$$

Using this, we can directly relate the left and right eigenstates,

$$\langle\psi| \hat{\Lambda} = \left(\hat{\Lambda}^\dagger |\psi\rangle\right)^\dagger = \left(\hat{\Lambda} |\psi\rangle\right)^\dagger = (\lambda |\psi\rangle)^\dagger = \langle\psi| \lambda,$$

where in the last step we used the fact that the eigenvalues are real. Let us now consider the case of a non-Hermitian operator $\hat{X}$, with a right eigenstate $|\psi\rangle$

$$\hat{X} |\psi\rangle = \chi |\psi\rangle .$$

However, it is now unclear what happens if we apply the operator $\hat{X}$ to $|\psi\rangle^\dagger = \langle\psi|$.

$$\langle\psi| \hat{X} = \left(\hat{X}^\dagger |\psi\rangle\right)^\dagger ,$$

because $\hat{X} \neq \hat{X}^\dagger$. Therefore, $|\psi\rangle$ is not necessarily an eigenstate of $\hat{X}^\dagger$. This is a problem, because how can you calculate observable properties if you cannot calculate any expectation values? The left and right eigenstates of the operator are also no longer related. For Hermitian operators, as we saw in Eq. (2.2), the different eigenstates of a system are orthogonal to each other. This equation no longer holds for non-Hermitian operators, because $\chi_1 \langle\psi_1|\psi_2\rangle \neq \chi_2 \langle\psi_1|\psi_2\rangle$ for $|\psi_1\rangle, |\psi_2\rangle$ both eigenstates of $\hat{X}$. The solution is the biorthogonal basis [17, 21]. In this basis, we make a distinction between the eigenstates of the operator, $\hat{X}$, and its Hermitian conjugate $\hat{X}^\dagger$. This results in a set of right eigenstates $|\psi\rangle^R$ and a set of left eigenstates $^L\langle\psi|$,

$$\hat{X} |\psi\rangle^R = \chi |\psi\rangle^R \rightarrow \left(\hat{X} |\psi\rangle^R\right)^\dagger = {}^R\langle\psi| \hat{X}^\dagger = {}^R\langle\psi| \chi^*$$

and

$$^L\langle\psi| \hat{X} = {}^L\langle\psi| \chi \rightarrow \left({}^L\langle\psi| \hat{X}\right)^\dagger = \hat{X}^\dagger |\psi\rangle^L = \chi^* |\psi\rangle^L .$$

We can also show that the right and left eigenstates are orthogonal to each other. Let $^L\langle\psi_1|$ and $|\psi_2\rangle^R$ be eigenstates of a non-Hermitian operator $\hat{X}$, with eigenvalues χ_1 and χ_2. Then,

$$^L\langle\psi_1| \hat{X} |\psi_2\rangle^R = \chi_2 {}^L\langle\psi_1|\psi_2\rangle^R = \chi_1 {}^L\langle\psi_1|\psi_2\rangle^R \rightarrow (\chi_2 - \chi_1) {}^L\langle\psi_1|\psi_2\rangle^R = 0 \rightarrow {}^L\langle\psi_1|\psi_2\rangle^R = 0.$$

Furthermore, the biorthogonal basis is also complete [17]:

$$\sum_{\{\psi\}} |\psi\rangle^{R}{}^{L}\langle\psi| = \mathbb{1}.$$

2.2 Pseudo-Hermitian

As we have discussed in the introduction to this chapter, non-Hermitian operators can have imaginary eigenvalues, but this is not necessarily the case. There exists a class of non-Hermitian matrices called pseudo-Hermitian. A matrix H is called pseudo-Hermitian if an η exists, such that [18, 22]

$$\hat{H}^\dagger = \eta \hat{H} \eta^{-1} \quad \text{where} \quad \eta = \eta^\dagger.$$

Such an η only exists if the eigenvalues of $\hat{H}$ are entirely real, or the complex eigenvalues come in conjugate pairs with the same degeneracy. In the case where η is an identity matrix, $\hat{H}$ is simply Hermitian. A way to construct η and η^{-1} is to consider the left and right eigenvectors of $\hat{H}$, $^L\langle\psi|$ and $|\psi\rangle^R$ [22]:

$$\eta = \sum_{\{\psi\}} |\psi\rangle^{LL}\langle\psi| \quad \text{and} \quad \eta^{-1} = \sum_{\{\psi\}} |\psi\rangle^{RR}\langle\psi|.$$

We can also restore a type of unitary time evolution with η. For this, we must introduce a slight modification to the time-dependent Schrödinger equation [22]

$$i\hbar \frac{\partial}{\partial \mathfrak{t}} |\psi\rangle^R = (\hat{H} + \hat{G}) |\psi\rangle^R \quad \text{with} \quad \hat{G} = -\frac{i\hbar}{2} g^{-1} \frac{\partial}{\partial \mathfrak{t}} g.$$

An added benefit of pseudo-Hermiticity is that the partition function

$$Z = \text{Tr}\left[e^{-\beta\hat{H}} \right]$$

remains real, because the imaginary parts of the conjugate complex eigenvalues cancel out. Since the partition function plays an important role in thermodynamics, it is convenient that this quantity remains fully real.

A particularly important subclass of pseudo-Hermitian operators are the $\mathcal{PT}$-symmetric operators. $\mathcal{P}$-symmetry is the invariance of the system under parity transformation: $(x, y, z) \rightarrow (-x, -y, -z)$ and $\mathcal{T}$-symmetry is the invariance of the system under time reversal: $\mathfrak{t} \rightarrow -\mathfrak{t}$. Therefore, $\mathcal{PT}$-symmetry is the invariance of a system under parity and time-reversal transformation. It turns out that $\mathcal{PT}$-symmetry is a more fundamental condition than Hermiticity [19, 22, 23], and has been proposed as a replacement for Hermiticity. If an operator has an unbroken $\mathcal{PT}$-symmetry, its spectrum is entirely real. However, the $\mathcal{PT}$-symmetry is spontaneously broken when the eigenvectors of the Hamiltonian are no longer eigenvectors of the $\mathcal{PT}$ operator [24]. In this case, the spectrum can have imaginary eigenvalues, which come in conjugated pairs.

There exists another subclass of non-Hermitian operators: the quasi-Hermitian operators. A non-Hermitian operator is quasi-Hermitian if there exists a positive definite operator η such that [18]

$$\eta \hat{H} = \hat{H}^\dagger \eta.$$

These quasi-Hermitian operators have a real spectrum.

2.3 Effective non-Hermitian Hamiltonians

2.3.1 Lindblad Formalism

A non-Hermitian Hamiltonian can be seen as an effective description of an open system via the Lindblad formalism. The Lindblad formalism is a method to study the behaviour of a system coupled to a bath. The full Hamiltonian of the system and bath is given by [25]

$$\hat{H} = \hat{H}_S \otimes \hat{I}_B + \hat{I}_S \otimes \hat{H}_B + \hat{H}_I.$$

Here, H_S is the Hamiltonian that acts only on the system, H_B is the Hamiltonian that acts only on the bath and H_I is the Hamiltonian which describes the interaction between the system and the bath. We first consider the density matrix [19, 25]

$$\hat{\rho} = |\psi(\mathbf{t})\rangle \langle \psi(\mathbf{t})| = e^{-\frac{i}{\hbar}\hat{H}\mathbf{t}} |\psi\rangle \langle\psi| e^{\frac{i}{\hbar}\hat{H}\mathbf{t}}.$$

If we simply take the time derivative of this equation, we arrive at the von Neumann equation (dropping the time labels for convenience)

$$\frac{\mathrm{d}}{\mathrm{d}\mathbf{t}}\hat{\rho} = -\frac{i}{\hbar}\left[\hat{H}, \hat{\rho}\right].$$

This equation describes the time evolution of the density matrix and is analogous to the time-dependent Schrödinger equation. We can trace out the bath to obtain an expression for the system

$$\frac{\mathrm{d}}{\mathrm{d}\mathbf{t}}\hat{\rho}_S = \mathrm{Tr}_B\left\{-\frac{i}{\hbar}\left[\hat{H}, \hat{\rho}\right]\right\}.$$

Now, to simplify this expression, we need to make a few assumptions. For example, we need to assume that the time-dependent part of the total Hamiltonian is only in the system and not in the bath. We also need to assume the Markov approximation and the rotating-wave approximation [19]. This results in

$$\frac{\mathrm{d}}{\mathrm{d}\mathbf{t}}\hat{\rho}_S = -\frac{i}{\hbar}\left[\hat{H}_S, \hat{\rho}_S\right] + \mathcal{D}(\hat{\rho}_S) \quad \text{with} \quad \mathcal{D}(\hat{\rho}_S) = \sum_i \left(\hat{L}_i\hat{\rho}_S\hat{L}_i^\dagger - \frac{1}{2}\left\{\hat{L}_i^\dagger\hat{L}_i, \hat{\rho}_S\right\}\right). \tag{2.3}$$

This is the so-called Lindblad master equation, or the GKSL (Gorini-Kossakowski-Sudarshan-Lindblad) master equation. $\mathcal{D}(\rho_S)$ is called the dissipator, and $\hat{L}_i$ are the so-called jump operators. The Lamb shift is omitted here. By rearranging the terms in Eq. (2.3), the connection between non-Hermitian Hamiltonians and the Lindblad master equation can be made clear [19]:

$$\frac{\mathrm{d}}{\mathrm{d}\mathbf{t}}\hat{\rho}_S = -\frac{i}{\hbar}\left(\hat{H}_{eff}\hat{\rho}_S - \hat{\rho}_S\hat{H}_{eff}^\dagger\right) + \sum_i \hat{L}_i\hat{\rho}_S\hat{L}_i^\dagger \quad \text{with} \quad \hat{H}_{eff} = \hat{H}_S - \frac{i\hbar}{2}\sum_i \hat{L}_i^\dagger\hat{L}_i. \tag{2.4}$$

We can see that if we drop the last term of Eq. (2.4), we obtain the von Neumann equation for a non-Hermitian Hamiltonian. For this reason, a non-Hermitian Hamiltonian can be used to describe an open system. This description remains an effective description, which means that it is only useful when we keep in mind that the system is interacting with its environment and explain the effect of the environment within this frame of reference.

2.3.2 Self-Energy

A different way to obtain non-Hermitian Hamiltonians is by looking at a description for quasi-particles with a limited lifetime. Our starting point will be the retarded Green's function [26]

$$G^R = (\omega - H_0 - \Sigma)^{-1}.$$

Here, $\hat{H}_0$ is the single-electron Hamiltonian, which is Hermitian. Σ is the self-energy of the electron, describing electron-electron interactions, electron-phonon interactions, and the scattering of the electron on impurities. Our aim is to find a description of the quasiparticle that incorporates these effects of the self-energy. The imaginary part of the spectrum encodes information about the lifetime of the quasiparticle. Therefore, if the quasiparticle has a finite lifetime, the self-energy is non-Hermitian. From this Green's function, we can define a Hamiltonian for the quasiparticle

$$H = H_0 + \Sigma.$$

This results in an effective non-Hermitian Hamiltonian describing quasiparticles with a finite lifetime.

2.4 Exceptional Points

An important aspect of non-Hermitian physics that we have not mentioned thus far is the existence of exceptional points. Exceptional points are points in the parameter space where two or more *eigenvalues and their corresponding eigenvectors* coalesce [18, 19, 21, 27]. This means that at these points the Hamiltonian is no longer diagonalisable, and the eigenvectors no longer span the Hilbert space. An example is the Hamiltonian [21]

$$H = \left(\begin{array}{cc} 0 & \alpha \\ 1 & 0 \end{array} \right), \quad \alpha \in \mathbb{C}. \tag{2.5}$$

The Hamiltonian of Eq. (2.5) is clearly non-Hermitian. It has two eigenvalues, which are equal to $E_\pm = \pm\sqrt{\alpha}$. These eigenvalues can be imaginary, depending on the value of α. We can already see that the candidate for the exceptional point is $\alpha = 0$, since the eigenvalues coalesce for that value. To determine this, we must look at the eigenstates of the system. Since this is a non-Hermitian system, there are left and right eigenstates, as discussed in Sec. 2.1. The eigenvectors are given by

$$\psi_{R,\pm} = \left(\begin{array}{c} \pm\sqrt{\alpha} \\ 1 \end{array} \right) \quad \text{and} \quad \psi_{L,\pm} = \left(\begin{array}{cc} 1 & \pm\sqrt{\alpha} \end{array} \right),$$

and we indeed see that the eigenvectors coalesce at $\alpha = 0$. Thus, this is in fact an exceptional point. The fact that both the energies and eigenstates coalesce marks a generalisation of Hermitian degeneracies. The strong response close to exceptional points was used, among other things, to build sensors [28].
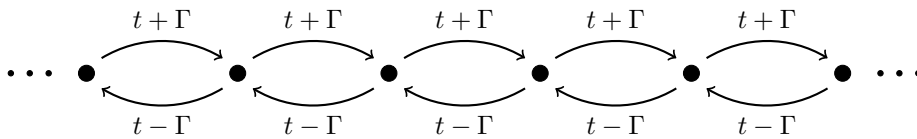
2.5 Hatano-Nelson Model

Figure 2.1: Illustration of the Hatano-Nelson model.

In this section, we will briefly discuss the Hatano-Nelson model, which describes one of the simplest non-Hermitian systems exhibiting non-reciprocity. The Hatano-Nelson model is a single-band tight-binding hopping model, where hopping to the left has a different amplitude than hopping to the right. The Hamiltonian of the Hatano-Nelson model is given by [14, 21, 29]

$$\hat{H} = -\sum_{j=0}^{N-1} \left[(t-\Gamma)\hat{c}_j^\dagger \hat{c}_{j+1} + (t+\Gamma)\hat{c}_{j+1}^\dagger \hat{c}_j \right]. \tag{2.6}$$

Here, t is the hopping parameter and Γ describes the non-reciprocity. In the case of periodic boundary conditions, we can diagonalise the Hamiltonian of Eq. (2.6) using a Fourier transform. The resulting spectrum is

$$\epsilon(k) = 2t\cos(ka) - 2\Gamma i \sin(ka).$$

Because the Hamiltonian of Eq. (2.6) is equivalent to a circular matrix, the eigenvectors ψ of Eq. (2.6) are given by Bloch waves [30]

$$\left[\psi_k^R \right]_j = e^{ikja} \quad \text{with} \quad k = \frac{2\pi m}{N}, \quad m, j = 0, 1, 2 \cdots N - 1.$$

Here, the wave vector k is the index for the different eigenvectors and the j's are the components of the eigenvector. It is also instructive to consider the case for open boundary conditions, as interesting effects

for non-Hermitian systems often appear for finite systems. For this, we write the Hamiltonian in matrix form

$$
H = \mathbf{c}^\dagger
\begin{pmatrix}
0 & -(t-\Gamma) & 0 & \cdots & 0 \\
-(t+\Gamma) & 0 & -(t-\Gamma) & & \\
0 & -(t+\Gamma) & 0 & \ddots & \vdots \\
\vdots & & \ddots & \ddots & -(t-\Gamma) \\
0 & & \cdots & -(t+\Gamma) & 0
\end{pmatrix}_{N \times N}
\mathbf{c}.
\tag{2.7}
$$

This is a tridiagonal Toeplitz matrix, for which the eigenvalues and eigenvectors are known [31]. For a general tridiagonal Toeplitz matrix A, we have

$$
A =
\begin{pmatrix}
a & d & & & \\
b & a & d & & \\
& b & \ddots & \ddots & \\
& & \ddots & \ddots & d \\
& & & b & a
\end{pmatrix}_{N \times N}
.
$$

The eigenvalues for this matrix are given by the equation

$$
\lambda = a + 2\sqrt{bd}\cos\left(\frac{m\pi}{N+1}\right) \quad \text{with} \quad m = 1, 2 \cdots N,
\tag{2.8}
$$

and the left and right eigenvectors read

$$
\left[\psi_m^R\right]_j = \sqrt{\frac{2}{N+1}}\left(\frac{b}{d}\right)^{j/2}\sin\left(\frac{mj\pi}{N+1}\right) \quad \text{and}
$$

$$
\left[\psi_m^L\right]_j = \sqrt{\frac{2}{N+1}}\left(\frac{d^*}{b^*}\right)^{j/2}\sin\left(\frac{mj\pi}{N+1}\right) \quad \text{with} \quad m, j = 1, 2 \cdots N.
\tag{2.9}
$$

Using the result of Eq. (2.8) and Eqs. (2.9) with the Hamiltonian of Eq. (2.7), we can determine the spectrum of the open Hatano-Nelson model,

$$
\epsilon_k = 2\sqrt{t^2 - \Gamma^2}\cos\left(\frac{m\pi}{N+1}\right) \quad \text{with} \quad m = 1, 2 \cdots N,
$$

and the right eigenvectors, which are given by

$$
\left[\psi_m^R\right]_j = \sqrt{\frac{2}{N+1}}\left(\frac{t+\Gamma}{t-\Gamma}\right)^{j/2}\sin\left(\frac{mj\pi}{N+1}\right) \quad \text{with} \quad m, j = 1, 2 \cdots N.
\tag{2.10}
$$

Let us now define the quantity [32]

$$
\kappa = \log\left(\sqrt{\frac{t-\Gamma}{t+\Gamma}}\right).
\tag{2.11}
$$

By substituting Eq. (2.11) into Eq. (2.10), we can rewrite the eigenstates for the Hatano-Nelson model

$$
\left[\psi_m^R\right]_j = \sqrt{\frac{2}{N+1}}e^{-\kappa j}\sin\left(\frac{mj\pi}{N+1}\right) \quad \text{with} \quad m, j = 1, 2 \cdots N.
\tag{2.12}
$$

Similary, for the left eigenstates this yields

$$
\left[\psi_m^L\right]_j = \sqrt{\frac{2}{N+1}}e^{\kappa j}\sin\left(\frac{mj\pi}{N+1}\right) \quad \text{with} \quad m, j = 1, 2 \cdots N.
\tag{2.13}
$$

Looking back at the Hamiltonian of the Hatano-Nelson model, Eq. (2.6), we see that hopping to the left is different from hopping to the right. When the system is open, one can expect this to result in an accumulation of states on one side of the chain. This is also what we see in Eqs. (2.12) and (2.13) due to the $e^{-\kappa j}$ and $e^{\kappa j}$ terms. This is an important aspect of non-reciprocal non-Hermitian systems, and is called the non-Hermitian skin effect (NHSE) [32–34]. Here, κ plays the role of the decay length for the accumulation of modes at the edge.
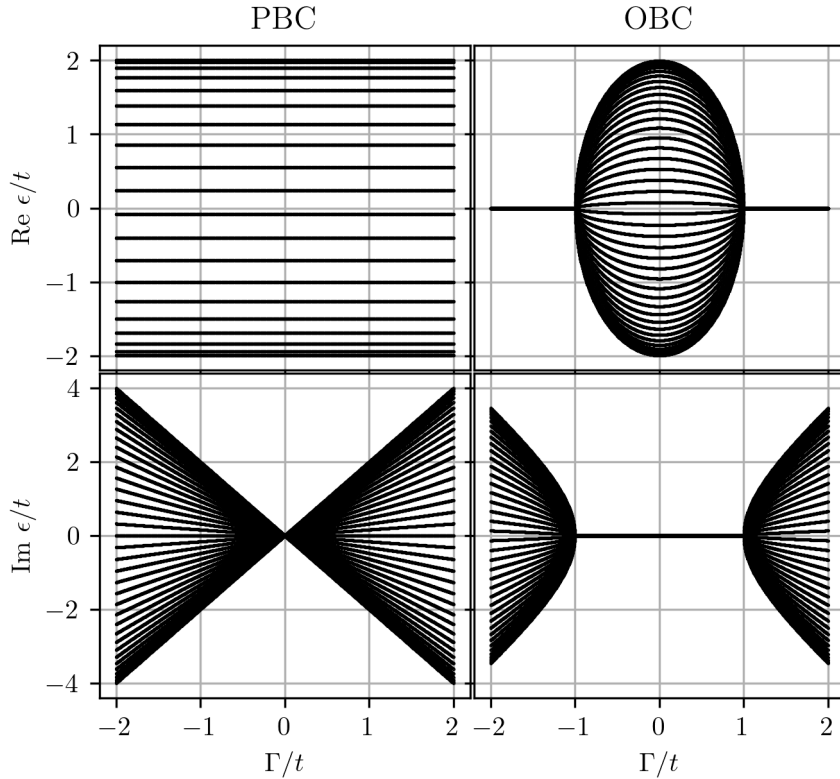
Figure 2.2: Real and imaginary part of the spectrum of the Hatano-Nelson model for periodic (PBC) and open (OBC) boundary conditions. The periodic case is plotted for 40 k-points (corresponding to a chain of length 40) and the open case is plotted for a chain with 40 sites.

In Fig. 2.2, we plot the spectrum of the Hatano-Nelson model as a function of Γ/t. Here, the real and imaginary parts of the spectrum are shown for both periodic and open boundary conditions. The two boundary conditions yield drastically different results. For open boundary conditions, we see a region in which the spectrum is entirely real and a region where the spectrum is entirely imaginary. This is different from the case with periodic boundary conditions, where the spectrum always has a real component and an imaginary component, which scales linearly with Γ/t. For open boundary conditions, we also see two points at which all eigenvalues become zero: $|\Gamma/t| = 1$. These are the exceptional points of the system. In Sec. 2.4, we discussed that at exceptional points, the eigenvalues and eigenstates coalesce. From the eigenstates in Eq. (2.10), we can also see that for $|\Gamma| = |t|$ the eigenstates coalesce. Additionally, we see that the imaginary parts of both spectra come in conjugated pairs. This would indicate that the Hatano-Nelson model is pseudo-Hermitian, thus leading to a fully real partition function.

Part I

Optical Gain and Loss Systems

Chapter 3

Gain and Loss Hamiltonians

In this chapter, we will investigate a different type of non-Hermitian Hamiltonian. In the previous chapter, we discussed the Hatano-Nelson model, where the non-Hermiticity is caused by non-reciprocity: hopping to the left has a different amplitude than hopping to the right. Here, the non-Hermiticty will be caused by gain and/or loss on the sites. As we can recall from the previous chapter, the Hamiltonian acts as the propagator of the system. A Hermitian Hamiltonian makes the propagation operator unitary, so probability is conserved. In the case of non-Hermiticity, we get eigenvalues which are imaginary and therefore cancel the i in the exponent of the propagator, resulting in decay or amplification of a state. When these imaginary terms are placed on the diagonal of the Hamiltonian, they correspond to gain and loss. We will start by considering systems with unit cells consisting of two lattice sites in Sec. 3.1. Here, we will discuss some general features and some variants of these systems. The spectra will be discussed in great detail. Afterwards, we will consider open systems with gain or loss near the edges in Sec. 3.2. Most of the results here are original.

3.1   Alternating Gain and Loss
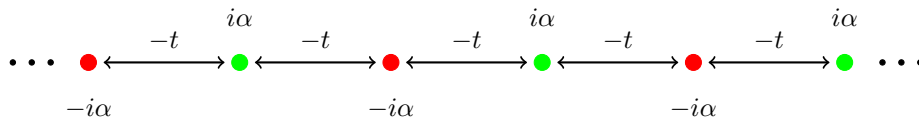
Figure 3.1: Tight binding chain with alternating gain and loss.

We will first investigate a dimerized system considering non-Hermitian physics: systems with alternating gain and loss [19, 27]. A visual representation of this system is shown in Fig. 3.1. It is a simple reciprocal tight-binding chain with gain or loss at the sites. The reason why these imaginary contributions on the sites lead to gain or loss can be explained straightforwardly by considering the time propagator:

$$U(\mathsf{t}) = e^{-\frac{i}{\hbar} \hat{H} \mathsf{t}},$$

where t is time. When this operator acts on an eigenstate of $\hat{H}$, $|\psi_n\rangle$, the state will evolve in time according to its eigenvalue

$$U(\mathsf{t}) |\psi\rangle = e^{-\frac{i}{\hbar} \epsilon_n \mathsf{t}} |\psi_n\rangle .$$

When there are losses at the hopping sites, the eigenvalues acquire a negative imaginary contribution. This will cause an exponential decay of the state, meaning loss. The Hamiltonian in matrix form is given

by

$$H = \mathbf{c}^\dagger \begin{pmatrix} -\alpha i & -t & 0 & \cdots & b \\ -t & \alpha i & -t & & \\ 0 & -t & -\alpha i & & \vdots \\ \vdots & & & \ddots & \\ b & & \cdots & & \alpha i \end{pmatrix} \mathbf{c}, \tag{3.1}$$

where b is $-t$ (0) for PBC (OBC). Here, $\mathbf{c}$ ($\mathbf{c}^\dagger$) are annihilation (creation) operators. Writing it in a different notation yields

$$\hat{H} = -\sum_{j=0}^{M-1} \left(t\hat{c}_{j+1}^\dagger \hat{c}_j + t\hat{c}_j^\dagger \hat{c}_{j+1} + \alpha i(-1)^j \hat{c}_j^\dagger \hat{c}_j \right). \tag{3.2}$$

Since the loss and gain alternate, the unit cell consists of two lattice sites. This also means that the entire system must always be composed of an even number of sites. We want to derive the spectrum of this system for PBC. Therefore, we first must write the Hamiltonian in terms of operators that act on a unit cell. We define $\hat{\psi}_j = (\hat{c}_{2j-1} \ \hat{c}_{2j})^T$. This yields,

$$\hat{H} = -\sum_{j=0}^{M/2-1} \left(\hat{\psi}_j^\dagger A \hat{\psi}_j + \hat{\psi}_{j+1}^\dagger B^\dagger \hat{\psi}_j + \hat{\psi}_j^\dagger B \hat{\psi}_{j+1} \right),$$

where $A = \begin{pmatrix} \alpha i & t \\ t & -\alpha i \end{pmatrix}$ and $B = \begin{pmatrix} 0 & 0 \\ t & 0 \end{pmatrix}$. After a Fourier transform, we are left with

$$\hat{H} = -\sum_{n=0}^{M/2-1} \left(Be^{-ik_n a} + B^T e^{ik_n a} + A \right) \hat{\psi}_{k_n}^\dagger \hat{\psi}_{k_n} = \sum_{n=0}^{M/2-1} h(k) \hat{\psi}_{k_n}^\dagger \hat{\psi}_{k_n},$$

where

$$h(k) = \begin{pmatrix} -\alpha i & -t(1 + e^{ik_n a}) \\ -t(1 + e^{-ik_n a}) & \alpha i \end{pmatrix}. \tag{3.3}$$

Finally, after diagonalising the matrix, we get

$$\epsilon(k) = \pm\sqrt{-\alpha^2 + 2t^2 + 2t^2 \cos(ka)}. \tag{3.4}$$

Fig. 3.2 shows the real and imaginary parts of the spectrum for different values of α/t. Notable here is that the spectrum becomes completely imaginary for $\alpha/t \geq 2$, which can be easily derived using Eq. (3.4). The spectrum becomes imaginary when the argument of the square root becomes negative. Therefore, the point where the entire spectrum is imaginary is

$$-\alpha^2 + 2t^2 + 2t^2 \cos(ka) = 0 \rightarrow \frac{\alpha}{t} = \sqrt{2 + 2\cos(ka)} \rightarrow \frac{\alpha}{t} = 2.$$

Here, we took $ka = 0$ because this is the point where the last eigenvalue turns imaginary. Another important fact is that the individual eigenvalues are either completely real or completely imaginary. This comes from the fact that there is a square root in Eq. (3.4), which either has a real result or an imaginary result for real arguments. Fig. 3.2 and Eq. (3.4) also make it clear that for every value of $\alpha > 0$, there is always a mode for which the energy is completely imaginary. At $ka = \pm\pi$, the spectrum is simply $\epsilon(k) = \pm\sqrt{-\alpha^2}$, which is imaginary for all $\alpha \neq 0$. Furthermore, the Hamiltonian of Eq. (3.2) and its eigenvectors are $\mathcal{PT}$-symmetric for some values of α/t. This means there is a region where the spectrum should be fully real and a region where there are complex eigenvalues in conjugated pairs. However, when we look at the spectrum in Fig. 3.2, we see that there is only a fully real spectrum for $\alpha = 0$, which is the Hermitian limit. Hence, the eigenvectors of Eq. (3.1) must not be eigenvectors of the
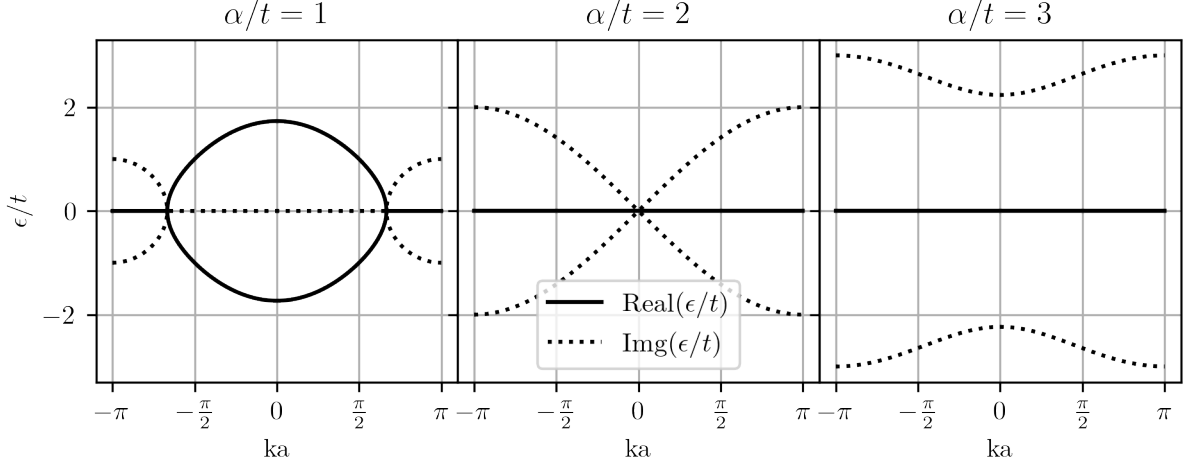
Figure 3.2: Behaviour of the spectrum for different values of α/t. Here, Eq. (3.1) is divided by t to obtain these results. The solid line is the real part of the spectrum, and the dotted line is the imaginary part.

$\mathcal{PT}$ operator for all $|\alpha| \neq 0$ [24]. To prove this, we first determine the right eigenvectors of Eq. (3.2), which are the eigenvectors of Eq. (3.3) multiplied by Bloch waves:

$$[\phi(k)]_{\pm,j} = \begin{pmatrix} \frac{i\alpha e^{ika} \pm \sqrt{e^{2ika}(-\alpha^2 + 2t^2 + 2t^2 \cos(ka))}}{t(1 + e^{ika})} \\ 1 \end{pmatrix} e^{ikaj} \quad \text{with} \quad j = 0, 1 \cdots \frac{M}{2} - 1. \tag{3.5}$$

We know from Sec. 2.2 that under $\mathcal{PT}$-symmetry we have $i \to -i$ and $k \to -k$. Every term in the above expression remains the same, except the $i\alpha e^{ika}$ term, which inverts its sign. So, this expression is only $\mathcal{PT}$-symmetric if $\alpha = 0$.

3.1.1 Broken $\mathcal{PT}$-symmetry

For a finite-size open system with a gain and loss structure like Eq. (3.1), the region where the spectrum remains real is larger than the single point $\alpha = 0$. As an example, we will consider a system consisting of two sites, with hopping t between the two sites and gain and loss α

$$H = \mathbf{c}^\dagger \begin{pmatrix} -i\alpha & -t \\ -t & i\alpha \end{pmatrix} \mathbf{c}. \tag{3.6}$$

The following reasoning also applies to systems larger than two sites, but we will only show it for this system since the other cases are too difficult to solve analytically. The Hamiltonian of Eq. (3.6) is non-Hermitian and $\mathcal{PT}$-symmetric. Its eigenvectors and eigenvalues are given by

$$\phi_\pm = \begin{pmatrix} -\frac{-i\alpha \pm \sqrt{t^2 - \alpha^2}}{t} \\ 1 \end{pmatrix} \quad \text{and} \quad \epsilon_\pm = \pm\sqrt{t^2 - \alpha^2}.$$

There is an exceptional point at $\alpha = t$ because, at this point, both eigenvalues are 0 and both eigenvectors are $\phi = \begin{pmatrix} i\alpha/t & 1 \end{pmatrix}^T$. For $\alpha < t$, the spectrum has fully real eigenvalues; if $\alpha > t$, it has fully imaginary eigenvalues in conjugated pairs. This suggests the $\mathcal{PT}$-symmetry is broken for $\alpha > t$. To prove this, we consider the eigenvectors. When $\alpha < t$ we have

$$\mathcal{PT}\phi_\pm = \mathcal{P}\begin{pmatrix} -\frac{i\alpha \pm \sqrt{t^2 - \alpha^2}}{t} \\ 1 \end{pmatrix} = \begin{pmatrix} 1 \\ -\frac{i\alpha \pm \sqrt{t^2 - \alpha^2}}{t} \end{pmatrix}.$$

Now we multiply the resulting vector by a constant to obtain

$$\mathcal{PT}\phi_\pm = \begin{pmatrix} -\frac{t}{i\alpha \pm \sqrt{t^2 - \alpha^2}} \\ 1 \end{pmatrix} = \begin{pmatrix} -\frac{-i\alpha \pm \sqrt{t^2 - \alpha^2}}{t} \\ 1 \end{pmatrix} = \phi_\pm,$$

so the eigenvectors are indeed $\mathcal{PT}$-symmetric. When $\alpha > t$, the eigenvectors are equal to

$$\phi_\pm = \begin{pmatrix} -\frac{-i\alpha \pm i\sqrt{\alpha^2 - t^2}}{t} \\ 1 \end{pmatrix}$$

and when we now apply the $\mathcal{PT}$ operators to it, we obtain

$$\mathcal{PT}\begin{pmatrix} -\frac{-i\alpha \pm i\sqrt{\alpha^2 - t^2}}{t} \\ 1 \end{pmatrix} = \mathcal{P}\begin{pmatrix} -\frac{i\alpha \mp i\sqrt{\alpha^2 - t^2}}{t} \\ 1 \end{pmatrix} = \begin{pmatrix} 1 \\ -\frac{i\alpha \mp i\sqrt{\alpha^2 - t^2}}{t} \end{pmatrix} \rightarrow \mathcal{PT}\phi_\pm = \begin{pmatrix} -\frac{t}{i\alpha \mp i\sqrt{\alpha^2 - t^2}} \\ 1 \end{pmatrix} \neq \phi_\pm.$$

We indeed find that the eigenvectors are no longer $\mathcal{PT}$-symmetric if $\alpha > t$, and thus the eigenvalues become complex. However, this $\mathcal{PT}$-symmetric region decreases as the system size increases. This indicates that the system behaves identically in the bulk in the thermodynamic limit compared to its periodic counterpart. We generally see this for systems without an NHSE, because an NHSE is due to an imaginary momentum term. Therefore, the bulk of systems with real momenta behaves similarly to the periodic system [35].

3.1.2 Exceptional Points

(a) Coalescence of the eigenvectors

(b) Eigenvalues for different α/t
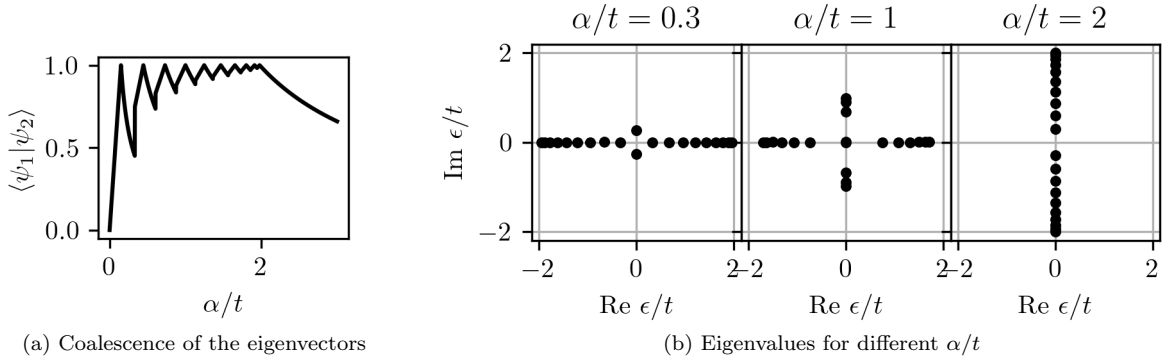
Figure 3.3: Overlap of eigenvectors and the spectrum for an open chain of 20 sites.

As discussed in the previous section, there are exceptional points in these types of systems. The occurrences of exceptional points are not limited to systems with OBC: They can also occur in systems with PBC. In this case, the eigenvectors of the *sublattice* must coalesce, as Bloch eigenvectors cannot coalesce. For the system of the Hamiltonian of Eq. (3.2), Fig. 3.2 shows that for $0 < \alpha/t < 2$, there are two points in the dispersion relation which have zero energy. We can readily see from Eq. (3.5) that at the points where the energy is zero ($\sqrt{-\alpha^2 + 2t^2 + 2t^2 \cos(ka)} = 0$), the two eigenvectors corresponding to the two zero modes reduce to

$$[\phi(k)]_{\pm,j} = \begin{pmatrix} \frac{ie^{ika}\alpha}{t(1+e^{ika})} \\ 1 \end{pmatrix} e^{ikaj} \quad \text{with} \quad j = 0, 1 \cdots \frac{M}{2} - 1.$$

The eigenvectors now coalesce because there is no longer a difference between the $+$ and $-$ eigenvectors. This is indeed an exceptional point. A critical note must be made here because the eigenvalues can only become zero if the required momentum is valid due to the quantisation. For instance, if we have a periodic system that is only 10 unit cells long, there are only 10 valid momenta. In that case, there is

not always an exceptional point for a general α/t in $0 < \alpha/t < 2$. This smoothly leads to open systems. There, we have a similar problem for open systems of finite size. This system has a dispersion relation similar to that of Fig. 3.2, only evaluated at discrete points. The dispersion relation for the open system given by Ref. [36] is equal to

$$\epsilon(\kappa) = \pm\sqrt{-\alpha^2 + 2t^2 + 2t^2\cos(\kappa)},$$

where κ is a solution to the equation

$$\sin(\kappa(N/2 + 1)) + \sin(\kappa N/2) = 0.$$

Such a system only has an exceptional point if the zero modes fall into the range of allowed values of k, for the Hamiltonian for that size. To show this, we investigate the coalescence of the eigenvectors belonging to the two eigenvalues closest to absolute zero. This can be seen in Fig. 3.3a. In the Hermitian limit ($\alpha = 0$), the eigenvectors are orthogonal, as they should be. When the system becomes non-Hermitian, they start to overlap. The system of this figure is 10 unit cells long, and we correspondingly see 10 peaks, where the eigenvectors entirely overlap, corresponding to the 10 pairs of eigenvalues in Fig. 3.3b becoming 0. An imaginary line gap opens for $\alpha/t > 2$, and the eigenvalues/vectors no longer coalesce. The jumps in Fig. 3.3a, which are not at the peaks, are caused by switching the eigenvalue pair. At these points, two new eigenvalues are closest to zero, and the corresponding wave-function overlap is calculated.

3.1.3 Systems with only Loss
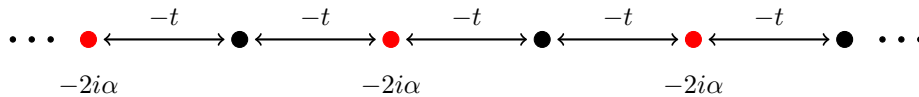
Figure 3.4: Tight-binding chain with only loss.

Up until this point, we have been considering systems with gain as well as loss. In an experimental setting, gain would be more difficult to engineer than loss, since loss is always present and gain requires active materials to amplify the signal. To adapt the theory to this, we can transform the system of Eq. (3.1) into a system with only loss by simply subtracting $i\alpha\mathbb{1}$ from it. This results in

$$H = \mathbf{c}^\dagger \begin{pmatrix} -2\alpha i & -t & 0 & \cdots & b \\ -t & 0 & -t & & \\ 0 & -t & -2\alpha i & & \vdots \\ \vdots & & & \ddots & \\ b & & \cdots & & 0 \end{pmatrix} \mathbf{c}, \tag{3.7}$$

where b is $-t$ (0) for PBC (OBC). After performing the same derivation as for Eq. (3.4), the dispersion relation for the PBC variant of Eq. (3.7) is given by

$$\epsilon(k) = \pm\sqrt{-\alpha^2 + 2t^2 + 2t^2\cos(ka)} - i\alpha.$$

This is the same dispersion relation as Eq. (3.4), but with an additional $-i\alpha$ term. The resulting spectrum for different values of α/t are depicted in Fig. 3.5. This is essentially the same spectrum as Fig. 3.2, but it is shifted down on the imaginary axis by a factor of α. Due to this, the system is no longer $\mathcal{PT}$-symmetric, as for a system with positive α, inverting time would now give the system a net gain. As a result, the eigenvalues do not come in complex conjugated pairs, but instead are centred around $-i\alpha$.
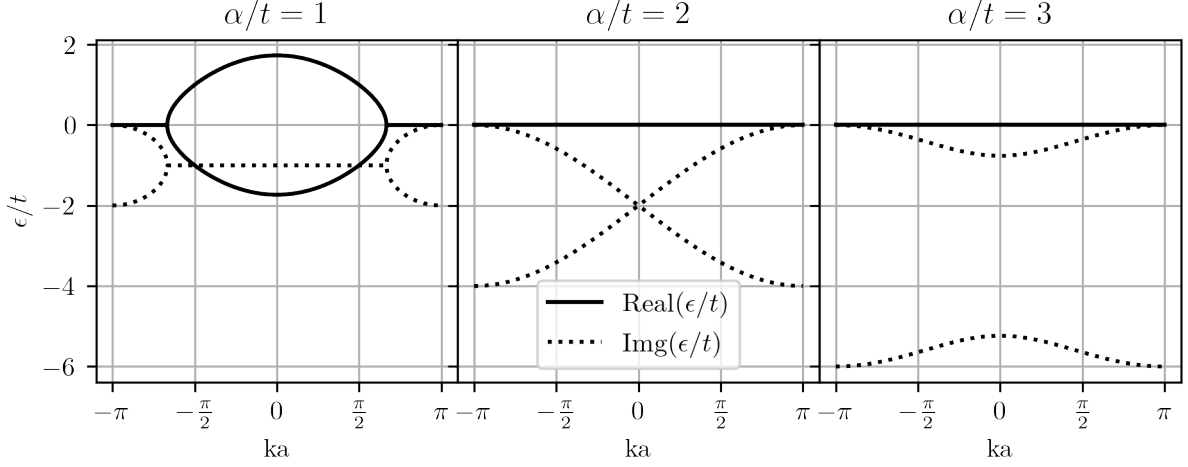
Figure 3.5: The behaviour of the spectrum for different values of α/t. Here, Eq. (3.7) is divided by t to obtain these results. The solid line is the real part of the spectrum, and the dotted line is the imaginary part.
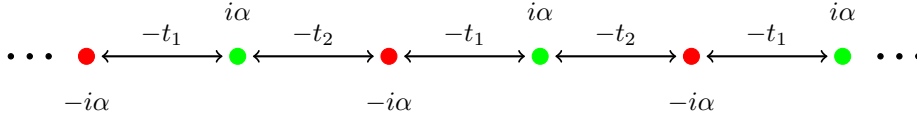
3.1.4 Non-Hermitian SSH Model

Figure 3.6: SSH chain with alternating gain and loss.

The SSH, or Su-Schrieffer-Heeger model, is a simple two-band model. It is a tight-binding model with two atoms in the unit cell. The hopping between the atoms in the unit cell and between atoms in neighbouring unit cells is different in the SSH model. It was originally intended to model the dimerisation of polyacetylene [15]. We can also apply gain and loss to this system, resulting in the system illustrated in Fig. 3.6. There are two distinct regimes for the SSH system. When $t_1 < t_2$, the system is in the topological regime. We will treat this case in more detail in the next chapter. In this section, we will study the trivial regime when $t_2 < t_1$. When $t_1 = t_2$, we restore the tight-binding chain of Fig. 3.1. The corresponding Hamiltonian for PBC is given by

$$\hat{H} = - \sum_{j=0}^{M/2-1} \left[\hat{\psi}_j^\dagger \begin{pmatrix} i\alpha & t_1 \\ t_1 & -i\alpha \end{pmatrix} \hat{\psi}_j + \hat{\psi}_{j+1}^\dagger \begin{pmatrix} 0 & t_2 \\ 0 & 0 \end{pmatrix} \hat{\psi}_j + \hat{\psi}_j^\dagger \begin{pmatrix} 0 & 0 \\ t_2 & 0 \end{pmatrix} \hat{\psi}_{j+1} \right], \tag{3.8}$$

where again $\hat{\psi}_j = (\hat{c}_{j,1} \ \hat{c}_{j,2})^T = (\hat{c}_{2j-1} \ \hat{c}_{2j})^T$. The resulting spectrum is

$$\epsilon(k) = \pm\sqrt{-\alpha^2 + t_1^2 + t_2^2 + 2t_1 t_2 \cos(ka)}$$

and it is plotted in Fig. 3.7. This spectrum has a real line gap for some α/t_1 values. This band gap closes for increasing α/t_1, after which an imaginary line gap opens. The real line gap closes when the spectrum at $ka = \pm\pi$ becomes zero at $|\alpha| = |t_1 - t_2|$. The imaginary gap opens when $|\alpha| = |t_1 + t_2|$. This means that the system has a $\mathcal{PT}$-symmetric region in parameter space, which is size-independent. If $|\alpha| < |t_1 - t_2|$, the system is $\mathcal{PT}$-invariant for PBC.
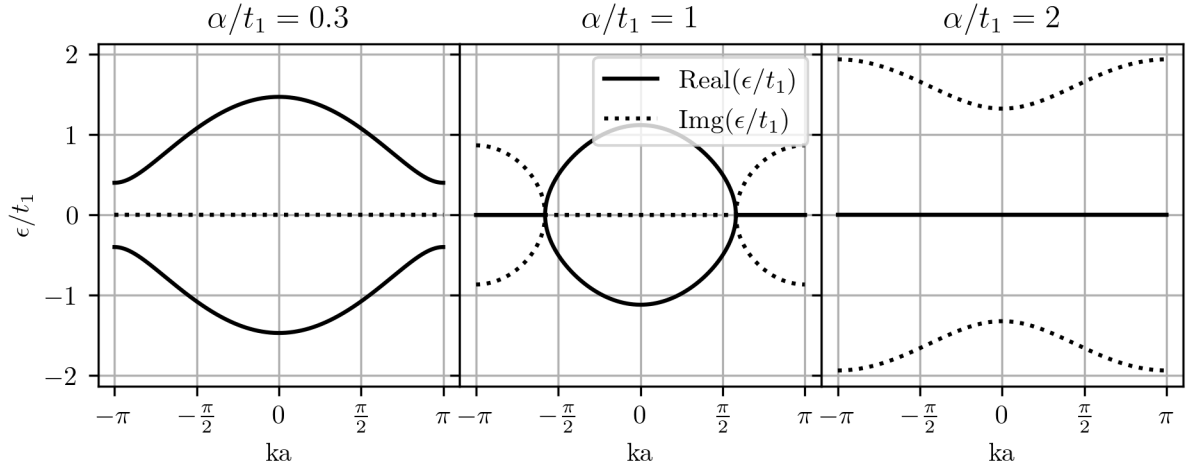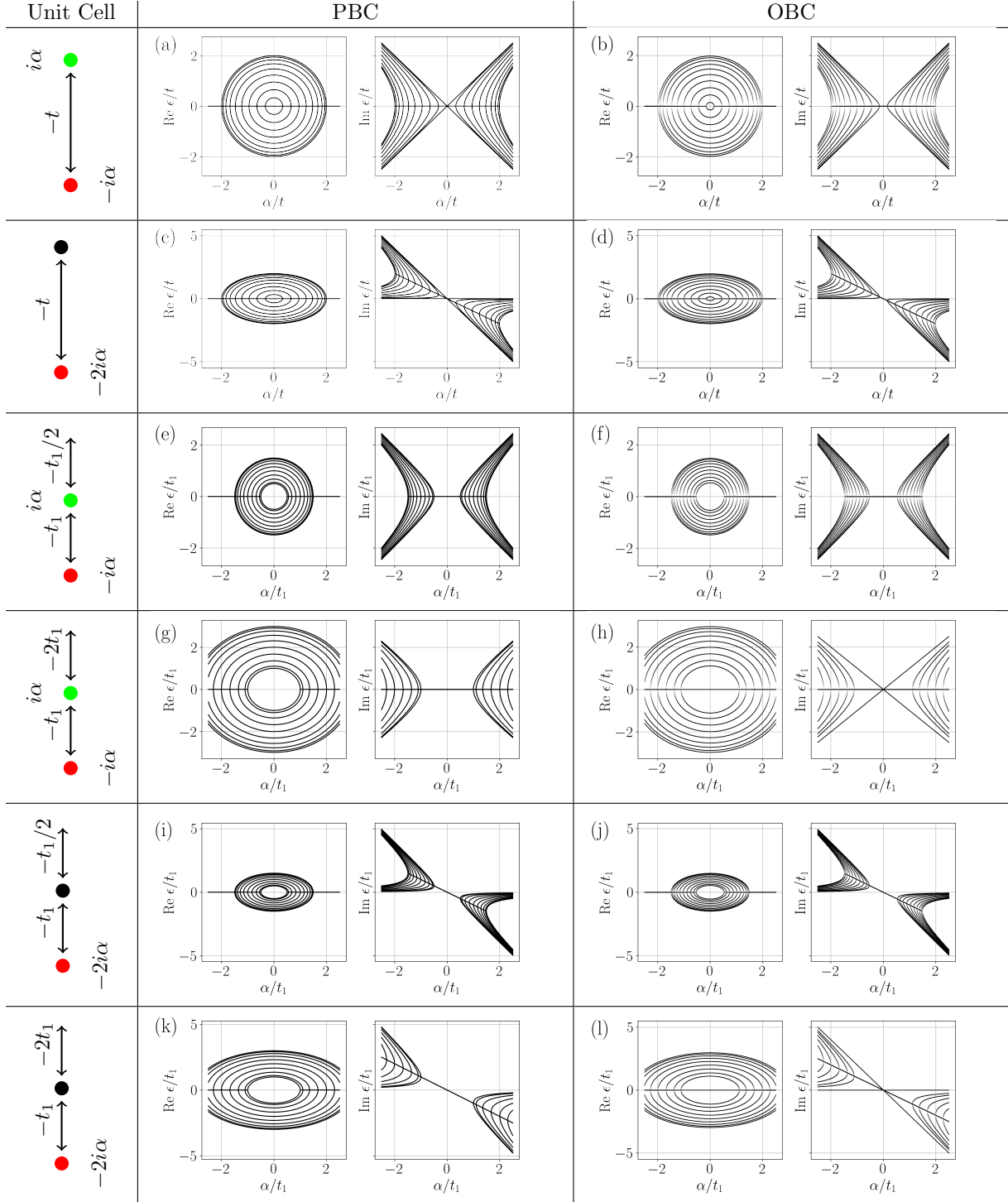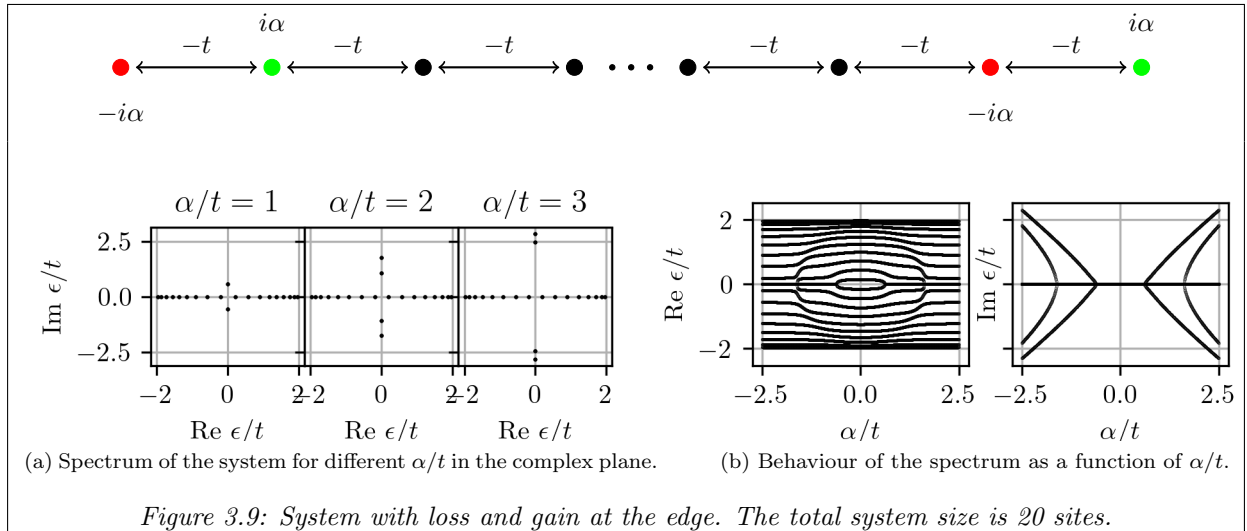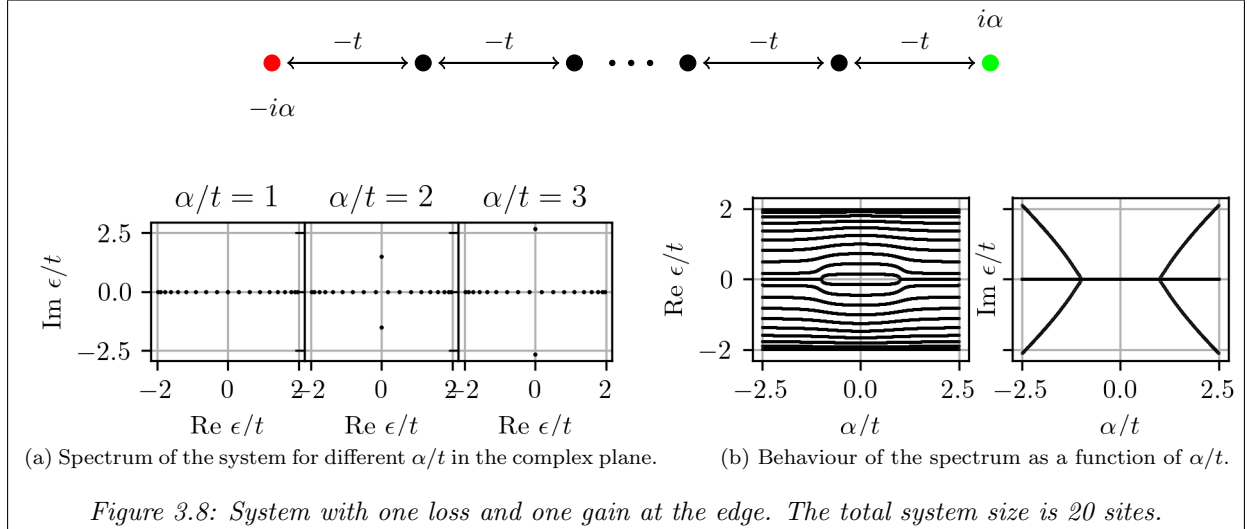
Figure 3.7: The behaviour of the PBC spectrum for different values of α/t. Here, Eq. (3.8) is divided by t_1 to obtain these results and $t_2 = t_1/2$. The solid line is the real part of the spectrum, and the dotted line is the imaginary part.

In table 3.1, we give an overview of the behaviour of the spectrum as a function of α/t for the different variants of gain/loss systems with two sites in the unit cell, for both PBC and OBC.

Table 3.1: *Real and imaginary part of the spectrum for all the different models investigated for different α/t with a unit cell containing two sites. The systems with only loss (as opposed to loss and gain) have a different y-axis range to fit the lopsided spectrum. All spectra are computed for a system size of 20 sites (10 unit cells).*

3.2 Gain and Loss at the Edge

(a) Spectrum of the system for different α/t in the complex plane.

(b) Behaviour of the spectrum as a function of α/t.

Figure 3.8: System with one loss and one gain at the edge. The total system size is 20 sites.

(a) Spectrum of the system for different α/t in the complex plane.

(b) Behaviour of the spectrum as a function of α/t.

Figure 3.9: System with loss and gain at the edge. The total system size is 20 sites.

Instead of introducing gain and loss at every site, we may also introduce gain and loss only near the system's boundary. An example can be seen in Fig. 3.8. Here, on one side of the chain there is one loss site, and on the other, there is one gain site. This results in one pair of complex conjugated eigenvalues for sufficiently large α/t values. When we add a loss and gain pair to the edges, as seen in Fig. 3.9, the system now hosts two complex conjugated pairs of eigenvalues. The two pairs correspond to different exceptional points at which they become imaginary. We get a new complex conjugated pair of eigenvalues for every gain and loss pair we add to the chain (for particular values of α/t). When we do not add the loss and gains in pairs, but instead add two loss sites at one edge and two gain sites at the other, the spectrum becomes different from the one presented thus far. This can be seen in Fig. 3.10. The eigenvalues still come in complex conjugated pairs, but are no longer entirely imaginary and acquire a real part. The real parts are precisely opposite in sign. These three systems are still $\mathcal{PT}$-symmetric. A system can also be

fabricated with two loss sites and two gain sites near the edge, which is not $\mathcal{PT}$-symmetric. This system can be seen in Fig. 3.11. Now, most eigenvalues get a small imaginary component, but four of them get a significant imaginary component, as seen in Fig. 3.11b. When increasing α/t, the first two eigenvalues move into the negative imaginary direction. After a while, again, two eigenvalues move in the positive imaginary direction.

(a) Spectrum of the system for different α/t in the complex plane.

(b) Behaviour of the spectrum as a function of α/t.

Figure 3.10: System with two losses and two gains at the edge. The total system size is 20 sites.

(a) Spectrum of the system for different α/t in the complex plane.

(b) Behaviour of the spectrum as a function of α/t.

Figure 3.11: System with opposite loss and gain at the edge. The total system size is 20 sites.

Chapter 4

Topological Monomode

This chapter is based on the manuscript E. Slootman, W. Cherifi, L. Eek, R. Arouca, E. J. Bergholtz, M. Bourennane, and C. Morais Smith, Topological Monomodes in Non-Hermitian Systems, arXiv:2304.05748 [1].

4.1 Introduction

Although the notion of topology has already appeared multiple times in this thesis, now we will introduce the concept more in detail. Topology in condensed-matter physics is mostly concerned with the band structure of materials. In solid-state physics, we often make the distinction between three separate classifications. There are the insulators, which are materials that are not conductive. They have a relatively large gap, in which the Fermi energy is positioned, such that there are no available conductive states. Furthermore, there are metals, which are conductive. In metals, the Fermi energy is located inside a band, so that there is no gap between valence and conduction states. Finally, there are the semi-conductors, which, play a vital role in modern electronics. They are like insulators in that the Fermi energy is located in a gap, but the size of the gap is considerably smaller, so that, for a suitable bias voltage, they become conductive. Topology in condensed matter adds a fourth category to it, namely the *topological insulators*. These types of materials are insulating in the bulk but have conductive edge states, meaning that electrons can flow around the edges of the material [37, 38].

In the field of topological condensed-matter physics, a fundamental concept is the existence of edge states, which are associated with a topological invariant [37], through the bulk boundary correspondance [38]. This topological invariant remains unchanged under adiabatic variations of the system's Hamiltonian. We associate this topological invariant to the bulk of the material, which allows for prediction of the edge states. Importantly, this topological invariant remains fixed as long as the parameters of the Hamiltonian are varied adiabatically [37]. However, if the gap closes in the Hamiltonian, the topological invariant changes, indicating a transition between different phases. This closing of the gap is crucial to distinguish between a topological phase and a trivial phase. A trivial phase lacks any non-trivial topological properties and typically exhibits a fully gapped energy spectrum. On the other hand, a topological phase possesses gapless or partially filled edge states that cannot be removed by adiabatic deformations without closing the energy gap [37]. This robustness of the edge states to deformations highlights the topological nature of the material and sets it apart from its trivial counterpart.

As mentioned before, one of the best known topological models is the SSH model [15]. The SSH model has two topologically protected edge modes in the topological phase. These edge modes sit in the middle of the band gap at zero energy. They can be characterised by a topological invariant, which in this case is called the winding number. In the case of the SSH model, this is a so-called $\mathbb{Z}_2$ topological constant,
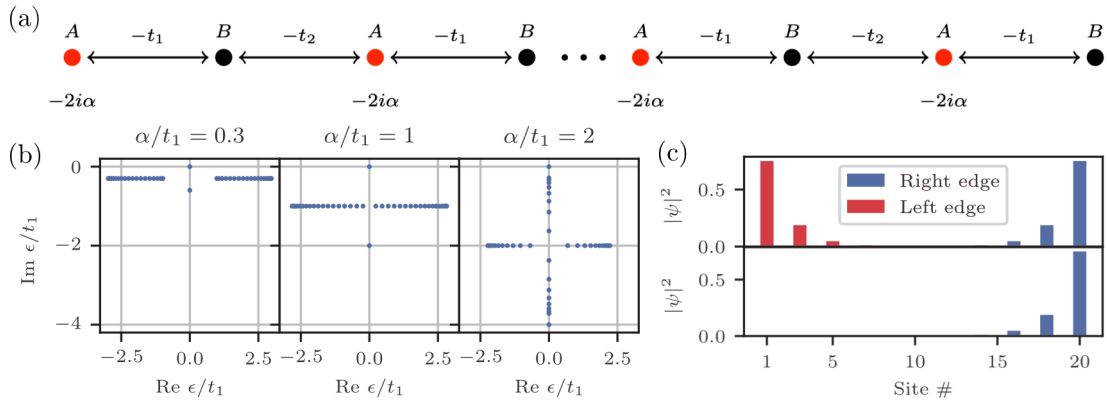
Figure 4.1: Theoretical description of an SSH chain with loss. (a) The lattice of Eq. (4.1). (b) Spectrum of the SSH model with alternating loss for OBC in the topological regime $t_2 = 2t_1$. The system consists of 40 lattice sites. The energies are shown in the complex plane, for different values of α/t_1. (c) Time evolution of the eigenstates of the Hamiltonian given by Eq. (4.1). Here, the system has 20 lattice sites. The two edge modes for $t_2/t_1 = 2$ and $\alpha/t_1 = 2$ are depicted at $\mathfrak{t} = 0$ ($\hbar/t_1$) and at $\mathfrak{t} = 10$ ($\hbar/t_1$). Figure taken from Ref. [1].

protected by chiral and inversion symmetry, meaning that it can take two integer values, being 1 in the topological phase and 0 in the trivial phase.

In this chapter, we explore how the addition of loss to this model can destroy one of the edge modes. We show that topological zero-energy monomodes can be engineered in non-Hermitian systems when losses are introduced in a way such that they only affect some sublattices. More specifically, we theoretically and experimentally investigate the 1D and 2D SSH models. The experiments were performed by Walid Cherifi under the supervision of prof. dr. Mohamed Bourennane at the University of Stockholm. We theoretically predicted the precise experimental setup that should be constructed in order to observe the zero-energy monomodes.

4.2 SSH with Loss

We consider a version of the SSH model, in which we introduce a loss of strength 2α on the A sublattice [19, 27, 39, 40], see Fig. 4.1a. The Hamiltonian of this system is given by

$$H = -\sum_{n=1}^{N} \left[\left(t_1 a_n^\dagger b_n + t_2 b_n^\dagger a_{n+1} + H.c. \right) + 2i\alpha a_n^\dagger a_n \right], \tag{4.1}$$

where N is the number of unit cells, and t_1, t_2 denote, respectively, the inter- and the intra-cell hopping parameter. For simplicity, we assume them to be real. The operators a_n ($a_n^\dagger$) annihilate (create) a particle in sublattice A at the site n (similarly for B). The corresponding dispersion relation for PBC is given by

$$\epsilon(k) = -i\alpha \pm \sqrt{-\alpha^2 + t_1^2 + t_2^2 + 2t_1 t_2 \cos(ka)}.$$

We note that the spectrum of the system is similar to the one with OBC. This spectrum is also similar to that of a chain with alternating gain and loss shifted down on the imaginary axis by α. The Hermitian SSH model ($\alpha = 0$) has a topological phase for $t_2 > t_1$. In the case of OBC, this manifests itself in a set of zero-energy edge modes. When α is taken to be finite, one of the zero modes acquires a negative imaginary energy, while the other remains at zero energy. This occurs because we have introduced loss only on one of the two sublattices. Each edge mode has support on one sublattice, thus exhibiting different energies. This behaviour is illustrated in Figs. 4.1b.
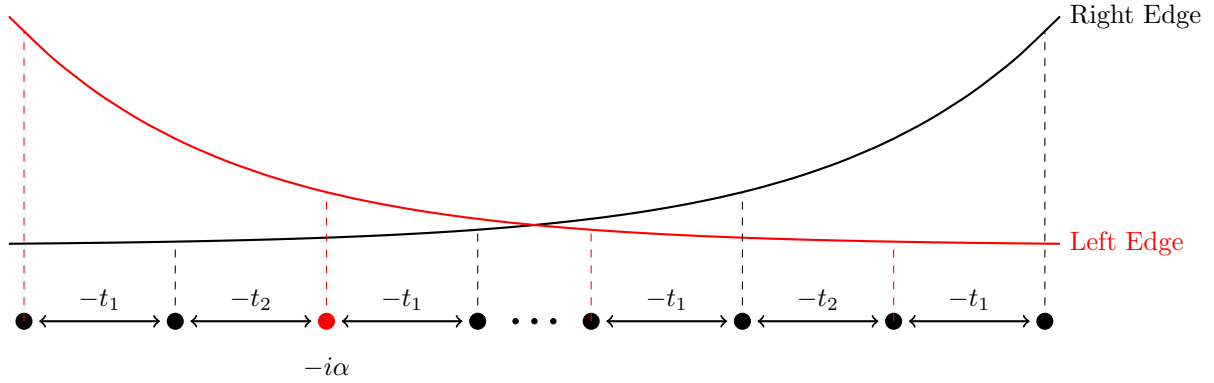
Figure 4.2: One loss site will create a monomode.

The Hamiltonian directly encodes the information about the time-evolution of the eigenstates through

$$|\psi(\mathbf{t})\rangle = \hat{U}|\psi(0)\rangle = \mathrm{e}^{-\frac{i}{\hbar}\hat{H}\mathbf{t}}|\psi(0)\rangle. \tag{4.2}$$

Therefore, the amplitude of states with a negative (positive) imaginary energy will decrease (increase) over time.

Since only one mode of the system has a nonnegative imaginary energy, see Fig. 4.1b, all but one of the states will decay over time. This is illustrated in Fig. 4.1c, where the time-evolution operator is applied to the two edge states of the system. It is clear that only the right edge mode, the one which has support on the sublattice without loss, will endure. Therefore, this system reveals the existence of a topological monomode.

4.3 Only One Loss

The monomode can nevertheless be realised in a more straightforward way. Instead of including losses in every unit cell, it is sufficient to insert only a single loss site into the chain, see Fig. 4.2. The difference is that it takes longer for the bulk modes (and the other edge) to decay. This decay time also becomes size dependent. A second, more practical, constraint is that the loss site should be 'relatively' close to the decaying edge mode for the decay to occur more rapidly. Since the left (right) edge mode has support on the A (B) sublattice, inserting the loss on the B (A) sublattice near the left (right) edge will give the right (left) edge mode a very long lifetime. As a result, it becomes more difficult to experimentally realise such a monomode. For instance, we can put one loss site on sublattice A in the second unit cell

$$H = -\sum_{n=1}^{N} \left[t_1 a_n^\dagger b_n + t_2 b_n^\dagger a_{n+1} + H.c.\right] - i\alpha a_2^\dagger a_2. \tag{4.3}$$

Although the left edge state decays relatively fast in this model, some bulk states take a long time to decay. For a sufficiently long time, the left-edge state and the bulk states belonging to the A sublattice will always decay. In Ref. [1], we show that the SSH model with periodic loss, but also the SSH model with only one loss site, is still topological, by calculating the topological invariant.

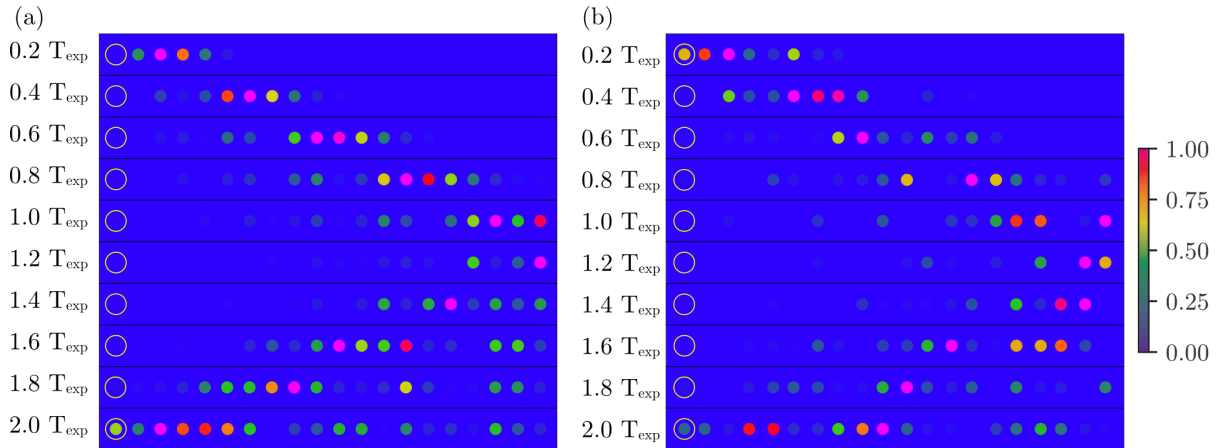To understand the time-evolution of a wavefunction, the Hamiltonians of Eqs. (4.1) and (4.3) were written

Figure 4.3: Numerical predictions of the time propagation of in waveguides. (a) Time propagation of the tight-binding chain. Clearly, a wave is propagating from its incertion point on the left, to the right. At around the time of the experiments, the wave hits the right edge of the chain and reflects back. (b) Time propagation of the trivial SSH chain. We see a similar behaviour as for (a). Figure taken from Ref. [1].

in matrix form,

$$
H = \mathbf{c}^\dagger
\begin{pmatrix}
-2\alpha i & -t_1 & 0 & \cdots & 0 \\
-t_1 & 0 & -t_2 & & \\
0 & -t_2 & -2\alpha i & & \vdots \\
\vdots & & & \ddots & \\
0 & & \cdots & & 0
\end{pmatrix}
\mathbf{c},
$$

for Eq. (4.1) and

$$
H = \mathbf{c}^\dagger
\begin{pmatrix}
0 & -t_1 & 0 & \cdots & 0 \\
-t_1 & 0 & -t_2 & & \\
0 & -t_2 & -\alpha i & & \vdots \\
\vdots & & & \ddots & \\
0 & & \cdots & & 0
\end{pmatrix}
\mathbf{c},
$$

for Eq. (4.3). The pattern along the diagonal is not repeated for the latter Hamiltonian. Here, $\mathbf{c}$ ($\mathbf{c}^\dagger$) are annihilation (creation) operators. The eigenvectors were evolved in time by letting Eq. (4.2) operate on the them. In Fig. 4.3, we show an example of the time-evolution of an excited waveguide, for the simple tight-binding case (Fig. 4.3a) and for the trivial SSH case (Fig. 4.3b). It will be explained in Sec. 4.5 that due to the paraxial equation, we can relate the length of the waveguides to a time quantity. As light moves along the waveguide, time can be promptly determined by the length divided by the speed of light. Therefore, this spatial direction actually corresponds to a time direction. The T_{exp} can be calculated by scaling the length of the waveguide by the hopping parameter t_1, yielding $T_{exp} = Lt_1$, as t_1 takes on the units of inverse length in this setup. This makes it clear that the theoretical predictions for these two models rely heavily on the duration of the experiment (length of the waveguide).

4.4 2D SSH

The SSH model can also be extended into two dimensions. This model displays the same basic behaviour as the 1D SSH model, exhibiting three phases: $\mathcal{PT}$-symmetric phase, $\mathcal{PT}$-broken phase, and a phase with an imaginary line gap. The 2D SSH model is considered a higher order topological (HOT) metal [41–43]. Although the 2D SSH metal presents bulk states at zero energy, they do not hybridise with the
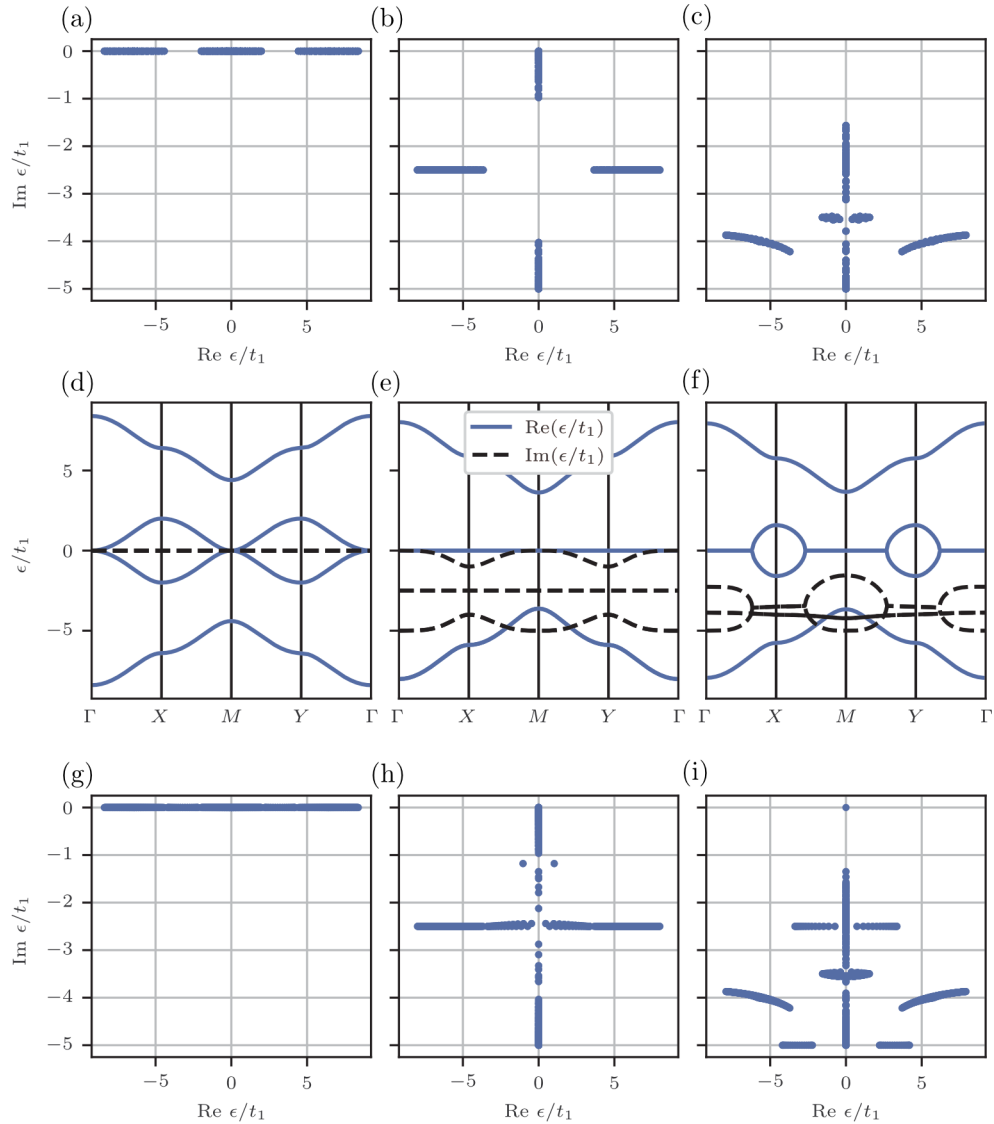
Figure 4.4: Spectrum of the 2D SSH model. (a)-(c) The spectrum in the complex plane for PBC. (d)-(f) Spectrum along the points of high symmetry for PBC. (h)-(i) The spectrum in the complex plane for OBC. (a), (d), and (g) show the spectrum for the lossless 2D SSH model. (b), (e), and (h) show the spectrum for the system with loss along the diagonal of the unit cell, yielding a bimode: only two modes remain at zero energy. (c), (f), and (i) show the spectrum for the model with loss at three sites in the unit cell, yielding a monomode, as there is only one mode remaining at zero energy. Figure taken from Ref. [1].
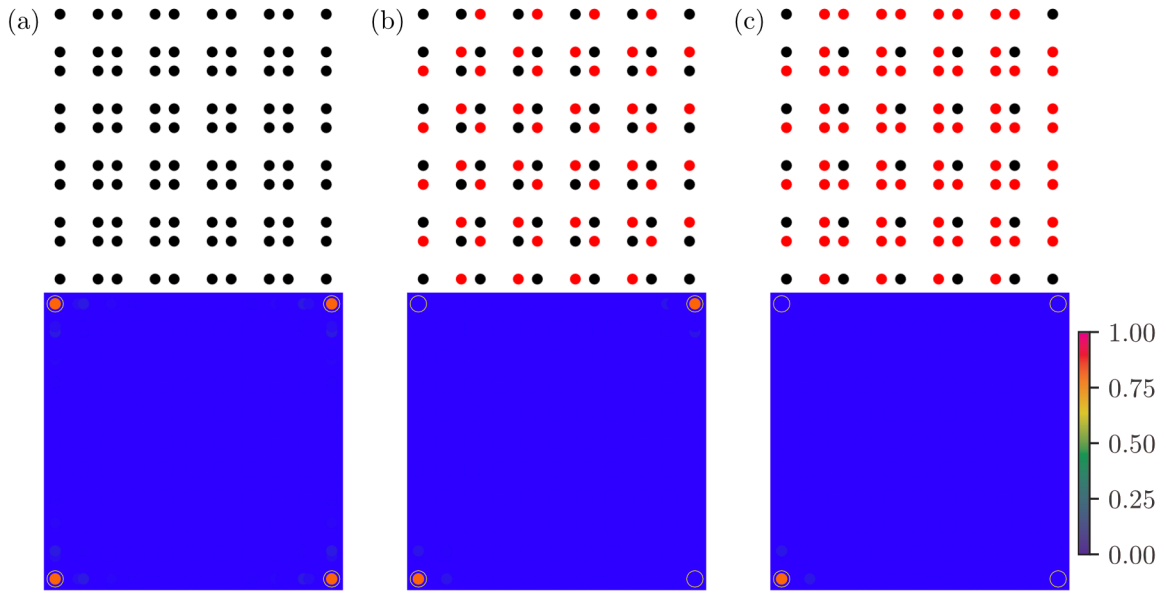
Figure 4.5: Numerical prediction of the bi- and monomodes in the 2D SSH model for 10×10 unit cells with $t_2/t_1 = 3.2$ and $\alpha/t_1 = 5$. Yellow circles signal the point at which light was injected. The top row shows the loss locations in the lattice (red dots) and the bottom row the predictions, for injecting into the four corners. (a) No loss, showing four distinct corner modes. (b) Loss on two sublattices. This breaks the C_{4v} symmetry of the system into C_{2v} and leads to bimodes. (c) By adding loss on three sublattices, the C_{2v} symmetry is broken and the monomode emerges. Figure taken from Ref. [1].

robust symmetry-protected corner modes for large system sizes. The four corner modes are protected by C_{4v} and chiral symmetry, such that we can use again a similar insight to add loss in some of the sublattices and design only two or one corner states, depending on the loss distribution. In Fig. 4.4, we show the spectrum of the 2D SSH model with no loss (Fig. 4.4a,d, and g) and with the loss distribution that produces a bimode (Fig. 4.4b, e, and h) and a monomode (Fig. 4.4c, f, and i). Especially, Fig. 4.4c makes it very clear that all the bulk modes are destroyed in this loss configuration. For OBC, this would leave only one edge state. Fig. 4.5 shows the theoretical results for the 2D SSH model. Here, a larger system size was used than in the experiment. However, the same behaviour can be seen with the realisation of a bimode and a monomode.

4.5 Experimental Observation of our Theoretical Prediction

To experimentally validate the existence of monomodes, a photonic waveguide lattice was built. In this setup, the propagation of the light is determined by the paraxial equation [44]

$$i\frac{\partial}{\partial z}\Psi(x,y,z) = \left(-\frac{1}{2k_0}\left(\frac{\partial^2}{\partial x^2} + \frac{\partial^2}{\partial y^2} \right) - \frac{k_0 \Delta n(x,y)}{n_0} \right) \Psi(x,y,z).$$

Here, Ψ acts as the wavefunction for the electric field, $k_0 = n_0\omega/c$, with ω the light frequency, and n_0 the refractive index, and Δn is the change in refractive index. Although the paraxial equation is classical, it has a structure similar to the Schrödinger equation. This system can be used to model the tight-binding Hamiltonian, where the hopping terms depend on the distance d_i between the waveguides, $t_i \approx e^{-d_i/\xi}$. ξ depends on the parameters of the experiment, such as the wavelength of light. We achieve the desired loss in the system by introducing a certain concentration of microscopic scattering points along the waveguides through the dwelling process. The direct laser-writing technology provided us with the ability to freely tune both the dwelling time and the separation between the individual scattering

(a)

Objective

(b)

Sample

(c)

Objective
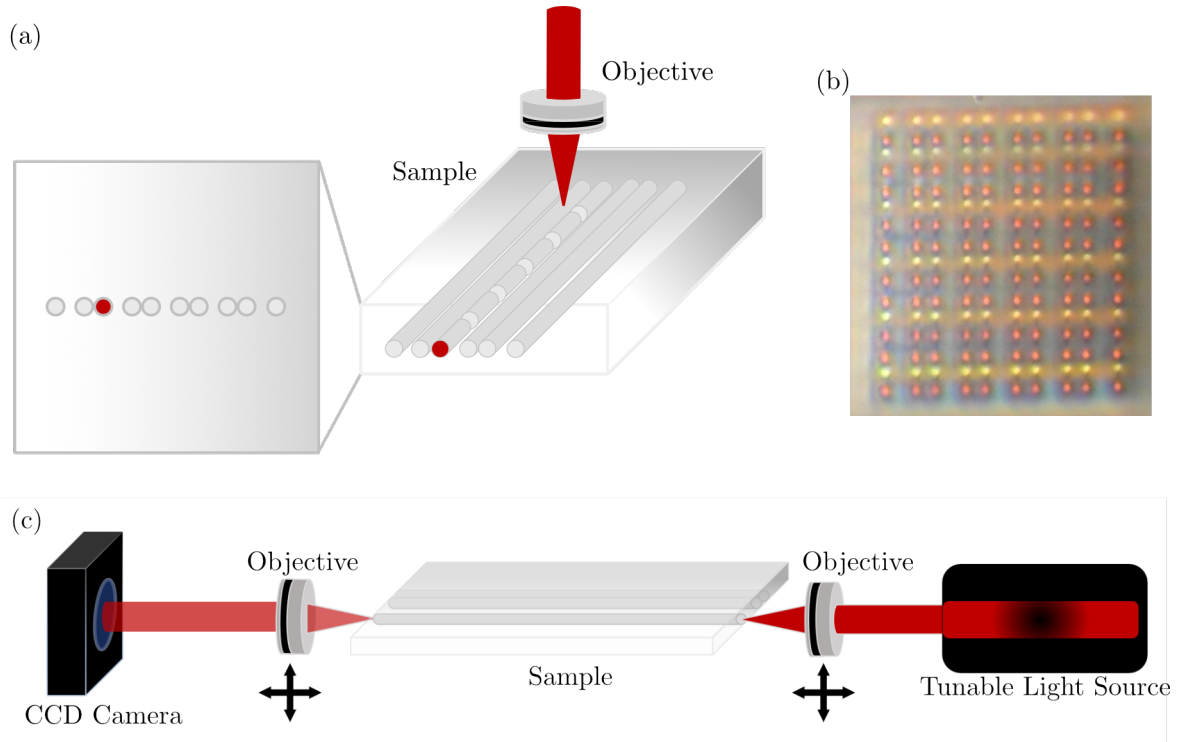
Objective

CCD Camera

Sample

Tunable Light Source

Figure 4.6: Overview of the experimental setup. (a) Schematic overview of the process of creating the waveguides in the sample. Here, the loss is introduced by making cuts in the waveguide. The light is focused using an objective. (b) A microscopic picture of a produced 2D SSH sample. $d_1 = 11 \ \mu m$ and $d_2 = 7 \ \mu m$. (c) Schematic overview of the measurement processed. The light from the tunable light source is focussed using an objective into a specific waveguide of the sample. At the other end, a camera captures the resulting light. Figure taken from Ref. [1].

points, allowing for the implementation of a wide range of artificial losses. Importantly, this process neither compromises the real part of the refractive index nor introduces directionality into the system. The direct laser-writing technique offered us precise control over the amount and distribution of loss in the waveguide lattice, enabling us to design and fabricate the lattice with the desired characteristics.

4.5.1 1D

To illustrate our findings, we now perform a set of eight experiments using waveguides for the 1D model. See Fig. 4.6a for a schematic overview of the waveguide writing process. Fig. 4.6b shows a resulting 2D SSH sample. Finally, Fig 4.6c gives a schematic overview of the measurement setup. One experiment was realized for a simple tight-binding chain without loss, and another for a dimerized chain in the trivial limit. Both show propagation of light in the bulk. Three experiments where performed on the dimerized chain in the topological case, two with loss and one without loss. Finally, three experiments were realised with a topological defect hosting a mode. By moving the location of the loss, this allows for destroying the edge mode, or the defect mode.

The distance between the waveguides was set to $d_1 = 12 \ \mu m$ and $d_2 = 10 \ \mu m$ for the first five experiments. This yields a ratio of $t_2/t_1 \approx 2$ for the topological case. In the topological defect experiments, the distances of $d_1 = 11 \ \mu m$ and $d_2 = 7 \ \mu m$ were used, giving a ratio of $t_2/t_1 \approx 3.2$. The loss for the first five experiments was engineered by making scattering points $0.2 \ mm$ apart in the waveguide, by waiting $0.5 \ s$ with the laser. For the last three (topological defect) experiments, the loss was engineered by adding 50 cuts of $350 \ \mu m$ along the waveguide. To ensure that the edge states did not hybridise before
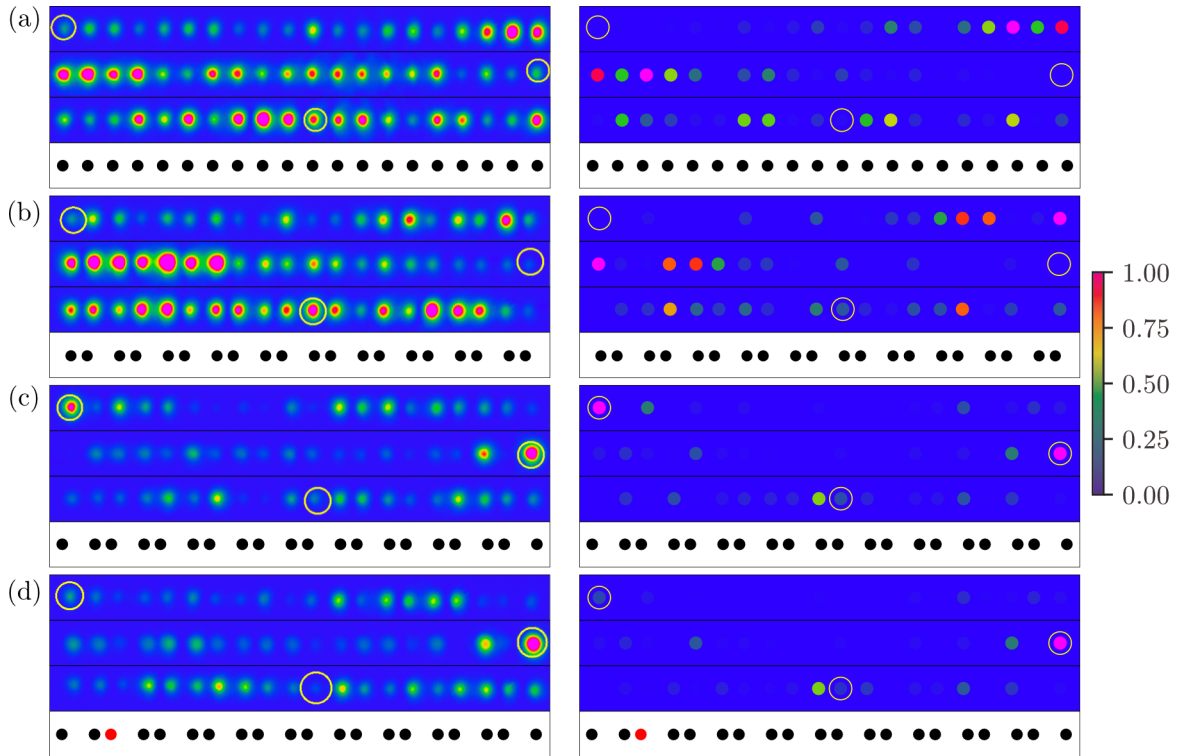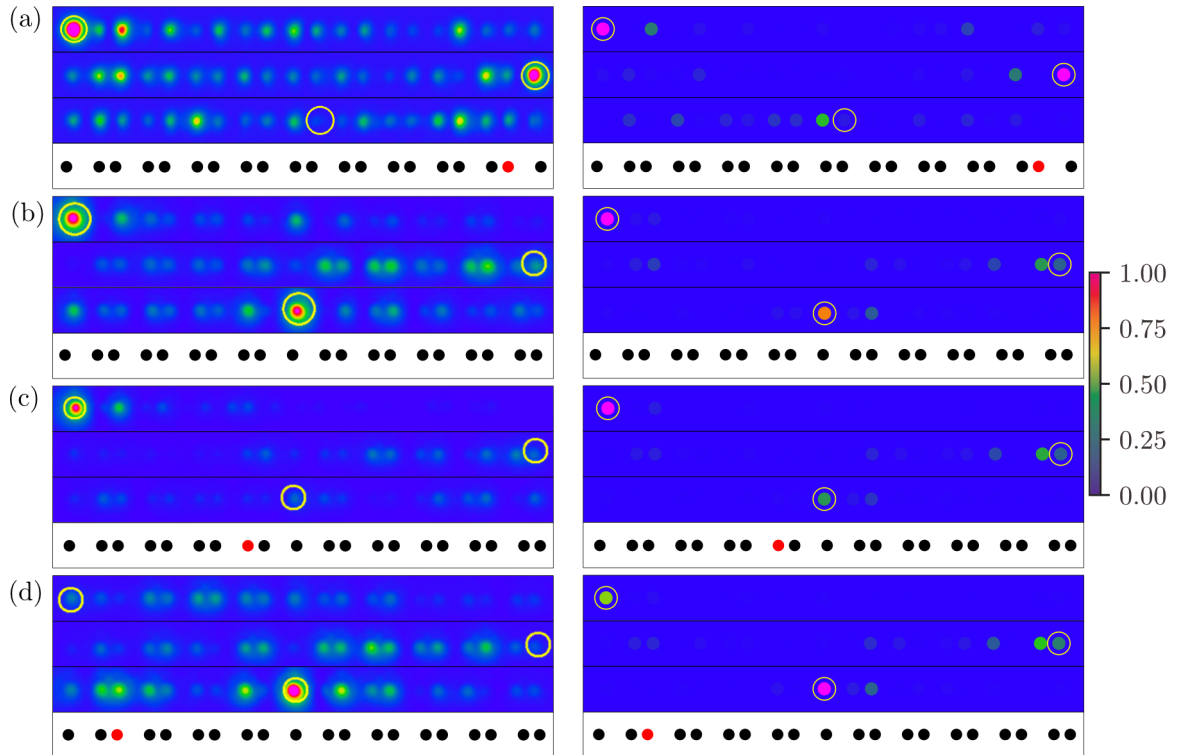
Figure 4.7: Comparison between experimental measurements (left column) and theoretical predictions (right column). Yellow circles signal the point at which light was injected. (a) Tight-binding chain (black dots) with $t_1 = t_2$ dispersing into the bulk. (b) Trivial SSH chain with $t_1/t_2 = 2$ dispersing into the bulk. (c) Topological SSH chain without loss with $t_2/t_1 = 2$. Localised edge modes can be clearly observed. (d) When we add loss ($\alpha/t_1 = 0.5$) at the red-dot site near the left edge, one of the edge modes disappears, revealing the monomode. Figure adapted from Ref. [1].

Figure 4.8: Comparison between experimental measurements (left column) and theoretical predictions (right column). Yellow circles signal the point at which light was injected. (a) The monomode does not appear when the loss site is placed far away from the left edge. In this case, the edge mode does not decay within the experimental time scale. (b) Adding a topological defect to the system ($t_2/t_1 = 3.2$)leads to a left edge mode, as well as a mode pinned on the defect. (c) By placing loss on the red-dot site near the defect this destroys the defect mode, but leaves a monomode at the edge. (d) By placing the loss on the red-dot site near the left edge, the edge mode gets destroyed, but not the defect mode. Figure adapted from Ref. [1].
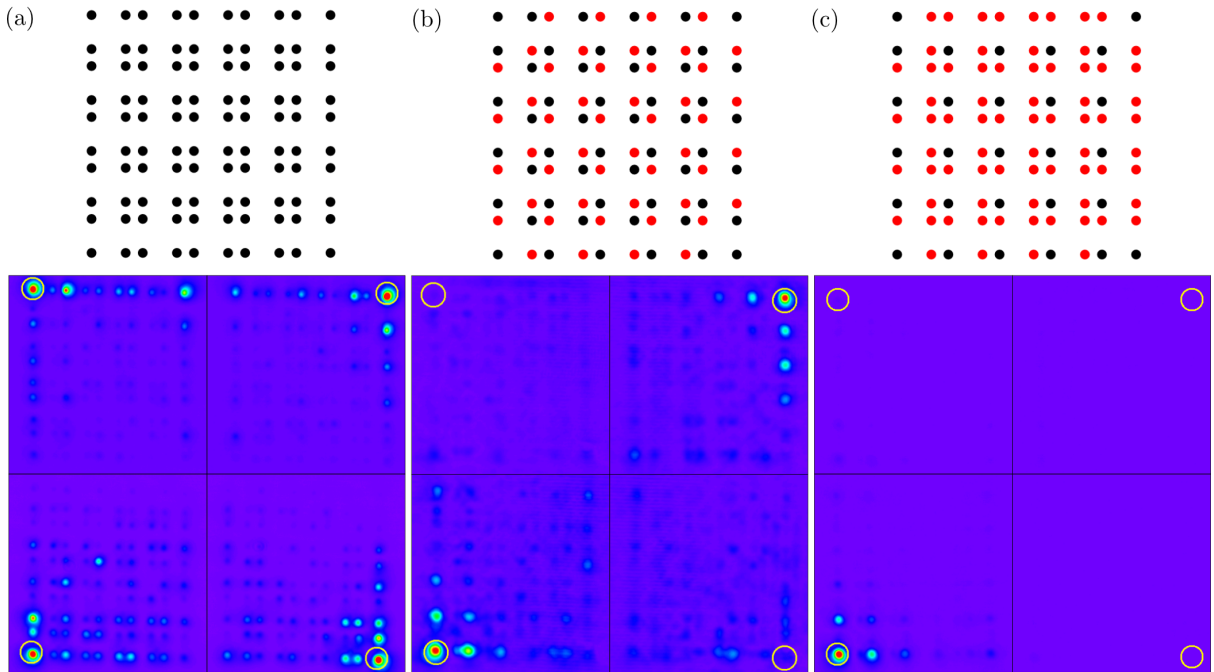
Figure 4.9: Experimental realisation of bi- and monomodes in the 2D SSH model. Yellow circles signal the point at which light was injected. For numerical predictions, see Fig. 4.5. Top row shows the loss locations in the lattice (red dots) and the bottom row the experiments, for injecting into the four corners. (a) No loss, showing four distinct corner modes. (b) Loss on two sublattices. This breaks the C_{4v} symmetry of the system into C_{2v} and leads to bimodes. (c) By adding loss on three sublattices, the C_{2v} symmetry is broken and the monomode emerges. Figure taken from Ref. [1].

the measurement, a system size of 10 unit cells was chosen. Figs. 4.7 and 4.8 show the results of the experiment, together with the theoretical predictions. Yellow circles are included to indicate the point of injection of light. The radius of the circles is proportional to the calculated relative intensity. In the tight-binding model and the SSH model in the trivial phase, we see that light disperses into the bulk (Figs. 4.7a-b). In the topological phase without loss, there are two edge modes (Fig. 4.7c). However, when we add loss on the A sublattice near the left edge (see red dot in Fig. 4.7d), we only observe one edge mode on the right-hand side (B sublattice). When the loss is placed on the A sublattice but far away from the left edge (Fig. 4.8a), the left edge mode does not feel it, and does not decay within the time scale of the experiment. This is in agreement with the theoretical predictions shown in the right column. When the system hosts a topological defect in the centre of the chain, there is an edge mode on the left edge of the chain, as well as a mode pinned on the defect (Fig. 4.8b). When loss is placed on the sublattice B near the defect, the mode pinned on the defect can be destroyed, while the left edge mode is left intact (Fig. 4.8c). Similarly, the loss can be placed on the A sublattice near the left edge. This removes the edge mode, but leaves the mode in the defect (Fig. 4.8d). In appendix A, we present the full experimental data for these experiments.

4.5.2   2D

For the 2D model, three experiments were performed. The first experiment shows the existence of four corner modes. By placing loss on two sublattices, we can reduce the amount of corner modes to two, giving bimodes. When more loss is added, the bimodes can be reduced to a single corner, revealing a monomode.

The distance between the waveguides was set to $d_1 = 11\ \mu m$ and $d_2 = 7\ \mu m$. This yields a ratio of $t_2/t_1 \approx 3.2$. The loss was engineered by adding 100 cuts of 70 μm along the waveguide. A system of 5 by 5 unit cells was used. Fig. 4.9 shows the results of the experiment for the 2D model. Yellow circles are included to indicate the point of injection of light. In the lossless case, the system hosts four corner modes (Fig. 4.9a). By adding loss to two sublattices, two of those corner modes can be destroyed, leaving bimodes (Fig. 4.9b). Adding loss to one more sublattice reveals a monomode in the 2D SSH model (Fig. 4.9c). This is in agreement with the theoretical predictions, presented in Fig. 4.5.

4.6   Conclusion

We have theoretically and experimentally shown the existence of topological monomodes in non-Hermitian systems through the engineering of loss. By introducing losses in a selected sublattice and sufficiently close to the corresponding edge, one of the topological edge modes will decay over time. We have realised these monomodes experimentally in a photonic lattice. Moreover, we confirmed the robustness of the monomodes against perturbations. The implications of our results are multifold. On the one hand, we have identified an extremely simple model capable of revealing monomodes. Since those cannot recombine with their corresponding partner, those monomodes would be ideal candidates for constructing qubits for quantum computers based on topological states. Although they are Abelian, poor-man operations were shown possible with the Hermitian SSH anyons. Here, we have the additional advantage that this mode will not hybridise and hence exhibits further robustness with respect to its Hermitian counterpart. A natural extension of this work is to explore the presence of such states in other $\mathbb{Z}_2$ topological classes and investigate whether engineered loss in other inner degrees of freedom (such as spin or particle / hole) can also be used to generate monomodes.

Chapter 5

Quantum Geometry

A different method to explore the parameter space of a quantum system is through the use of quantum geometry. This method is based on the quantum geometric tensor, which effectively quantifies the distance between states in Hilbert space [45]. At the point of a phase transition, the eigenstates of the system will change rapidly. This can be explored to charter the phase diagram of the system. To demonstrate the power of quantum geometry, we will first show its application to the Hermitian SSH model. After this, we will apply the theory to the non-Hermitian SSH model in 1D and 2D.

5.1 Hermitian Quantum Geometry

We will start with a Hermitian Hamiltonian $H(\lambda)$, which depends on some parameters $\lambda = \{\lambda^\mu\}$. A natural method of measuring the change of the eigenfunctions $|\psi(\lambda)\rangle$ of $H(\lambda)$ under a small perturbation of $d\lambda$, is to calculate [45, 46]

$$ds^2 = 1 - |\langle\psi(\lambda)|\psi(\lambda + d\lambda)\rangle|^2, \tag{5.1}$$

for orthonormal eigenfunctions. When the eigenfunctions overlap, the distance is zero, so $ds = 0$, and when the eigenfunctions are independent, the distance is at a maximum, $ds = 1$. This is closely related to the fidelity, which is the overlap between two states [47],

$$F(\lambda, \lambda + d\lambda) = |\langle\psi(\lambda)|\psi(\lambda + d\lambda)\rangle|.$$

From this fidelity, one can calculate the fidelity susceptibility χ_F. The susceptibility has the advantage over the fidelity itself, in that the fidelity vanishes with system size for many-body systems [48]. However, the susceptibility does not vanish. The fidelity susceptibility is simply the change of the fidelity with respect to the parameter λ, as given by

$$\chi_F = \left.\frac{\partial^2 F}{\partial \lambda^2}\right|_{\lambda=0}.$$

Expanding this equation for small $d\lambda$ yields

$$\chi_F = \frac{\partial x^\mu}{\partial \lambda}\frac{\partial x^\nu}{\partial \lambda}g_{\mu\nu},$$

with the metric tensor

$$g_{\mu\nu} = \frac{1}{2}(\langle\partial_\mu\psi|\partial_\nu\psi\rangle - \langle\partial_\mu\psi|\psi\rangle\langle\psi|\partial_\nu\psi\rangle + \mu \leftrightarrow \nu) \quad \text{with} \quad \partial_\mu = \frac{\partial}{\partial x^\mu}. \tag{5.2}$$

Similarly, one can start from Eq. (5.1), and show that for infinitesimally small $d\lambda$ this yields [46],

$$ds^2 = \chi_{\mu\nu}d\lambda^\mu d\lambda^\nu,$$

where $\chi_{\mu\nu}$ is the geometric tensor,

$$\chi_{\mu\nu} = \langle \partial_\mu \psi | \partial_\nu \psi \rangle - \langle \partial_\mu \psi | \psi \rangle \langle \psi | \partial_\nu \psi \rangle .$$

By inspecting Eq. (5.2), we can observe that the real symmetric part of $\chi_{\mu\nu}$ is the metric tensor

$$g_{\mu\nu} = \mathrm{Re}\ \chi_{\mu\nu} = \frac{1}{2}(\chi_{\mu\nu} + \chi_{\nu\mu}).$$

The imaginary asymmetric part then equals the Berry curvature [46],

$$F_{\mu\nu} = -2\ \mathrm{Im}\ \chi_{\mu\nu} = i(\chi_{\mu\nu} - \chi_{\nu\mu}) = \partial_\mu A_\nu - \partial_\nu A_\mu,$$

where $A_\mu = i \langle \psi | \partial_\mu \psi \rangle$ is the Berry connection [37]. This formalism is quite general, but for the systems discussed in Chapter 3, these parameters λ would correspond to the quantities α/t_1 and t_2/t_1. However, λ is not limited to the parameters of the model, as it can also be the momentum k [49], adding yet another degree of freedom.
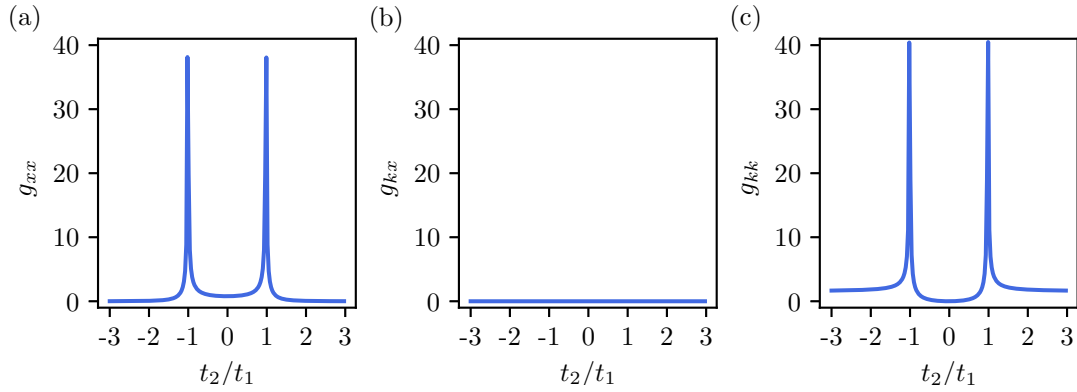
Figure 5.1: The metric tensor for the Hermitian SSH model. 1000 k-points were used for this figure. Here, $x = t_2/t_1$ and k is momentum. (a) The g_{xx} component. There is a clear distinction between the trivial and topological phase $|t_2/t_1| > 1$. (b) The g_{kx} component which seems to vanish. (c) The g_{kk} component again shows the two regimes.

5.1.1 Quantum Geometry of the SSH Model

We will now apply this formalism to a simple model: the SSH model (see Chapter 4). The Hamiltonian of this model is given by

$$H = -\sum_{n=1}^{N} \left(t_1 a_n^\dagger b_n + t_2 b_n^\dagger a_{n+1} + H.c. \right),$$

where N is the number of unit cells, t_1 the inter-cell hopping, and t_2 the intra-cell hopping. The operators a_n ($a_n^\dagger$) annihilate (create) a particle in sublattice A at site n (similarly for B). This system has a trivial phase for $|t_2/t_1| < 1$ and a topological phase for $|t_2/t_1| > 1$, depending on the parameter $t_2/t_1 = x$. Dividing the Hamiltonian by t_1 allows us to write the Hamiltonian as a function of x,

$$H/t_1 = -\sum_{n=1}^{N} \left(a_n^\dagger b_n + x b_n^\dagger a_{n+1} + H.c. \right),$$

with the eigenstates

$$|\psi_\pm\rangle = \begin{pmatrix} \frac{e^{ika}\sqrt{1+x^2+2x\cos(ka)}}{e^{ika}+x} \\ \pm 1 \end{pmatrix}.$$

Calculating Eq. (5.2), summing over momenta, and dividing by the number of k-points yields the results in Fig. 5.1. Here, the three possible metric tensors for the Hermitian SSH model are depicted, namely the g_{xx}, g_{kx} and the g_{kk} component, shown in Figs. 5.1a-c, respectively. Figs. 5.1a and c show a clear distinction between the topological ($|t_2/t_1| > 1$) and trivial ($|t_2/t_1| < 1$) regime of this model. The g_{kx} component vanishes.

5.2   Non-Hermitian Quantum Geometry

The addition of non-Hermiticity to the model slightly changes the relevant equation. This introduces a new degree of freedom: the left and right eigenvectors. Writing the metric tensor in general terms [50],

$$g_{\mu\nu}^{\vartheta\varphi} = \frac{1}{2}\big({}^{\vartheta}\langle\partial_\mu\psi|\partial_\nu\psi\rangle^\varphi - {}^{\vartheta}\langle\partial_\mu\psi|\psi\rangle^\varphi\, {}^{\vartheta}\langle\psi|\partial_\nu\psi\rangle^\varphi + \mu\leftrightarrow\nu\big),$$

where $\{\vartheta,\varphi\} \in \{L,R\}$. The permutation of ϑ and φ is equal to a complex conjugation [50]. However, because only $\vartheta \neq \varphi$ will yield an orthonormal basis, $\vartheta = \varphi$ will not truly be metric tensors. Nonetheless, we will still calculate them for the non-Hermitian SSH model, with alternating gain and loss as studied in Chapter 3, given by

$$H = -\sum_{n=1}^{N}\Big[\big(t_1 a_n^\dagger b_n + t_2 b_n^\dagger a_{n+1} + H.c.\big) + 2i\alpha a_n^\dagger a_n\Big],$$

where α is the loss strength. Dividing by t_1 yields

$$H/t_1 = -\sum_{n=1}^{N}\Big[\big(a_n^\dagger b_n + x b_n^\dagger a_{n+1} + H.c.\big) + 2iy a_n^\dagger a_n\Big].$$

Because the model has two independent parameters, namely $\alpha/t_1\ (= y)$ and $t_2/t_1\ (= x)$, we can calculate six metric tensors for every basis (the combinations being xx, yy, xy, kk, kx, ky). There are three possible bases, which results in a total of 18 metric tensors. The real part of the metric tensor for the first three of the sixth parameter combinations are shown in Fig. 5.2. Figs. 5.2a-c show the metric tensors for the biorthogonal LR basis, Figs. 5.2d-f for the LL basis, and Figs. 5.2g-i for the RR basis. One can see the transition between the trivial and the topological regime along the vertical axis. This is most clear in Fig. 5.2a, where there are two horizontal lines at $t_2/t_1 = \pm 1$. To explain the cross structure along the diagonals, we return to Table 3.1 on page 20, where we discuss the possible regimes for this model. Depending on the strength of the loss and the dimerisation, this system can have a phase where the spectrum is entirely real, the $\mathcal{PT}$-symmetric phase. It can also have a phase where the $\mathcal{PT}$-symmetry is spontaneously broken without a gap. Finally, it can have a spontaneously broken $\mathcal{PT}$-symmetry phase with an imaginary line gap. These three phases can exist in both the trivial and topological regimes. This gives a total of six different phases, illustrated in the phase diagram of Fig. 5.3. However, the metric tensors of Fig. 5.2 shows more structure than is depicted in this phase diagram, as the metric tensors also show sign differences for identical phases in the phase diagram. The model from Chapter 3 with only loss would give identical results to the model with gain and loss. However, instead of breaking the true $\mathcal{PT}$-symmetry, passive $\mathcal{PT}$-symmetry would be broken because this model is shifted down along the imaginary energy axis and therefore has no true $\mathcal{PT}$-symmetry. Notably, this phase diagram is very similar to the phase diagram of the non-Hermitian SSH model with non-reciprocal hopping for periodic boundary conditions, discussed in Ref. [51]. This non-reciprocal model has no horizontal lines, but the cross structure is identical. The only difference is that the parameter on the horizontal axis of this model is the non-reciprocity instead of the loss. It is also interesting to look at the imaginary part of the metric tensors. In the Hermitian case, the symmetric part of the quantum geometric tensor is real. This is no longer true for a non-Hermitian system. Fig. 5.4 shows the imaginary part of the LR metric tensors. Interestingly, the topological transition lines do not show up in these figures. Still, the non-Hermitian phase transitions are depicted more clearly, and with less noise than in the real part.
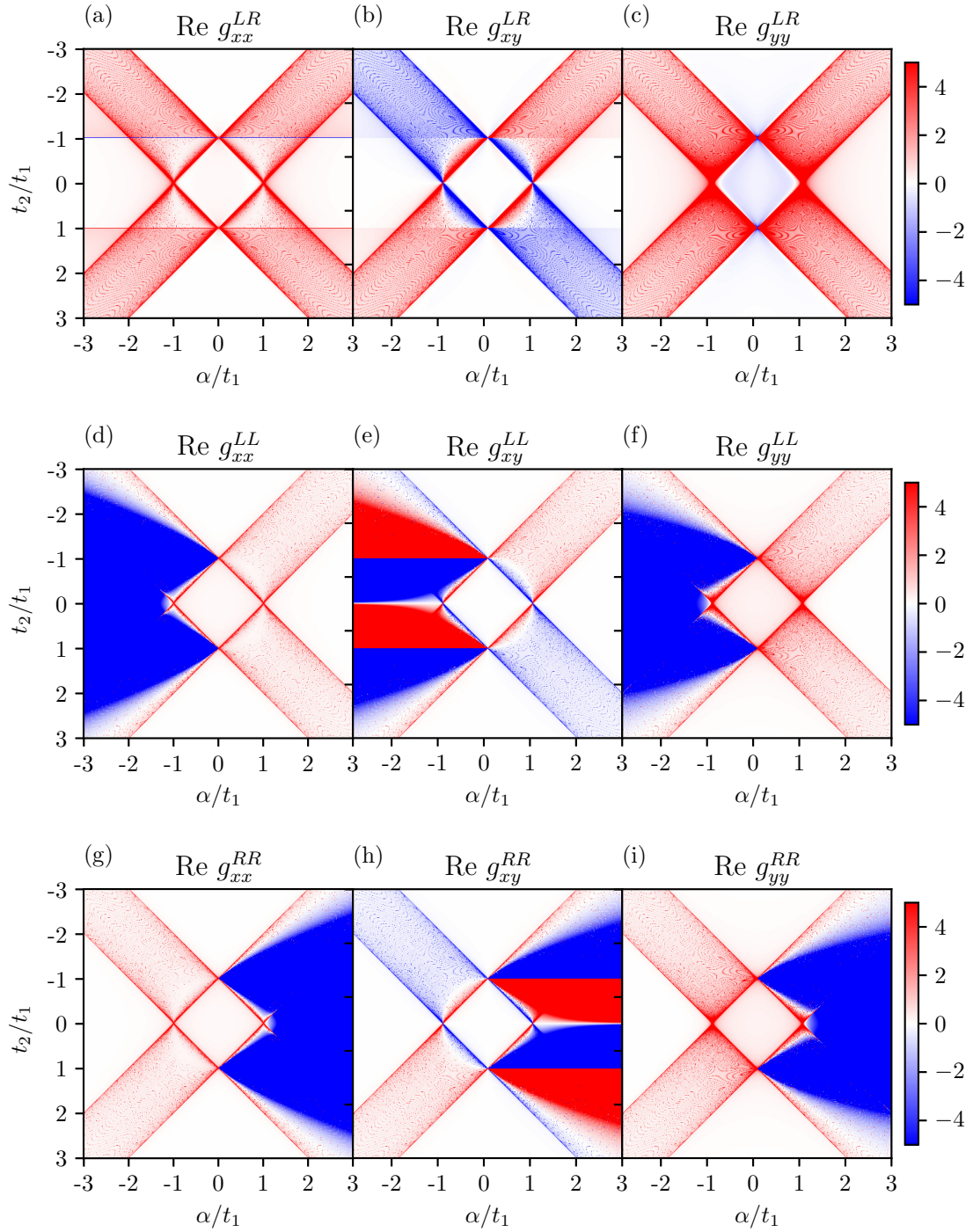
Figure 5.2: Real part of the metric tensor for the x and y components, for 1000 k-points, for the alternating gain and loss SSH model. (a)-(c) The LR part of the metric tensor shows the system's six different phases. (d)-(f) The LL part of the metric tensor. (g)-(i) The RR part of the metric tensor. Both, the LL and RR parts of the metric tensor are not able to capture the complete phase diagram.
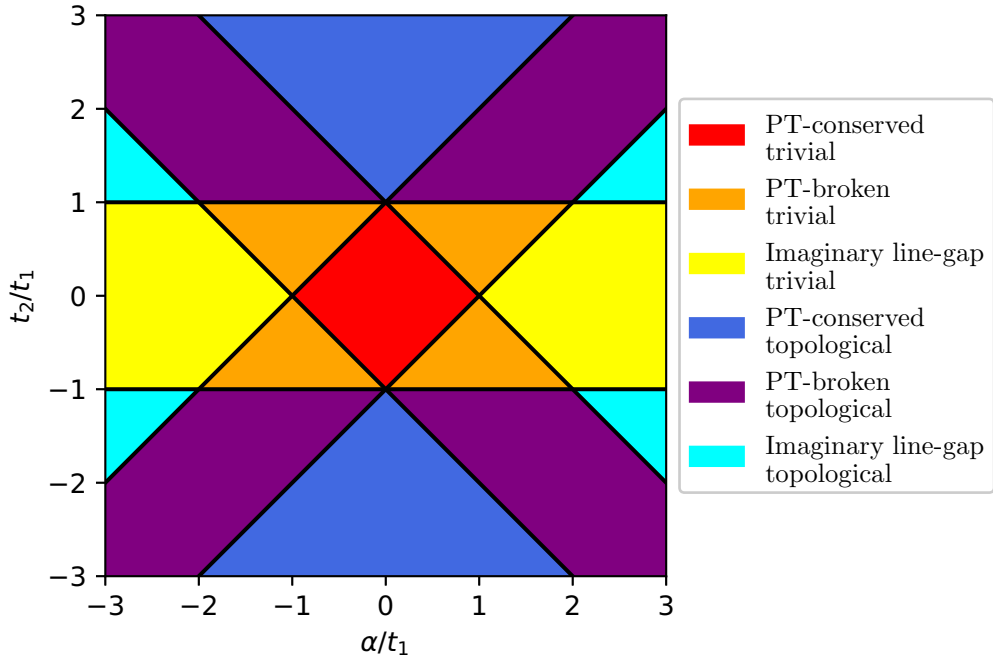
Figure 5.3: Phase diagram for the SSH model with alternating loss (and gain). The trivial and topological regimes have three subphases related to the non-Hermiticity. Those being a $\mathcal{PT}$-conserved, broken and a broken phase with an imaginary line gap. This phase diagram was calculated based on the band structures from Chapter 3.
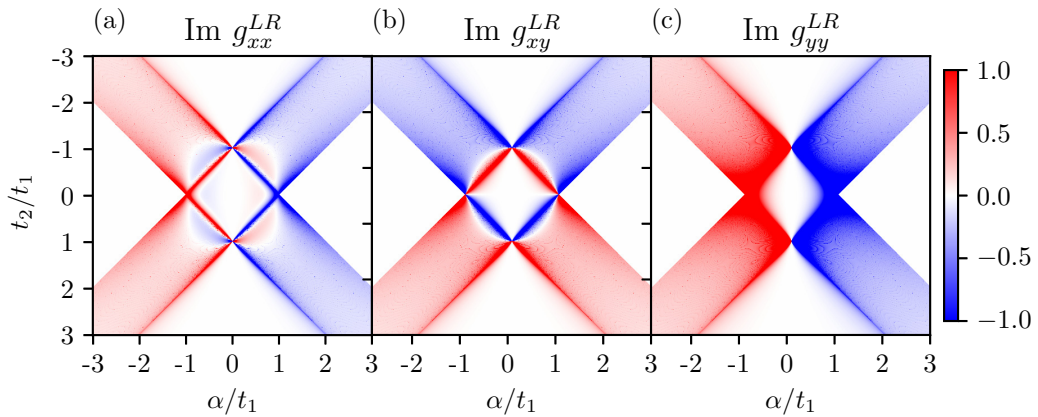
Figure 5.4: The imaginary part of the LR metric tensors of Fig. 5.2 for 1000 k-points. (a) The g_{xx}^{LR} metric tensor. (b) The g_{xy}^{LR} metric tensor. (c) The g_{yy}^{LR} metric tensor.
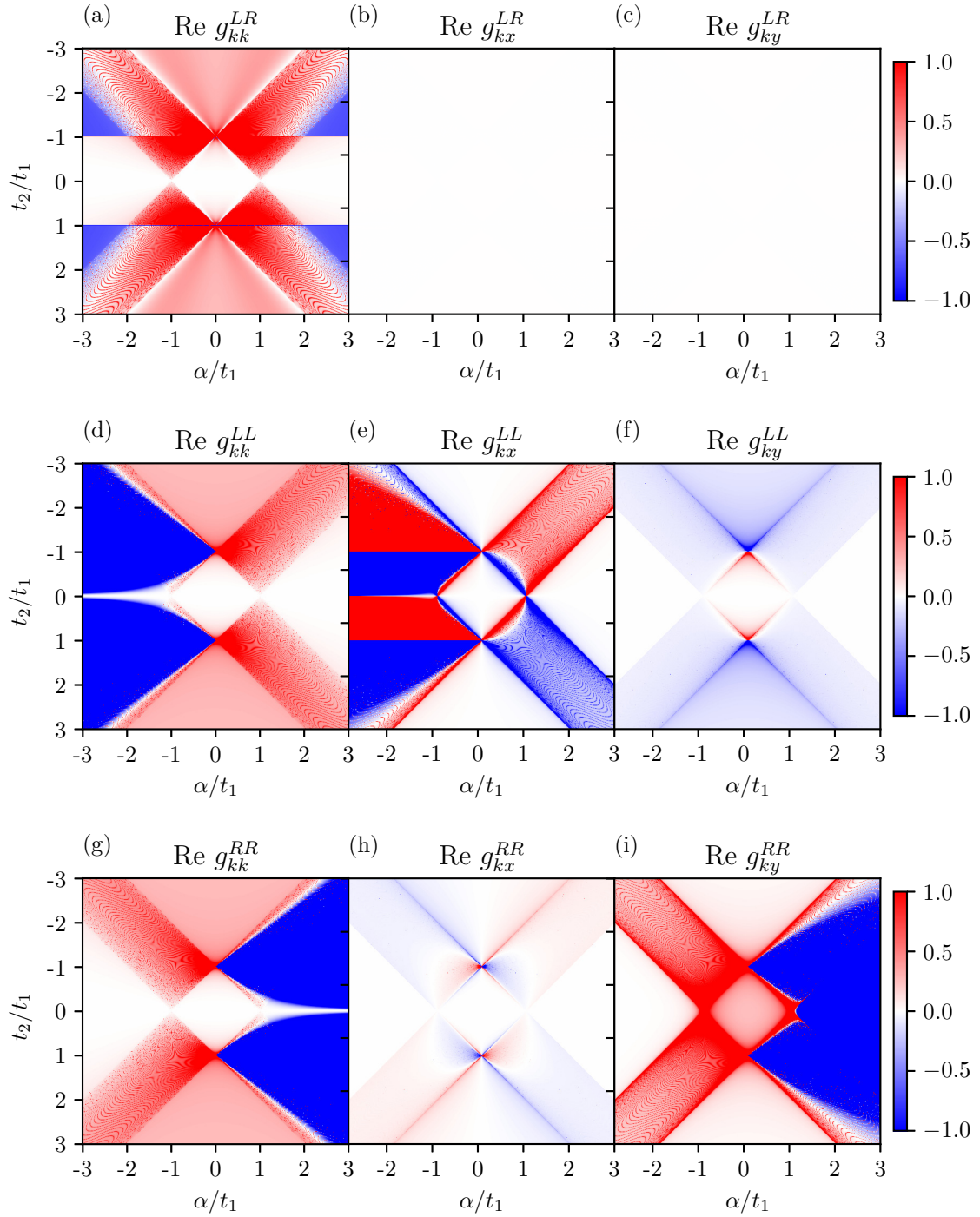
Figure 5.5: Real part of the metric tensor for the k and x/y components, for 1000 k-points, for the alternating gain and loss SSH model. (a)-(c) The LR part of the metric tensor shows the system's six different phases. (d)-(f) The LL part of the metric tensor. (g)-(i) The RR part of the metric tensor.

Finally, we discuss the metric tensors with a momentum component. These can be seen in Fig. 5.5. Figs. 5.5a-c show the metric tensors for the biorthogonal LR basis, Figs. 5.5d-f for the LL basis, and

Figs. 5.5g-i for the RR basis. The same structure appearing in Fig. 5.2 is visible. In particular, the g_{kx}^{LR} and g_{ky}^{LR} components seem to vanish, just as the g_{kx} component vanished for the Hermitian SSH model.
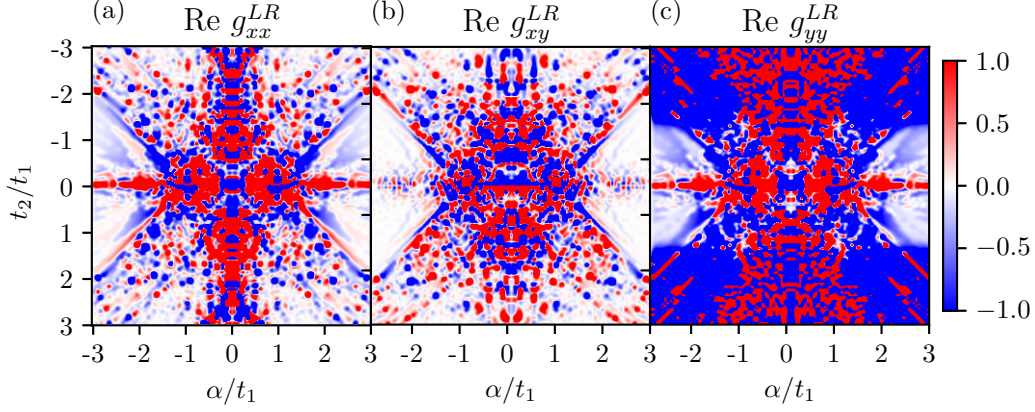
Figure 5.6: *Real part of the metric tensor for the gain and loss SSH model with OBC. The system size was 10 unit cells. All three components show the same structure as for PBC. (a) The g_{xx}^{LR} component. (b) The g_{xy}^{LR} component. (c) The g_{yy}^{LR} component. The transition between the topological and trivial regime appears to occur for higher values of $|t_2/t_1|$ than 1 due to the finite size effect.*
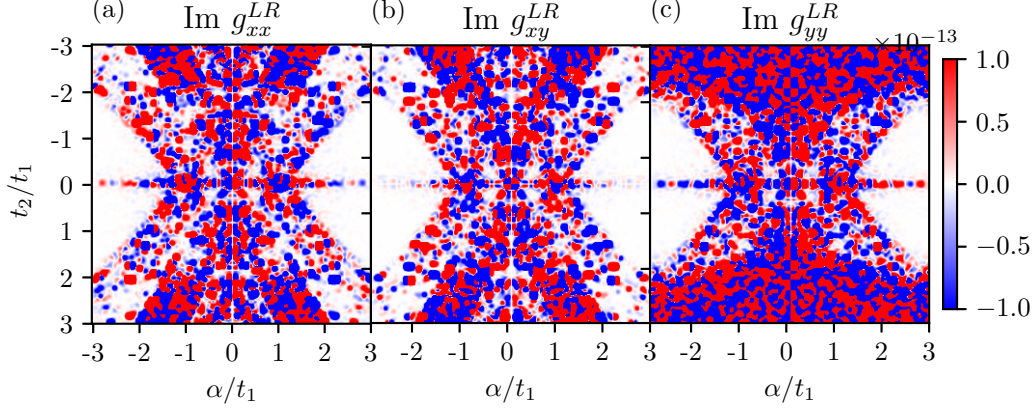
Figure 5.7: *Imaginary part of the metric tensor for the gain and loss SSH model with OBC. The system size was 10 unit cells. All three components show the same structure as for the PBC. (a) The g_{xx}^{LR} component. (b) The g_{xy}^{LR} component. (c) The g_{yy}^{LR} component.*

The same method can be applied to a system with OBC. However, special care is required to deal with the derivatives of the wave functions. Given a Hermitian matrix H, with eigenvectors v_i and eigenvalues λ_i, the derivative of this eigenvectors with respect to a variable of the matrix, $\dot{v}_i$, is given by [37],

$$\dot{v}_i = \sum_j \frac{v_j^\dagger \dot{H} v_i}{\lambda_i - \lambda_j} v_j.$$

Based on the fact that our system is pseudo-Hermitian and therefore $\left|\psi^R(x,y)\right\rangle = \left|\psi^L(x,-y)\right\rangle$, we will apply this method to the case of the non-Hermitian SSH model. However, summing over exceptional

points has to be avoided as the denominator will be zero, since the eigenvalues in exceptional points are the same. Results for a system of 10 unit cells can be seen in Figs. 5.6 and 5.7. The first shows the real part of the metric tensors g_{xx}^{LR}, g_{xy}^{LR}, and g_{yy}^{LR}, while the latter shows the imaginary part. The same general structure as for the PBC system can be seen in both figures. This is not unexpected, since the PBC and OBC systems do not behave differently, as they have the same spectrum, only with a different (pseudo)momentum distribution. Due to the finite size of the system, some transitions occur at values different from those for the periodic model. This is especially visible for the topological/trivial phase transition, which occurs closer to $t_2/t_1 \approx 1.5$, in Fig. 5.6c.

5.3   Non-Hermitian 2D SSH

The theory of quantum geometry is not limited to 1D systems. It can also be applied to 2D models. However, due to the extra dimension, the computational requirement increases dramatically. We will use the information we learnt for the 1D case to limit the number of metric tensors to calculate for the 2D model. Therefore, we will only show results for the g_{xx}^{LR} and g_{xy}^{LR} metric tensors, as they clearly shows the distinct phases in the 1D model. The metric tensors for the 2D SSH model with loss and gain along the diagonal of the unit cell (for which the unit cell is depicted in Fig. 5.8) for periodic boundary conditions can be seen in Fig. 5.9. There is a lot of noise due to the numerical integration. However, the same phase diagram as the non-Hermitian 1D model is visible.
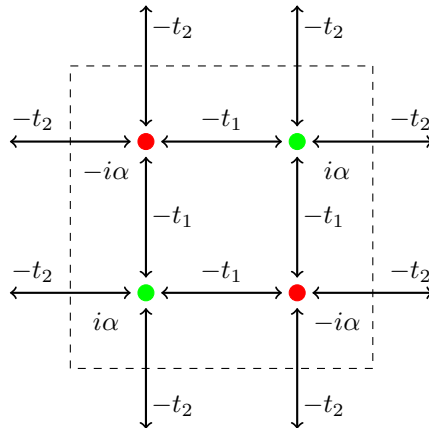
Figure 5.8: The unit cell for the 2D SSH model with loss.
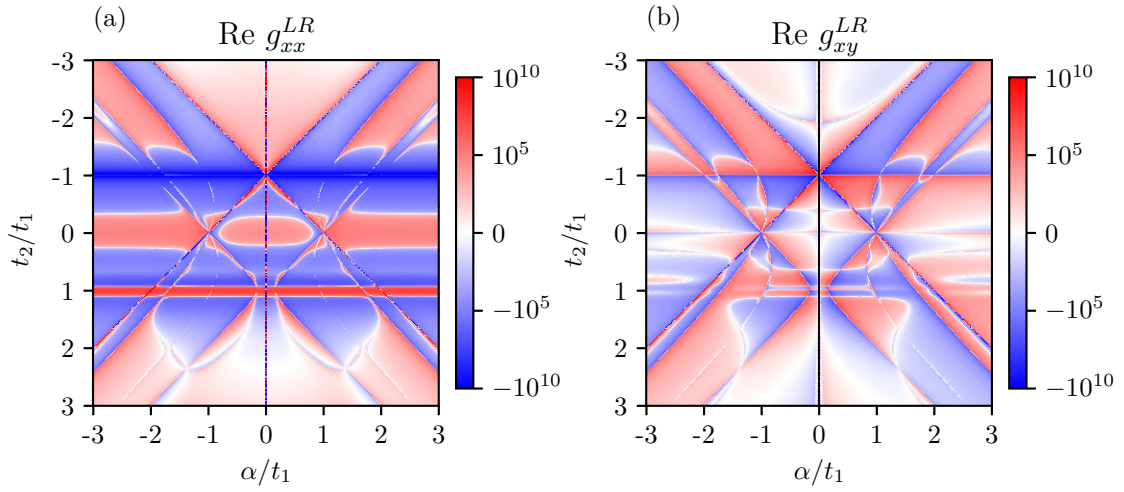
Figure 5.9: (a) The g_{xx}^{LR} component of the metric tensor for the 2D SSH model with loss and gain for periodic boundary conditions. A new region has appeared in the range $1/2 < |t_2/t_1|$, which requires further study. (b) The g_{xy}^{LR} component of the metric tensor for the 2D SSH model with loss and gain for periodic boundary conditions.

Part II

Time Crystals

Chapter 6

Imaginary Time Crystals

In 2012, Shapere and Wilczek proposed the idea of time crystals [11], which are systems that break time-translation symmetry. Whereas regular crystals have a periodic nature in space, time crystals would have persistent oscillations. In a companion paper, Wilczek also proposed the idea of a time crystal for quantum systems [10]. Although the original proposal was later proven to be impossible [52–55], it generated a profuse area of research with many theoretical and experimental realizations [54–56]. In the same paper, he also speculated on the existence of imaginary time crystals (iTC). Instead of being periodic in regular time, these systems would be periodic in imaginary time τ, or, in inverse temperature, since imaginary time is periodic in $\beta = 1/(k_B T)$. The first theoretical investigation of imaginary time crystals was done by *Cai et Al.* [13], where, the authors show that an open system can display macroscopic properties that oscillate as a function of temperature. Next, *Arouca et Al.* [14] showed that non-Hermitian quantum gases can also display this phase due to the presence of resonances in the Matsubara Green's function. They considered the Hatano-Nelson for example, showing in which parameter range there is oscillation in imaginary time. During this thesis, we also briefly investigated a different method of obtaining a phase similar to the iTC phase. The results of this are given in appendix B. Here, it was tried to obtain a similar phase to the iTC phase, using the Floquet [57] formalism. To show the existence of imaginary time crystals, we start with the partition function of a general quantum gas [12]

$$\mathcal{Z} = \int D\Psi^\dagger D\Psi e^{-S[\Psi^\dagger, \Psi]},$$

where the action is given by

$$S\left[\Psi^\dagger, \Psi\right] = \int_0^{\hbar\beta} d\tau \left[\Psi^\dagger(\tau)(\hbar\partial_\tau - \mu + H)\Psi(\tau)\right].$$

Here, Ψ are the fields that parametrise the coherent states of the system, μ is the chemical potential and H is the Hamiltonian governing the system. Here, imaginary time τ is obtained by performing an analytical continuation from real time to imaginary time by substituting $\mathfrak{t} = -i\tau$. This can be a tight-binding Hamiltonian, for instance. For non-interacting quantum gases, the action is quadratic. Therefore, this integral can be performed exactly. This leads to [12]

$$\mathcal{Z}_{B/F} = \det\left(\hbar\partial_\tau - \mu + H\right)^{\mp 1} = \det(G)^{\pm 1}.$$

Here, G is the Green's function of the system. It describes all thermodynamic properties of the system due to Wick's theorem [12]. This states that all correlation functions of non-interacting systems are proportional to products of the two-point function, which is given by the Green's function. Taking the Fourier transform of this Green's function in imaginary time yields

$$\widetilde{G}_n = \frac{1}{-i\hbar\omega_n - \mu + H}, \tag{6.1}$$

where ω_n are the so-called *Matsubara frequencies* [12]. These are discrete frequencies that arise because
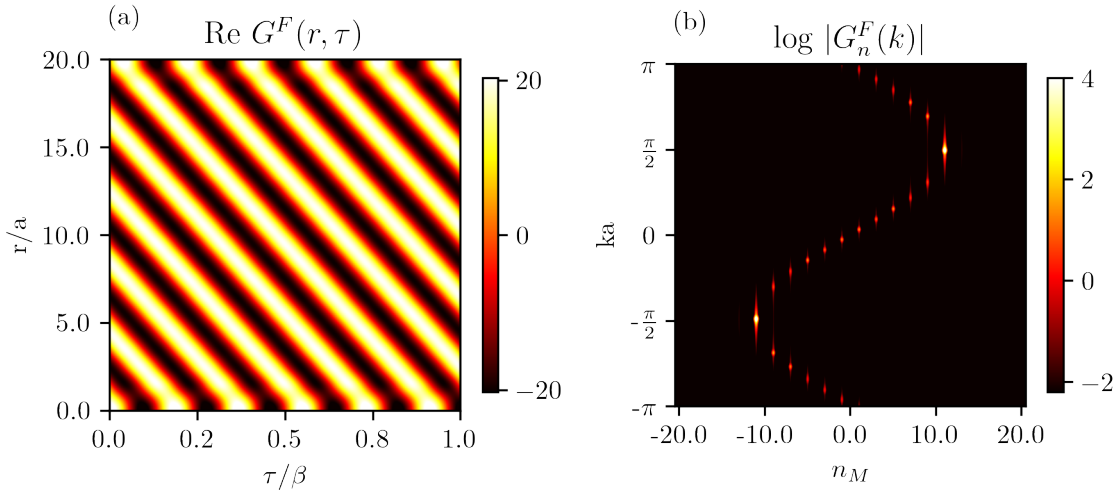

Figure 6.1: Green's function for the Hatano-Nelson model with periodic boundary conditions. The model parameters are $\beta = 1$, $t = 0.1$, $\mu = -10^{-3}$, and $\Gamma = 11\pi/2$. Therefore, the resonance is at $n_M = \pm 11$. 100 k-points were used. (a) The Green's function as a function of imaginary time and space. Here, the imaginary time crystal properties can be seen. (b) The pole structure of the Green's function as a function of the Matsubara modes and the momentum. The poles are clearly visible at $ka = \pm\pi/2$. There are also smaller poles visible in this plot, where the positive part of the energy is not 0. Figure reproduced from Ref. [14].

the imaginary time is periodic in β. They are given by

$$\hbar\omega_n = \frac{\pi}{\beta} n_M = \frac{\pi}{\beta} \begin{cases} 2n & \text{bosons,} \\ (2n+1) & \text{fermions,} \end{cases} \tag{6.2}$$

where n is an integer value. Therefore, the Matsubara modes n_M are even for bosons and odd for fermions. The number of photons is not a conserved quantity, and thus the chemical potential is zero. Since we are mostly concerned with photons (bosonic particles) in this thesis, we set $\mu = 0$ until further notice. Applying the (non-Hermitian) resolution of identity to Eq. (6.1) yields

$$\widetilde{G}_n = \sum_m \phi_m^R \phi_m^{L\dagger} \frac{1}{-i\hbar\omega_n + \epsilon_m}. \tag{6.3}$$

This equation already allows for an interesting observation for non-Hermitian systems [14]. In Chapter 2, we discussed the fact that non-Hermitian systems can have complex eigenvalues and that $\mathcal{PT}$-symmetric systems can have eigenvalues that are either fully real or fully imaginary. In Eq. (6.3), we observe that the Green's function has poles when $i\hbar\omega_n = \epsilon_m$. $\hbar$ and ω_n are fully real quantities. Thus, this equality only holds when $\text{Re}(\epsilon_m) = 0$ and

$$\text{Im}(\epsilon_m) = \hbar\omega_n. \tag{6.4}$$

The Green's function only has poles, when the energy is fully imaginary. Eq. (6.4) also puts a constraint on the temperature of the system. Recalling from Eq. (6.2) the definition of Matsubara modes, we get $\text{Im}(\epsilon_m) = n_M \pi k_B T$. This equality has no non-trivial solutions for the high-temperature regime, as can be seen by inspecting Eqs. (6.2) and (6.4). In the high temperature regime, a very large imaginary
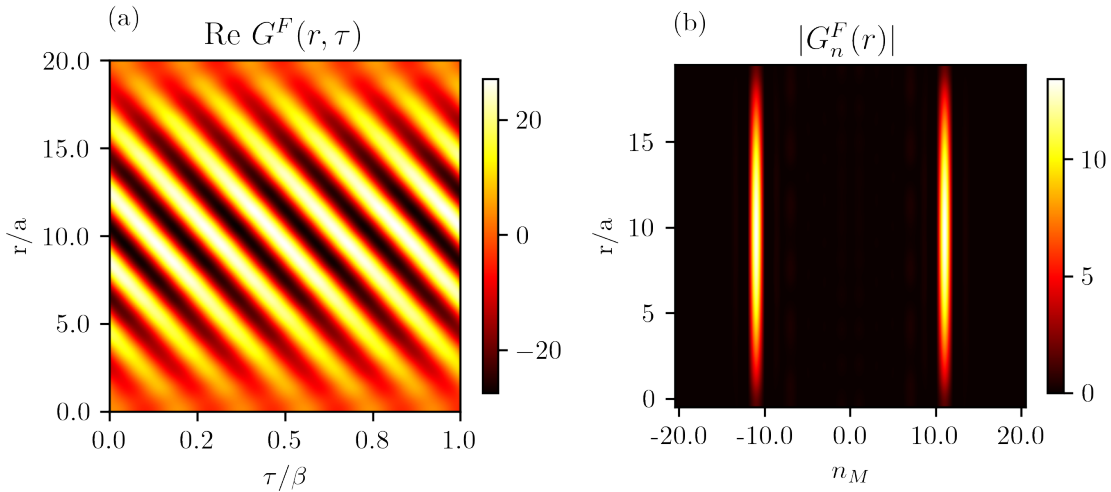
Figure 6.2: Green's function for the Hatano-Nelson model with open boundary conditions. The model parameters are $\beta = 1$, $t = 0.1$, $\mu = -10^{-3}$, and $\sqrt{\Gamma^2 - t^2} \approx 11\pi/2$. Therefore, the resonance is at $n_M = \pm 11$. The parameters are slightly different than those of the periodic case due to the finite size. The system consisted of 10 unit cells. (a) The Green's function as a function of imaginary time and space. Here, the imaginary time crystal properties can be seen. The 'haze' near the edges of the chain are due to the OBC and the finite size of the chain. (b) The pole structure of the Green's function as a function of Matsubara modes and space. The poles are clearly visible at $n_M = \pm 11$. Figure reproduced from Ref. [14].

energy is required to obtain the iTC phase. Near the resonance frequencies, the Green's function can be approximated as a function of imaginary time [14],

$$G(\tau) \approx \beta \sum_m \phi_M^R \phi_m^{L\dagger} \frac{1}{\mathrm{Re}(\epsilon_m)} e^{-i\omega_n \tau}. \tag{6.5}$$

Here, we are probing the function near a pole, and not at a pole, to avoid divergences. This function clearly oscillates as a function of imaginary time. This makes it clear that non-Hermitian systems can be imaginary time crystals.

6.1   Hatano-Nelson Model

In a paper by *Arouca et al.* [14], the authors show that the Hatano-Nelson model exhibits an imaginary time crystal phase. In this section, we will try to reproduce these results. The Hatano-Nelson model is a tight-binding model with non-reciprocal hopping. The Hamiltonian is given by

$$\hat{H} = - \sum_{j=0}^{N-1} \left[(t - \Gamma)\hat{c}_j^\dagger \hat{c}_{j+1} + (t + \Gamma)\hat{c}_{j+1}^\dagger \hat{c}_j \right],$$

where t is the hopping amplitude and Γ the non-reciprocity. It is useful to consider the resonance conditions. Since the system is fermionic, the resonance condition is equal to

$$i\hbar\omega_n = \epsilon_m - \mu.$$

The dispersion relation for the Hatano-Nelson model with periodic boundary conditions (PBC) is given by

$$\epsilon(k) = 2t\cos(ka) - 2\Gamma i \sin(ka),$$

which is only fully imaginary if $ka = \pm\pi/2$. This results in

$$n_M = \pm\frac{2\beta\Gamma}{\pi},$$

and $\mu = 0$. In practice, μ will not be zero, to avoid divergences at the resonance momentum. Instead, it
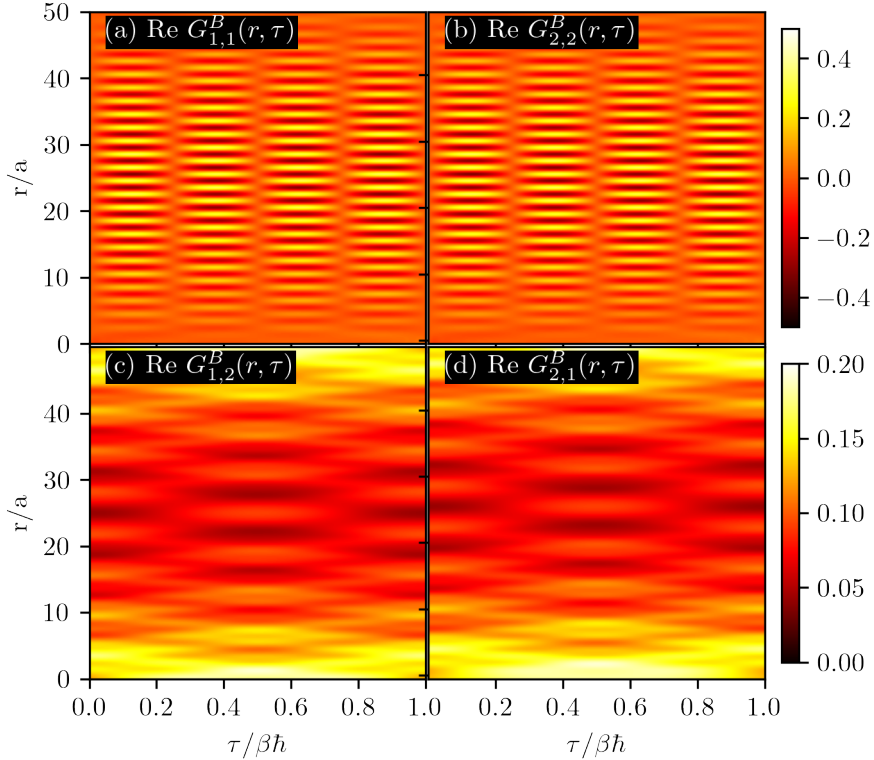

Figure 6.3: Green's function in imaginary time and real space, where the imaginary time component is calculated by a Fourier transform of Eq. (6.1) from Matsubara modes to imaginary time. Results are for PBC, bosonic case, $\beta = 2\pi$, $\mu = 0$, $\alpha/t = 2.001$ and for 50 unit cells (and thus also 50 k-points). Here $G(r,\tau)$ is shown as a function of unit cells. The top colorbar is for (a) and (b) and the bottom bar is for (c) and (d). Notice how the amplitude in (a) and (b) is two times higher than in (c) and (d). Furthermore, the top and bottom rows also show different periodicity. The top row shows two full oscillations, while the bottom row only has one.

will have a small value. In Fig. 6.1, the Green's function is plotted for the Hatano-Nelson model for PBC. This figure makes it clear that the system is indeed an imaginary time crystal, because there are clear oscillations in imaginary time. The same can be seen in Fig. 6.2 for OBC. There are small differences between the two figures. For instance, the poles cannot be plotted for momenta due to the OBC, so the figure is given for real space. Overall, it describes the same behaviour as in the PBC case. For OBC, we can calculate a so-called surrogate Hamiltonian, which is a PBC Hamiltonian, with an extra term due to an analytical continuation of momentum to imaginary momentum, to simulate exponential decay at

the edge. For more details about this procedure, see Ref. [14]. The resulting spectrum is given by [14]

$$\epsilon_{\text{surr}}(k) = \begin{cases} 2i\,\text{sgn}(\Gamma)\sqrt{|\Gamma^2 - t^2|}\sin(ka), & |\Gamma/t| > 1 \\ -2\,\text{sgn}(t)\sqrt{|\Gamma^2 - t^2|}\cos(ka), & |\Gamma/t| < 1 \end{cases}.$$

This results in a new resonance condition,

$$n_M = \pm\frac{2\beta\sqrt{\Gamma^2 - t^2}}{\pi}.$$

6.2 Gain and Loss

We will now focus our attention on the Green's function of the optical systems discussed in Chapter 3. We will start by considering the periodic systems. We will not treat the OBC variant of these because, as we already concluded in Chapter 3, the behaviour of the spectrum does not depend on the boundary conditions. An exception is the SSH model in the topological phase. After discussing these systems, we will investigate the Green's function of the OBC systems with aperiodic loss distributions. The results in this and the following sections are original.
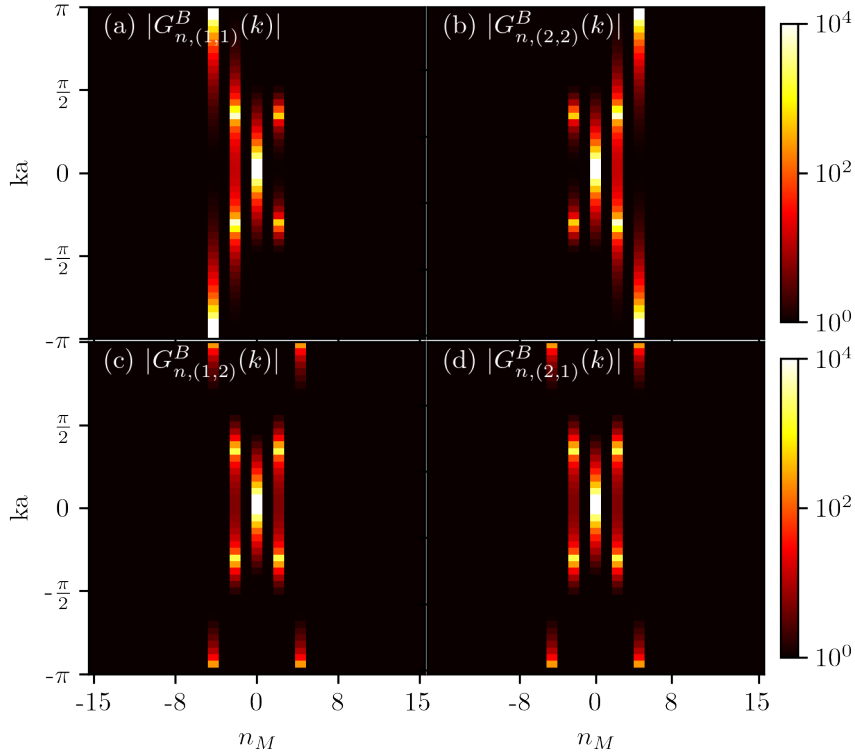
Figure 6.4: Green's function in Matsubara modes and momentum space calculated using Eq. (6.1). Results are for PBC, bosonic case, $\beta = 2\pi$, $\mu = 0$, $\alpha/t = 2.001$ and for 50 unit cells (and thus also 50 k-points). The top colorbar is for (a) and (b) and the bottom bar is for (c) and (d).
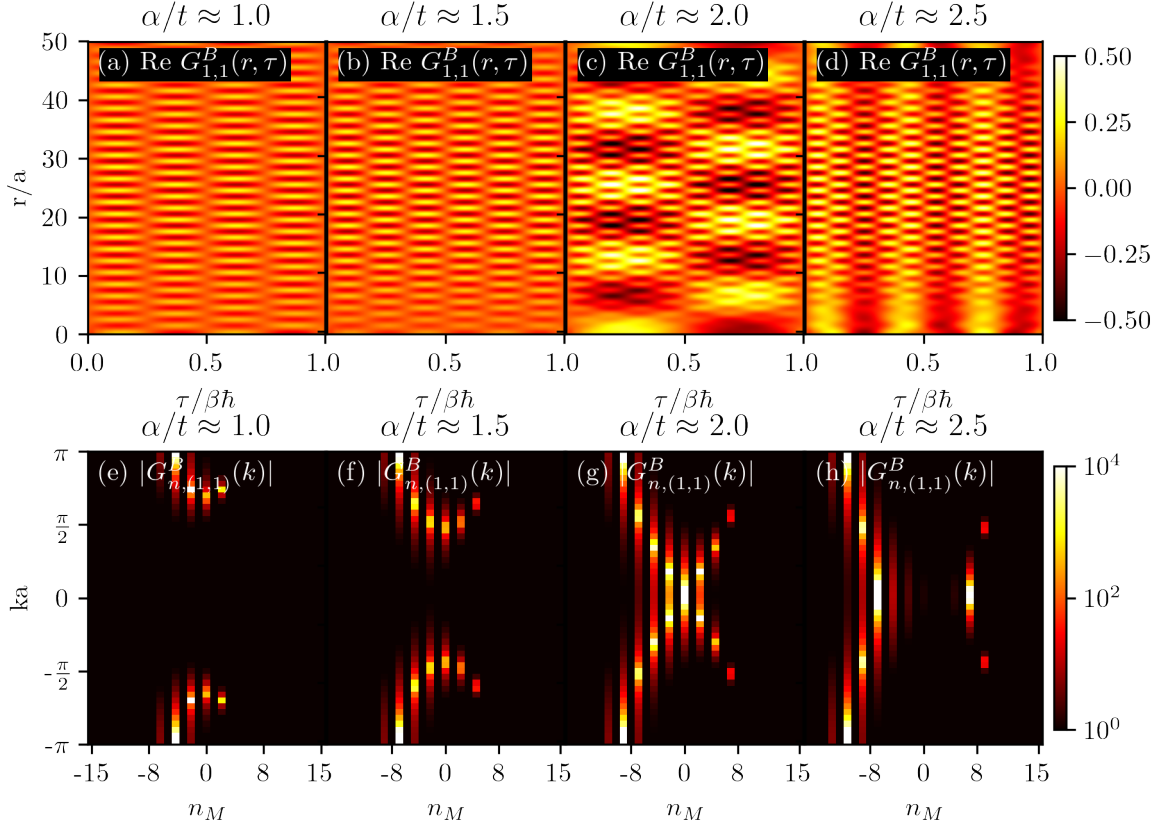
Figure 6.5: The $G_{1,1}^B$ Green's function for different values of α. Results are for PBC, bosonic case, $\beta = 4\pi$, $\mu = 0$ and for 50 unit cells (and thus also 50 k-points). We decreased the temperature for this figure in comparison to earlier figures to better highlight the effect on the poles in momentum space. We added 0.001 to every α to avoid divergences. (a)-(d) The Green's function as a function of position and imaginary time. (e)-(h) The Green's function as a function of momentum and Matsubara modes.

6.2.1   Alternating Gain and Loss

The simplest system with alternating gain and loss, discussed in Chapter 3, is the tight-binding model. The Hamiltonian of this system is given by

$$\hat{H} = -\sum_{j=0}^{M-1} \left(t\hat{c}_{j+1}^\dagger \hat{c}_j + t\hat{c}_j^\dagger \hat{c}_{j+1} + \alpha i(-1)^j \hat{c}_j^\dagger \hat{c}_j \right),$$

where t is the hopping amplitude and α the strength of the loss and gain. This results in a spectrum given by

$$\epsilon(k) = \pm\sqrt{-\alpha^2 + 2t^2 + 2t^2 \cos(ka)}.$$

By looking at Eq. (6.4), one can determine which criteria must be met for the parameters of the system to get an imaginary time crystal. This yields

$$\hbar\omega_n = \text{Im}\left(\sqrt{-\alpha^2 + 2t^2 + 2t^2 \cos(ka)} \right) \to \frac{\hbar\omega_n}{t} = \text{Im}\left(\sqrt{-\alpha^2/t^2 + 2 + 2\cos(ka)} \right).$$

After inserting Eq. (6.2), for bosons, we get

$$n_m = \frac{\beta t}{\pi} \text{Im}\left(\sqrt{-\frac{\alpha^2}{t^2} + 2 + 2\cos(ka)} \right).$$

Therefore, in the best case, when $k = \pm\pi$, the system has an iTC phase for all $|\alpha/t| > 0$. The only limit is the temperature, because for very small values of α/t, the temperature needs to be very low in order to observe the iTC phase. As can be seen in Eq. (6.4), if the imaginary part of the energy is small, β needs to be large (low temperature) in order for this equation to have nontrivial solutions. There is a complication that comes with these systems with two sites in the unit cell: instead of one Green's function there are now four. It is now possible to propagate from sublattice 1 to 1, from 1 to 2, from 2 to 1 and from 2 to 2, and these will be denoted by subscript i, j. These are calculated by replacing the Hamiltonian in Eq. (6.1) by the Bloch Hamiltonian.
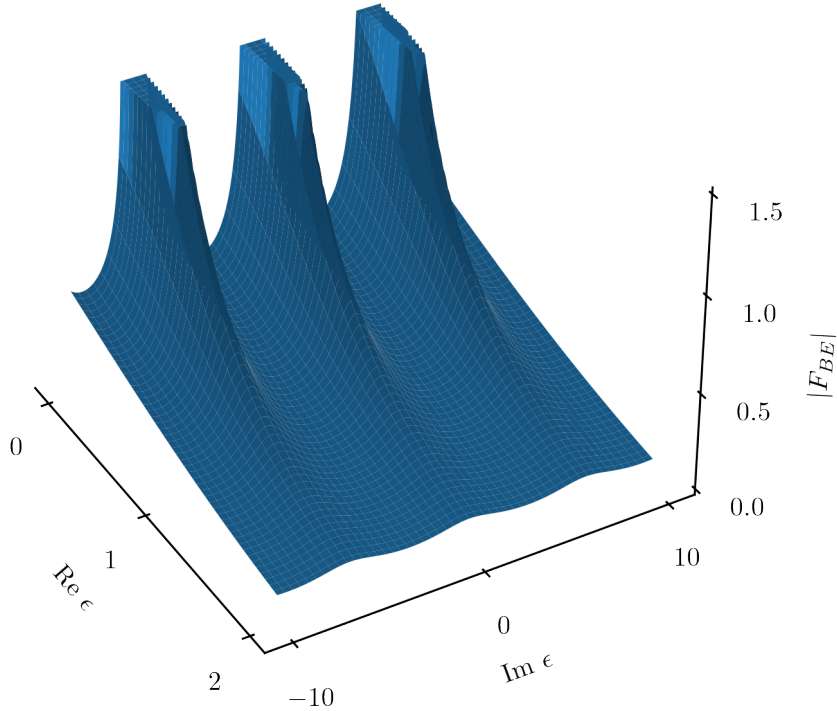
Figure 6.6: Bose-Einstein distribution for complex energies for $\beta = 1$ and $\mu = 0$. The function shows a clear periodicity in imaginary energy with a period of $2\pi/\beta$.

The Green's functions as a function of imaginary time and space are given in Fig. 6.3. Here, Figs. 6.3a and 6.3b clearly highlight the imaginary time crystal behaviour of this system. The system does not appear to oscillate at the same frequency for every sublattice combination, as can be noticed by the difference between Figs. 6.3a-b and Figs. 6.3c-d.

This can be further concluded by looking at Fig. 6.4. This figure shows the pole structure of the Green's function, as a function of Matsubara modes and momentum. The first thing we want to note about this figure is that Fig. 6.4a has an opposite structure to Fig. 6.4b. This can be explained by looking at the chain. The first site in the unit cell is lossy, while the second site has gain. Since the function $G^B_{n,(1,1)}(k)$ is a propagator from the first lattice site to the loss sites in other unit cells, it should be opposite to $G^B_{n,(2,2)}(k)$, since it only sees gain sites. The mixed sublattice Green's functions observe both loss and gain, and therefore combine the pole structure of both (1,1) and (2,2), as can be seen in Figs. 6.4c and 6.4d. The poles for the Matsubara modes $n_M = \pm 4$ are less strong than the poles at $n_M = \pm 2$. This is also the reason for the lower frequency of the oscillations, in Figs. 6.4c and 6.4d. To explain what happens for different values of the inverse temperature β, we look at Eq. (6.5), the definition of the Matsubara frequencies in Eq. (6.2), and the resonance condition in Eq. (6.4). Combining these yields that for larger values of β (lower temperature), the resonating Matsubara frequency increases.
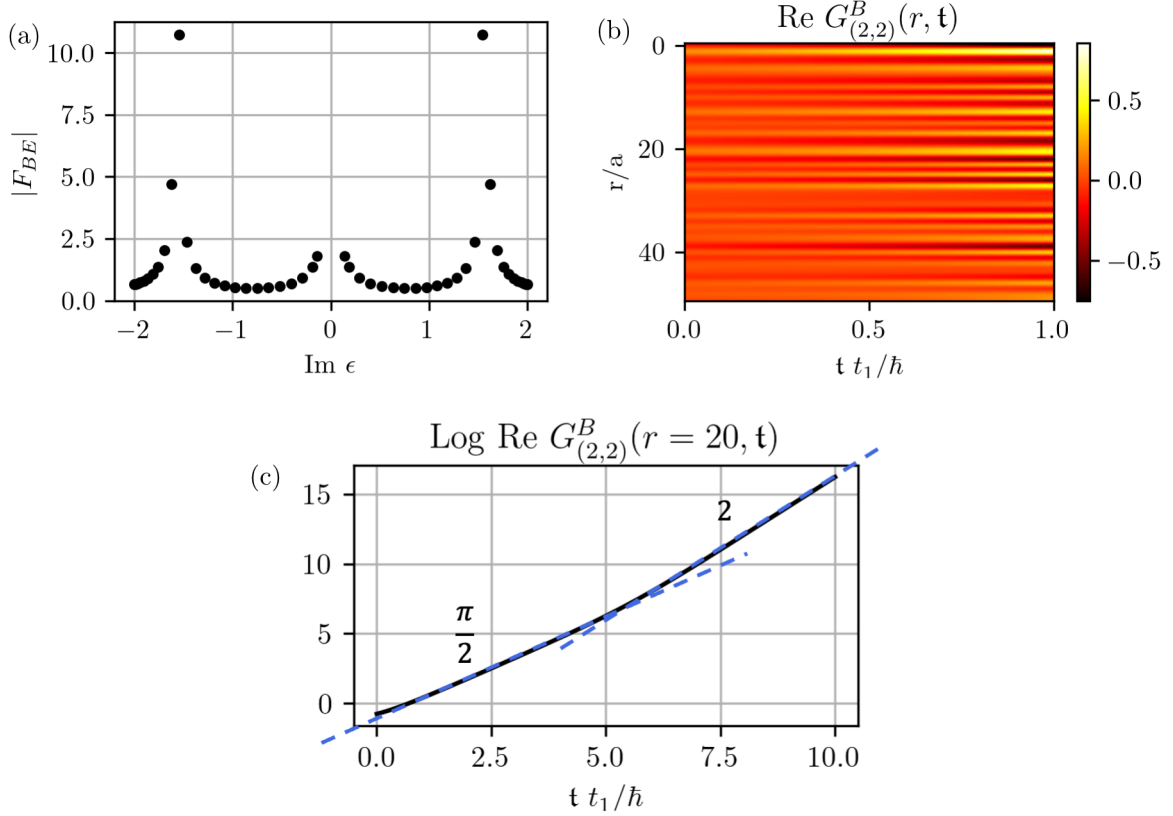
Figure 6.7: (a) Bose-Einstein distribution of the eigenvalues of a system of 50 unit cells, for $\beta = 4$ and $\alpha = 2.005$. This value of α was chosen because it causes a clear resonance for the first non-trivial Matsubara frequency. (b) The $G_{2,2}^B$ Green's function as a function of position and real time, for $\beta = 4$, $\alpha = 2.005$ and 50 unit cells. These results are for PBC. (c) Extending the time for the real-time Green's function for a single x-position. This clearly shows the change in slope.

Therefore, there are more oscillations in the imaginary time interval from 0 to $\hbar\beta$. It is also instructive to study the behaviour of the system for different values of the loss/gain variable α. Some examples of this can be seen in Fig. 6.5. What immediately comes to attention is how the poles for the positive and negative momenta 'meet' for $\alpha/t = 2$ in Fig. 6.5g. This can be easily understood by looking at the Green's function of Eq. (6.1). This function has poles (for $\mu = 0$) at

$$i\hbar\omega_n = \epsilon(k) = \pm\sqrt{-\alpha^2/t^2 + 2 + 2\cos(ka)}.$$

In this case, we are looking for solutions for $ka = 0 \ \wedge \ n_M = 0$. Again, using the definition for the Matsubara modes of Eq. (6.2) for bosons, we obtain

$$\sqrt{-\alpha^2/t^2 + 2 + 2} = 0 \to \alpha/t = \pm 2.$$

Thus, we see that for $\alpha/t = 2$, there is a pole for zero momentum and $n_M = 0$ (there is also a negative solution but since the system is symmetric for positive/negative α, we will keep the notation easy and only focus on the positive side). Notice how, for $\alpha/t > 2$, the poles start to move away from each other (see Fig. 6.5h), but will now move along the Matsubara 'axis', as opposed to the momentum axis. In addition to this, the figure also illustrates how the amount of oscillations in imaginary time increases with α, due to the imaginary energy of the system increasing with α.
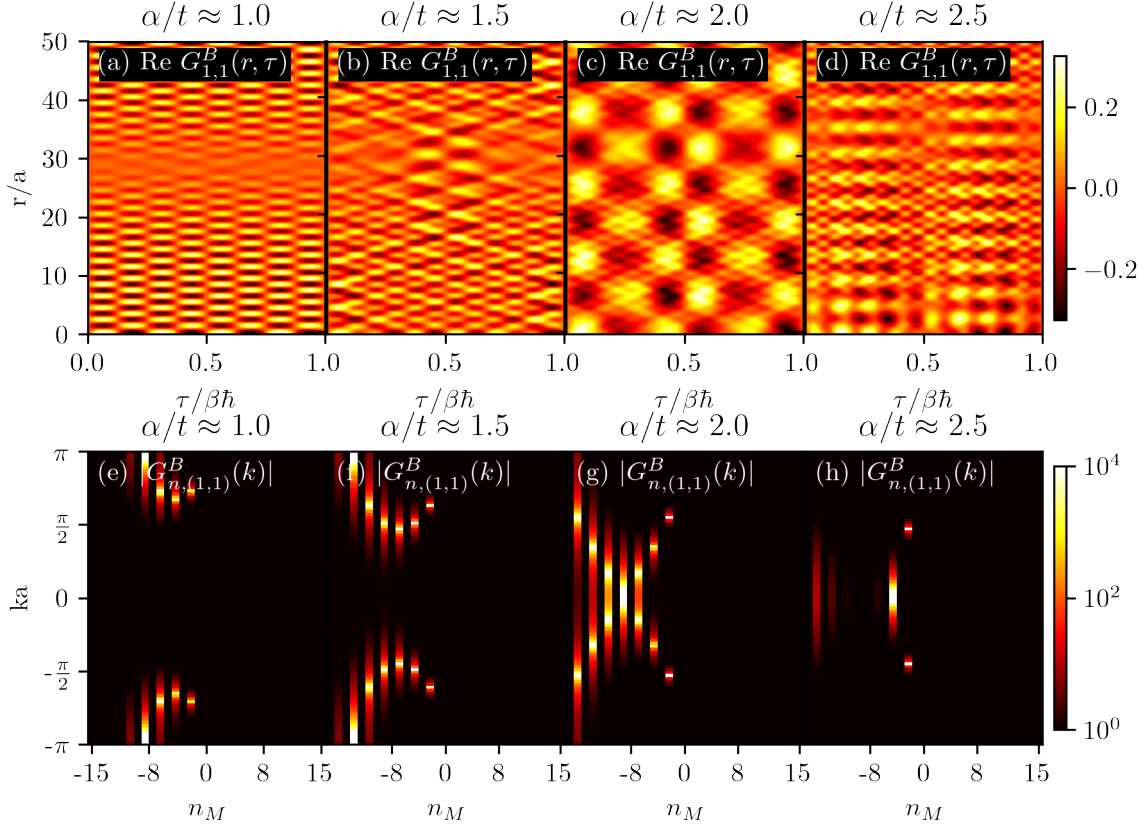
Figure 6.8: The $G_{1,1}^B$ Green's function for different values of α. Results are for PBC, bosonic case, $\beta = 4\pi$, $\mu = 0$ and for 100 lattice sites (and thus also 100 k-points). This is equivalent to 50 unit cells. We added 0.001 to every α to avoid divergences. (a)-(d) The Green's function as a function of position and imaginary time. (e)-(h) The Green's function as a function of momentum and Matsubara modes.

Real Time Behaviour

Until now, we have seen how gain/loss systems can give rise to imaginary time crystal phases, with oscillations related to Matsubara modes. In order to relate this to observables, which can be experimentally verified, we would like to rotate back to real time. Wick rotating Eq. (6.5) suggests that the Green's function will decay/increase exponentially, depending on the pole structure. However, this equation is just an approximation. Ref. [58] provides an equation for the real time Green's function, for fermionic particles for a Hermitian system. One could then promptly show that the expression for bosonic particles, for a non-Hermitian Hamiltonian, is given by

$$G(\mathsf{t}) = \sum_m \phi_m^R \phi_m^{L\dagger} F_{\text{BE}}(\epsilon_m, \beta, \mu) e^{-i\epsilon_m \mathsf{t}}, \tag{6.6}$$

where $F_{\text{BE}}(\epsilon_m, \beta, \mu)$ is the Bose-Einstein distribution for bosonic particles: $F_{\text{BE}} = \left(e^{\beta(\epsilon - \mu)} - 1\right)^{-1}$. This equation is only valid if $\epsilon - \mu > 0$, and therefore μ must be equal to the lowest real energy of the system. One can readily see in Eq. (6.6) that this Green's function will oscillate for real eigenvalues and decay/increase exponentially for imaginary eigenvalues. By studying the behaviour of the Bose-Einstein distribution for complex eigenvalues, we can discover how the pole structure, an example of which can be seen in Fig. 6.4, is encoded in this equation. An illustration of this can be found in Fig. 6.6. The function is periodic in the imaginary part of the energy, with a periodicity of $2\pi/\beta$. The divergences along the imaginary axis correspond to the Matsubara modes of Eq. (6.2), satisfying $\beta(\epsilon - \mu) = 0$. In

the thermodynamic limit, Eq. (6.6) can be approximated by a sum over only the resonating Matsubara modes, yielding Eq. (6.5), due to this Bose-Einstein distribution effectively acting as a delta distribution.

In Fig. 6.7a, the Bose-Einstein distribution is given as a function of the eigenvalues, for the alternating gain and loss system of Eq. (3.2). This reveals that for this choice of parameters ($\beta = 4^1$, $\alpha = 2.005$), the system has a Matsubara frequency at $2\pi/4 \approx 1.57$ (see Eq. (6.2)). This is indeed the location of the peaks in Fig. 6.7a. Based on Eq. (6.6), this system should increase exponentially, with the dominant term being this Matsubara frequency. This is indeed the case, as seen in Fig. 6.7b, where the real time Green's function is depicted. Taking the logarithm of the figure and calculating the slope yields $d\log(G)/d\mathfrak{t} \approx 1.57$. So, indeed, this is the case. However, an important remark must be made here. Eq. (6.6) shows that non-resonating modes of the system are only initially suppressed by the Bose-Einstein distribution. Over longer time scales, these stronger exponentials will still dominate the behaviour of the system. Indeed, when we extend the time of Fig. 6.7b by a factor of 10, the slope equals α, as it can be seen in Fig. 6.7c. In this case, we also studied the (2,2) Green's function. This is because, as can be seen in Fig. 6.4, the (1,1) Green's function also contains positive Matsubara modes, besides a major negative contribution. These positive Matsubara modes make it very difficult to properly measure the decay of this function. Therefore, it is easier to study the exponentially increasing (2,2) Green's function.

6.2.2 Alternating Loss

As already discussed in Chapter 3, the tight-binding model with alternating loss is similar to the model with alternating gain and loss, but with an overall imaginary shift. In Fig. 6.8, this manifests itself as a shift of the Matsubara modes into the negative part of the domain. The overall pole structure remains the same, but the modes at which they occur have shifted by a factor of α. Therefore, this system oscillates at twice the frequency in imaginary time, with respect to Fig. 6.5. We also see this effect in Fig. 6.9a, where it becomes clear that the system decays fast. Here, the graph shows a peak near Im $\epsilon \approx -3.14$. By evaluating the Green's function at a single r coordinate and measuring the slope of the logarithm of the function, we find that the slope is equal to -3.14 ($\approx \pi$).
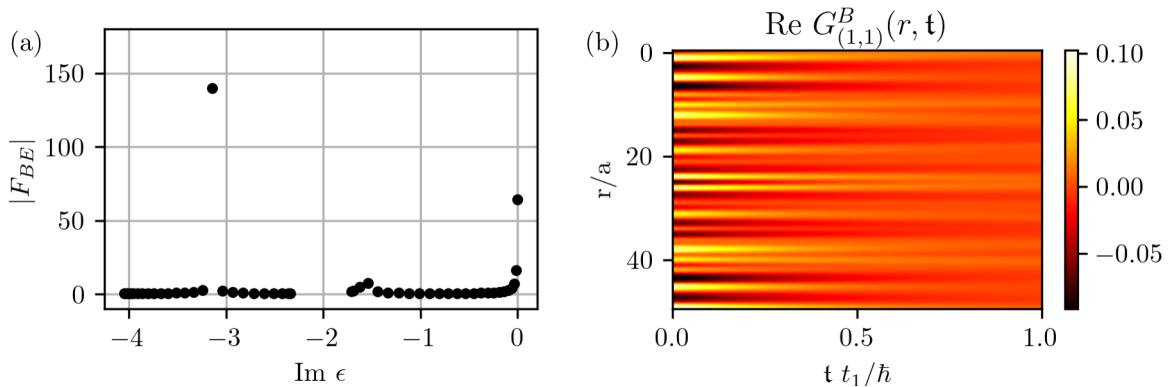

Figure 6.9: (a) Bose-Einstein distribution of the eigenvalues of a system of 50 unit cells for $\beta = 4$ and $\alpha = 2.024$. This value of α was chosen because it causes a clear resonance for the first non-trivial Matsubara frequency. (b) The $G^B_{1,1}$ Green's function as a function of position and real time, for $\beta = 4$, $\alpha = 2.024$ and 50 unit cells. These results are for PBC.

---

[1]In this case, the value for β was not a multiple of 2π, unlike in other figures. β being a multiple of 2π has the effect that the Matsubara frequencies become rational numbers. However, in this case, it would hamper the proof that these systems decay/increase exponentially with Matsubara frequencies, as the highest Matsubara frequency will now only be equal to α. If β is not a multiple of π, this is no longer a problem.
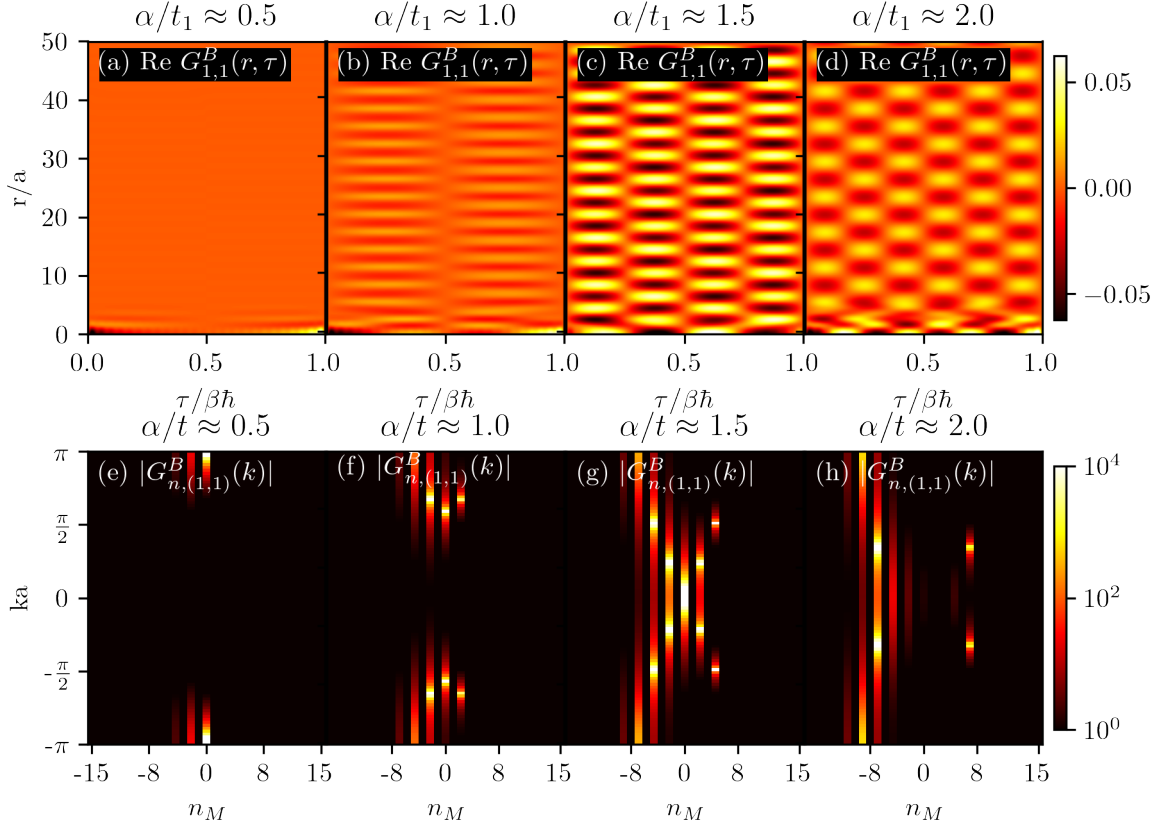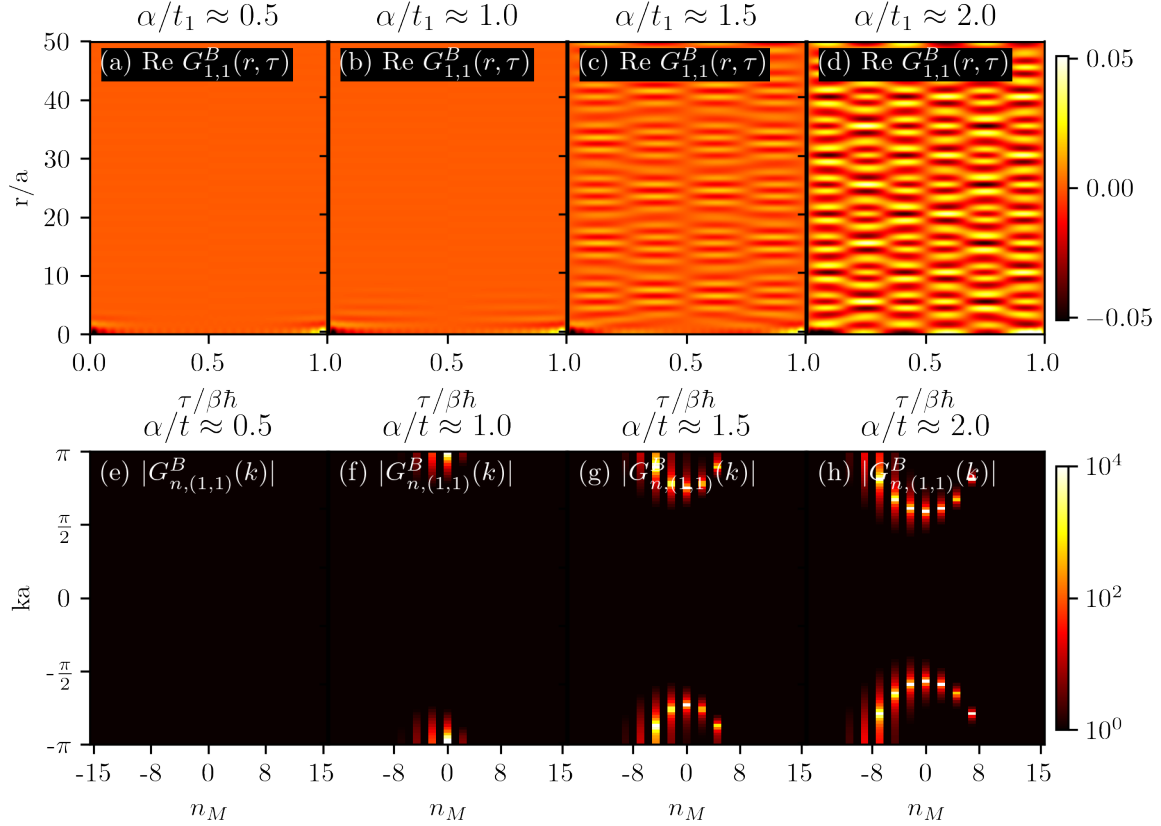
Figure 6.10: The $G_{1,1}^B$ Green's function for different values of α. Results are for PBC, bosonic case, $\beta = 4\pi$, $\mu = 0$, $t_2 = 1/2$ and for 100 lattice sites (and thus also 100 k-points). This is equivalent to 50 unit cells. We added 0.001 to every α to avoid divergences. (a)-(d) The Green's function as a function of position and imaginary time. (e)-(h) The Green's function as a function of momentum and Matsubara modes.

6.2.3 SSH Model with Loss

We can also study the Green's functions of the SSH models presented in Chapter 3. On the basis of their spectra, we can already predict that they will look very similar to the tight-binding results shown above, with the addition that the SSH model can have a $\mathcal{PT}$-symmetric region. In this region, the system has real eigenvalues, and thus it does not exhibit an imaginary time crystal phase. In Fig. 6.10, we show the Green's function for the trivial phase of the SSH model with alternating gain and loss, and in Fig. 6.11, we show the topological regime of the SSH model with alternating gain and loss. These figures clearly highlight the different sizes of the $\mathcal{PT}$-symmetric regions for both systems. As we can recall from Chapter. 3, this SSH model is $\mathcal{PT}$-symmetric when $\alpha < |t_1 - t_2|$. In the case of the system of Fig. 6.10, this transition occurs at $\alpha = 1/2$, and this is indeed visible in the pole structure. In Fig. 6.11, this transition occurs at $\alpha = 1$, and at $\alpha \approx 0.5$ no poles are visible.

6.2.4 Gain and Loss at the Edge

In Chapter 3, we discussed a few different variations of open boundary systems with gain or loss near the edge. There we saw that their spectra are not very different from the PBC case, but that they have fewer imaginary modes, corresponding to the gain/loss sites. Of the four different systems discussed there, we would like to highlight one special case, the system of Fig. 3.11. This system only has a few imaginary modes, due to the limited amount of gain/loss sites, but also is not $\mathcal{PT}$-symmetric. This results in a

Figure 6.11: The $G_{1,1}^B$ Green's function for different values of α. Results are for PBC, bosonic case, $\beta = 4\pi$, $\mu = 0$, $t_2 = 2$ and for 100 lattice sites (and thus also 100 k-points). This is equivalent to 50 unit cells. We added 0.001 to every α to avoid divergences. (a)-(d) The Green's function as a function of position and imaginary time. (e)-(h) The Green's function as a function of momentum and Matsubara modes.

special spectrum, with the interesting property that the positive and imaginary modes are asymmetrically located around the real axis. Therefore, this system could resonate with either the positive or negative imaginary modes, depending on the temperature. For a certain temperature, the Green's function would increase, and for a different temperature, the system would decay. This is illustrated in Fig. 6.12, where the plots on the left and right show the pole structure for different temperatures, and the middle plot shows the spectrum and the energies with which they resonate. However, in practice, it would be difficult to measure this behaviour due to (relatively) large real modes still present in the system. Only for very high values of loss and gain this behaviour emerges. For a complete overview of Green's functions for systems which were not or partially covered in this chapter, see appendix C.

6.3 Thermodynamic Analysis

Apart from the aforementioned Green's functions, the imaginary time crystal phase also has signatures in thermodynamic quantities [10], such as the free energy F and the entropy S. By looking at the partition function for bosons [12],

$$\mathcal{Z} = \prod_m \frac{1}{1 - e^{-\beta \epsilon_m}},$$
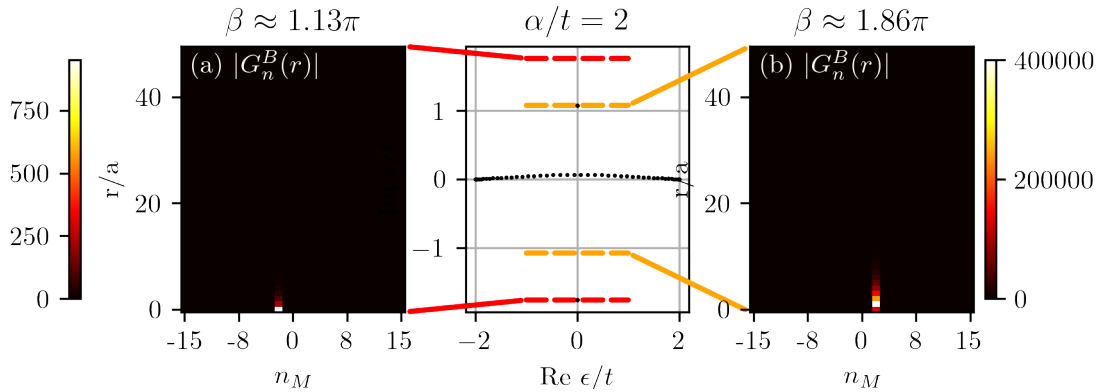
Figure 6.12: Green's function as a function of position and Matsubara modes. Results are for OBC, bosonic case, $\alpha/t = 2$, $\mu = 0$ and for 50 lattice sites. The plot on the left and right show the pole structure for different temperatures, and the middle plot shows the spectrum and the energies with which they resonate.

where we set the chemical potential to zero, we immediatly see the effect of non-Hermitian quantum physics on statistical mechanics. The partition function will oscillate as a function of temperature, due to the imaginary argument of the exponent [14]. As most thermodynamic quantities can be directly derived from the partition function, this greatly affects the thermodynamic behaviour. To study the effect of non-Hermiticity on this, we will first derive the necessary equations. The most straightforward is the internal energy U, which is given by $U = -\partial \log(\mathcal{Z})/\partial \beta$ [12]. This yields

$$U = \sum_m \epsilon_m \frac{1}{e^{\beta \epsilon_m} - 1} = \sum_m \epsilon_m F_{BE}(\epsilon_m, \beta),$$

where F_{BE} is again the Bose-Einstein distribution. The free energy is given by $F = -(1/\beta)\log(\mathcal{Z})$ [12], and therefore,

$$F = \frac{1}{\beta} \sum_m \log\left(1 - e^{-\beta \epsilon_m}\right).$$

Finally, the entropy is given by $S/k_B = \beta^2(\partial F/\partial \beta)$ [12]. This gives

$$\frac{S}{k_B} = -\beta F + \beta U.$$

The free energy, internal energy, and entropy can be calculated for the SSH model with alternating (gain and) loss, for both the trivial and topological phases. The trivial SSH chain ($|t_2/t_1| = 0.5$) with alternating gain and loss can be seen in Fig. 6.13. The results for the topological regime of this model are depicted in Fig. 6.14. The SSH chain with alternating loss in the trivial regime, can be seen in Fig. 6.15, and the topological regime in Fig. 6.16. Just as for the real time Green's function, the chemical potential was set to the smallest real energy component of the spectrum, in order for the Bose-Einstein distribution to behave well. In all four figures, it is clear that in the full non-Hermitian limit, where the entire spectrum is imaginary, the depicted quantities oscillate as a function of temperature. Besides the aforementioned oscillations of the Green's function in imaginary time, the oscillations in the thermodynamic quantities are a second import signature of the iTC phase. Unlike the case of the Hatano-Nelson model [14], there is no significant difference between OBC and PBC for these systems. This is to be expected, since the spectrum changes dramatically depending on the boundary conditions for the Hatano-Nelson model. This is not the case for the non-Hermitian SSH model. In Fig. 6.13, we can see that when $\alpha/t_1 = 2$, the system is periodic with a periodicity of roughtly π. This is because, for this α/t_1 value, the spectrum of the system is entirely imaginary, with an imaginary line gap. The maximum

and minimum imaginary components of one of the bands are about 2 and $\frac{4}{3}$. The maximum of 2 explains the periodicity of π, since $e^{n\pi 2i} = e^{2\pi i}$. There is also an additional peak visible at $\beta = 3\pi/2$. This is explained by the eigenvalue of $4/3$, since $e^{n\frac{3\pi}{2}\frac{4}{3}i} = e^{2i\pi}$. A similar reasoning can be applied to Fig. 6.14, but now with a periodicity of $2\pi/3$. In Figs. 6.15 and 6.16, which are the systems only containing loss, the entire spectrum is shifted down by α. Therefore, in both the case where the spectrum is partly imaginary and fully imaginary (centre and right column), the system is always periodic in $2\pi/\alpha$, besides the eigenvalue-based resonances. Overall, there does not appear to be a clear distinction between the thermodynamic behaviour of the topological and trivial regimes of the SSH model. The only visible differences depend on the magnitude of t_1 and t_2, and does not depend on which is larger than the other.
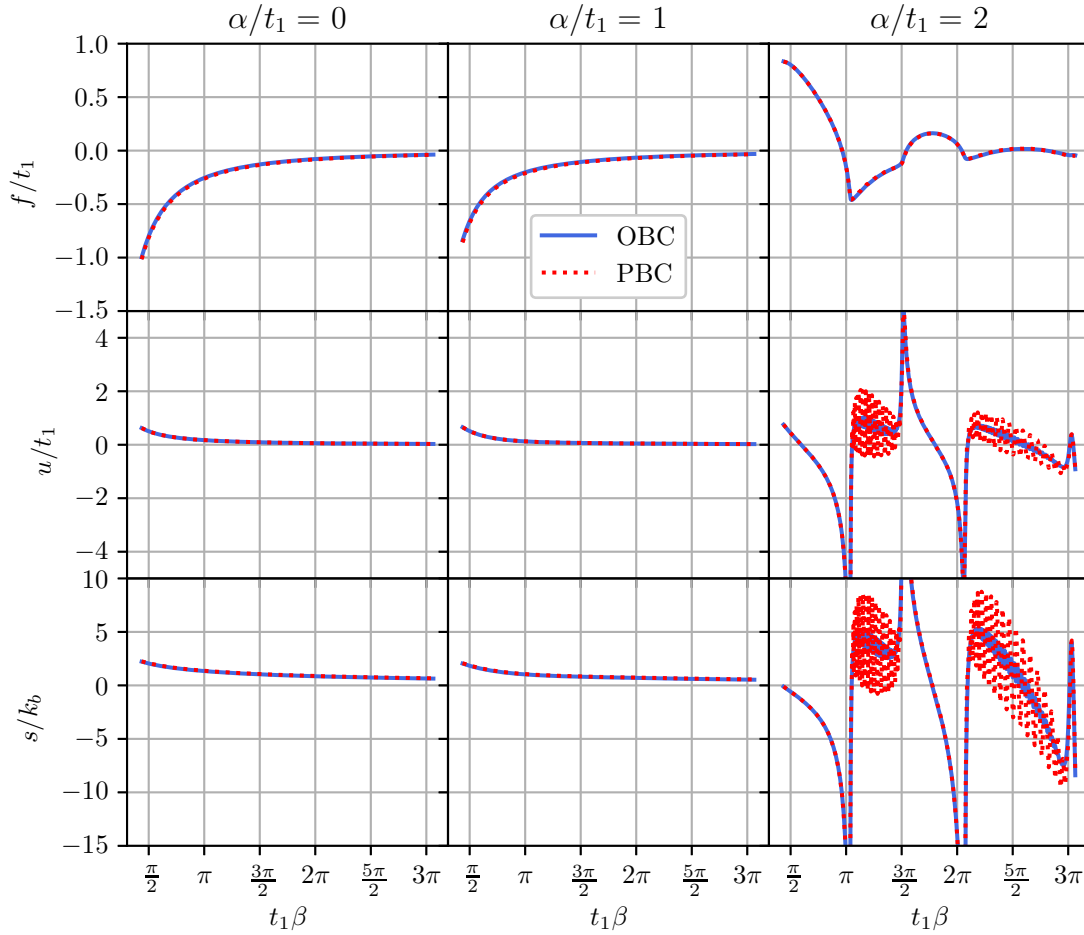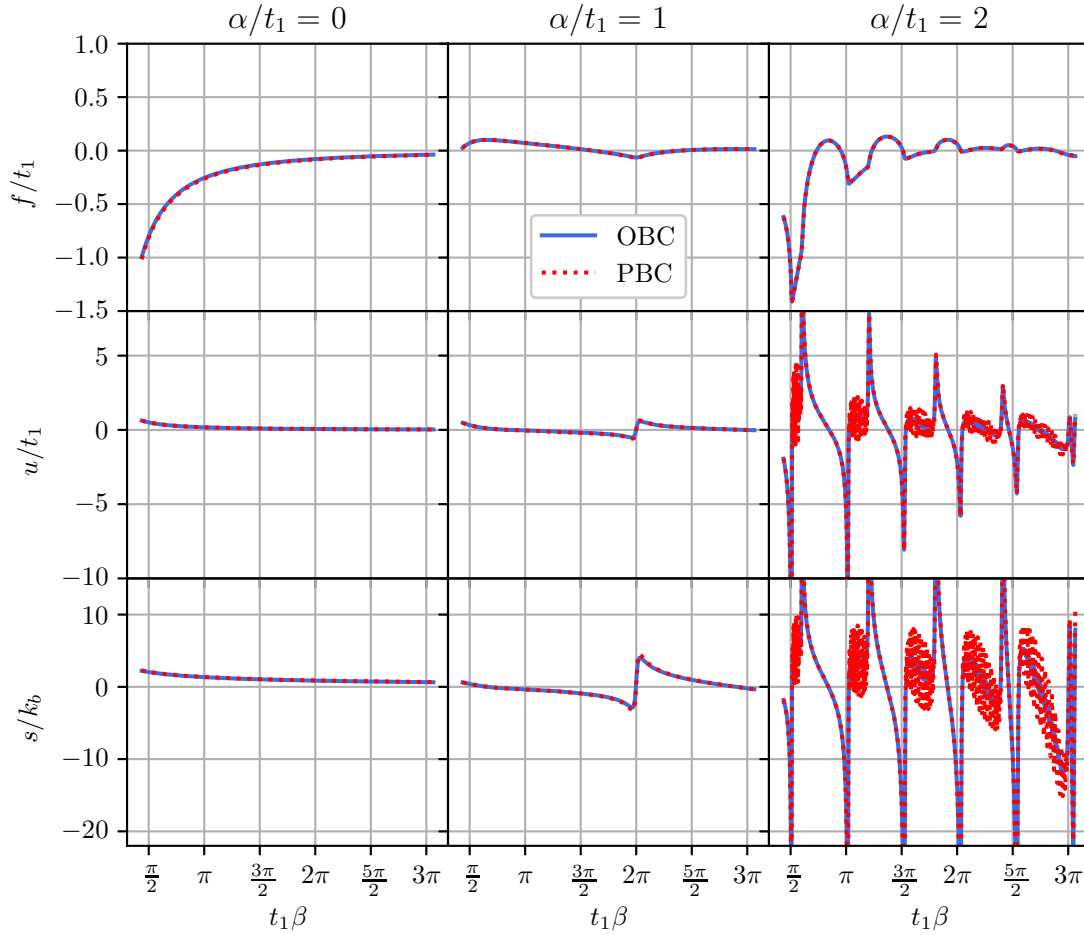
Figure 6.13: The free energy, internal energy and entropy, per unit cell, for the trivial SSH model ($t_2/t_1 = 0.5$) with alternating gain and loss, for three different gain/loss strengths. Blue is OBC, red dotted is PBC. A system of 50 unit cells was used for both boundary conditions. In the Hermitian limit (left column), the free energy, internal energy, and entropy are not oscillating. If the $\mathcal{PT}$-symmetry is broken (middle column), imaginary modes appear, but because the chemical potential is still large, the imaginary modes are not highly occupied. Therefore, there are no oscillations visible. For an entirely imaginary spectrum (right column), there are more imaginary modes, and the chemical potential has nearly vanished, and so the oscillations are visible.
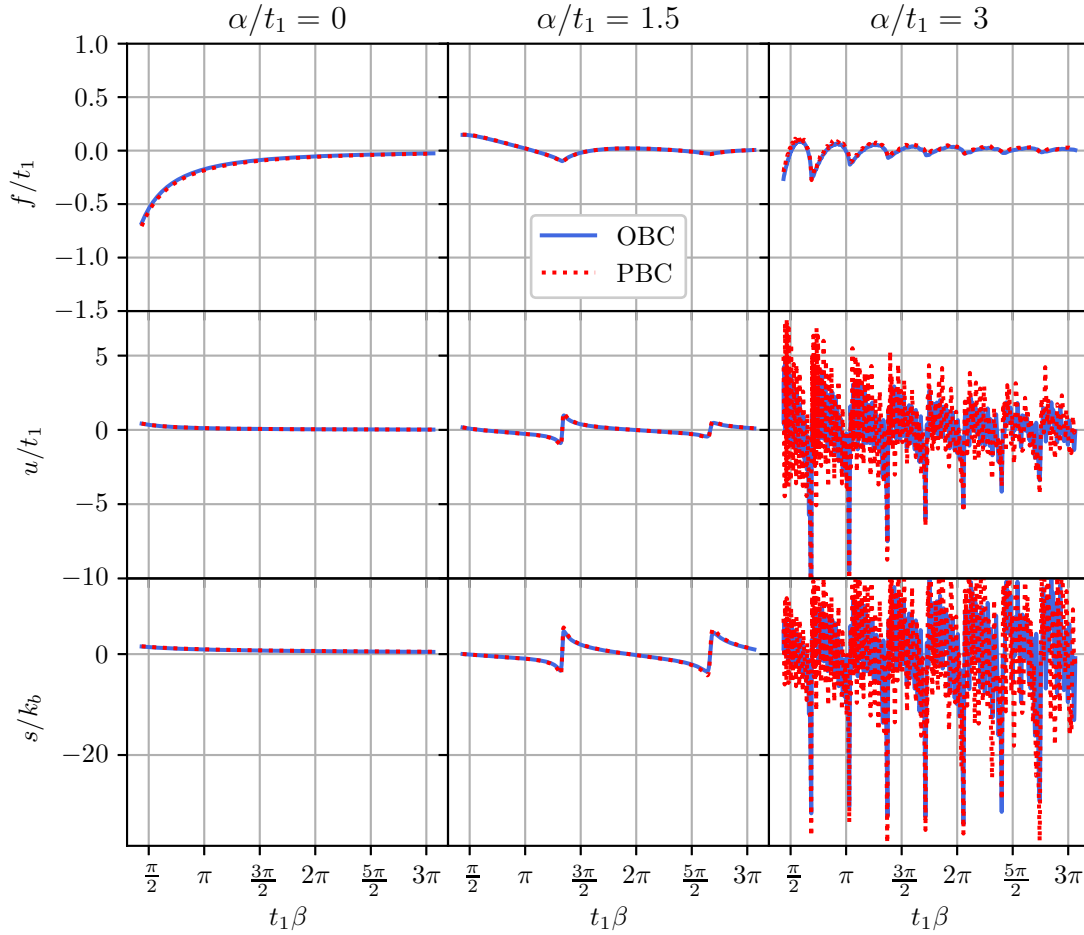
Figure 6.14: The free energy, internal energy and entropy, per unit cell, for the topological SSH model ($t_2/t_1 = 2$) with alternating gain and loss, for three different gain/loss strengths. Blue is OBC, red dotted is PBC. A system of 50 unit cells was used for both boundary conditions. In the Hermitian limit (left column), the free energy, internal energy, and entropy are not oscillating. If the $\mathcal{PT}$-symmetry is broken (middle column), imaginary modes appear, but because the chemical potential is still large, the imaginary modes are not highly occupied. Therefore, there are no oscillations visible. For an entirely imaginary spectrum (right column), there are more imaginary modes, and the chemical potential has nearly vanished, and so the oscillations are visible.

Figure 6.15: The free energy, internal energy and entropy, per unit cell, for the trivial SSH model ($t_2/t_1 = 0.5$) with alternating loss, for three different loss strengths. Blue is OBC, red dotted is PBC. A system of 50 unit cells was used for both boundary conditions. In the Hermitian limit (left column), the free energy, internal energy, and entropy are not oscillating. If the $\mathcal{PT}$-symmetry is broken (middle column), imaginary modes appear, but because the chemical potential is still large, because the spectrum still has real parts. However, since the imaginary component is larger, due to the imaginary offset, there are already oscillations visible. For an entirely imaginary spectrum (right column), the spectrum is entirely imaginary and thus, a lot of oscillations are visible.

Figure 6.16: *The free energy, internal energy and entropy, per unit cell, for the topological SSH model ($t_2/t_1 = 2$) with alternating loss, for three different loss strengths. Blue is OBC, red dotted is PBC. A system of 50 unit cells was used for both boundary conditions. In the Hermitian limit (left column), the free energy, internal energy, and entropy are not oscillating. If the $\mathcal{PT}$-symmetry is broken (middle column), imaginary modes appear, but because the chemical potential is still large, because the spectrum still has real parts. However, since the imaginary component is larger, due to the imaginary offset, there are already oscillations visible. For an entirely imaginary spectrum (right column), the spectrum is entirely imaginary and thus, a lot of oscillations are visible.*

Chapter 7

Conclusion & Outlook

7.1 Conclusion

To conclude, we investigated multiple properties of non-Hermitian systems, specifically focussing on optical gain and loss systems. We looked at both the spectral and thermodynamical properties of these systems, and specifically the ones influenced by the non-Hermiticity. We started by giving an introduction to non-Hermitian quantum physics in Chapter 2. There, we discussed the difference between Hermitian and non-Hermitian operators, and discussed the biorthogonal basis. This is a consequential necessity of non-Hermiticity, due to the fact that the normal right eigenvector basis is no longer orthogonal. Next, we introduced the notion of pseudo-Hermitian operators and came to the very important concept of $\mathcal{PT}$-symmetric operators, which played a big role in the rest of the thesis. After this, we gave a mathematical motivation behind non-Hermitian physics as an effective tool for modelling open systems. These are systems that are in contact with an environment. There, we gave two methods of achieving a non-Hermitian Hamiltonian, using the Lindblad or the self-energy formalism. After this, we discussed exceptional points, which are special points in the parameter space of a system, where multiple eigenvalues and eigenvectors coalesce. To end the chapter, we presented a commonly discussed non-Hermitian system, namely the Hatano-Nelson model, which acquires its non-Hermiticity due to non-reciprocal hopping.

In Chapter 3, we started investigating gain and loss systems. We analysed multiple versions of tight-binding models with on-site gain or loss, and discussed how these systems can be $\mathcal{PT}$-symmetric, as well as how they can host exceptional points. This was followed by an investigation of tight-binding chains with only loss. We showed how systems with alternating loss are related to systems with alternating gain and loss. At the end of the chapter, we also briefly discussed a few systems with gain and/or loss placed at the edges of OBC chains. We learnt that these systems are not fundamentally different from systems with PBC. This led to Chapter 4, which is based on a manuscript written during this thesis [1]. Here, we discuss how to create a topological monomode using loss in an SSH chain. We find that only introducing one loss site in the chain is sufficient to obtain a monomode. This is supported by experimental results in photonic lattices, for both the 1D and 2D SSH models. We find that these experimental results are in agreement with the numerical results, based on the tight-binding calculations. In Chapter 5, the quantum geometric tensor was discussed. This is a method of measuring the distance between eigenstates of a system in Hilbert space. We started the chapter with a Hermitian example of quantum geometry, by showing the metric tensor for the Hermitian SSH system. After this, we added gain and loss to the SSH chain, resulting in a non-Hermitian system. This allowed us to calculate a phase diagram, which we found by inspecting the spectra in Chapter 3. Finally, we also briefly showed results for the 2D SSH model, finding that there is no notable difference in the phase diagram between these models.

In the second part of the thesis, Chapter 6, we discussed the imaginary time crystal phase. This is a

special phase that, like crystals in space, oscillates in imaginary time. We find that these oscillations in imaginary time correspond to exponential gain/decay in real time. We start the chapter by discussing previous work done on imaginary time crystals, namely the Hatano-Nelson model [14]. After this, we presented the imaginary time crystal phase in the optical gain and loss systems, by studying their Green's functions. Here, we calculated the Green's function for different bases, one of those being the Green's function as a function of real time and space. These give a measurable quantity that can be experimentally verified. This is followed by investigating the behaviour of thermodynamical properties, which oscillate as a function of temperature, due to the imaginary time crystal phase.

7.2   Outlook

A natural extension on the work on topological monomodes (Chapter 4), would be to investigate the creation of monomodes in other systems. For example, it would be interesting to try to create monomodes in other topological systems, in which corner modes come in pairs. Some examples are the quantum spin Hall effect or the Kitaev chain. In addition, engineered loss can also be used to target desired states. This was used in Ref. [59] to obtain only corner states, upon engineering the system such that the bulk modes decay.

Secondly, experimental verification of the existence of the imaginary time crystal phase would be interesting. Usually, the temperature is a difficult constraint on the experiment, because the temperature needs to be in an intermediary range, since the imaginary part of the energy should be an integer of $\pi k_B T$. So, for measuring the imaginary time crystal phase using photonics, the temperature of the thermal light would need to be sufficiently low. If this could be achieved, there are multiple methods of measuring the imaginary time crystal phase. The first would be to measure the amplitude or intensity correlation functions. Since the Green's function is effectively the amplitude correlation function, they should show the same behaviour. One could also measure any thermodynamic quantity. These should oscillate as a function of temperature, as discussed in Chapter 6. One would not specifically need to vary the temperature to achieve this. In the tight-binding model, increasing the loss or gain, while keeping the temperature constant, would also allow for achieving this aim.

Acknowledgements

I first and foremost want to thank my daily supervisors, Lumen Eek and Rodrigo Arouca. Working with you has truly been the most fun I have ever had during a project. We could always joke with each other, even at the most desperate of times. Rodrigo, even though we have not seen each other face to face, it already feels like I have known you for years. You were always ready to explain any concepts I needed help understanding. You blew me away with your knowledge of the literature on the subject. You were always there if I needed a paper on a specific topic. You were also always quick to make corrections and suggestions to things I sent you. You will be an assistant professor very soon. Lumen, of course, I had already known you before I started my thesis. One could even say you 'arranged' this master thesis for me. I especially enjoyed working with you when you were in Enschede, or I was in Utrecht, when we both got enthusiastic about a subject and wanted to calculate things as fast as possible. This thesis could not have happened without you.

I also want to thank my supervisor, Cristiane Morais Smith. Even though you can be extremely busy sometimes, you are the most involved supervisor I know. You are also the most all-round supervisor I know. Not only did you teach me a lot of physics during sometimes long meetings where we discussed a subject, but you also taught me a lot about academic writing and presenting. These important aspects can quickly be overlooked by other supervisors. I will also fondly remember the group activities you initiated, with the highlight being the Sinterklaas party you hosted. Your students are like family to you.

I also want to thank my supervisor from the University of Twente, Jan Klärs. Although we did not have many meetings, they were always useful and pragmatic. Although we did not get to do the experiments we hoped to do, we can hopefully finish this project in the future.

I also want to thank Rembert Duine and Pepijn Pinkse for being my second supervisors for this thesis.

I also want to thank all the CMS group members for their warm welcome and the shared activities. Noteworthy was, of course, my second place in the bowling competition.

Appendices

Appendix A

Complete Measurements

Figs. A.1 and A.2 show the full experimental data of the 1D chain experiments, obtained upon inserting light in each waveguide.
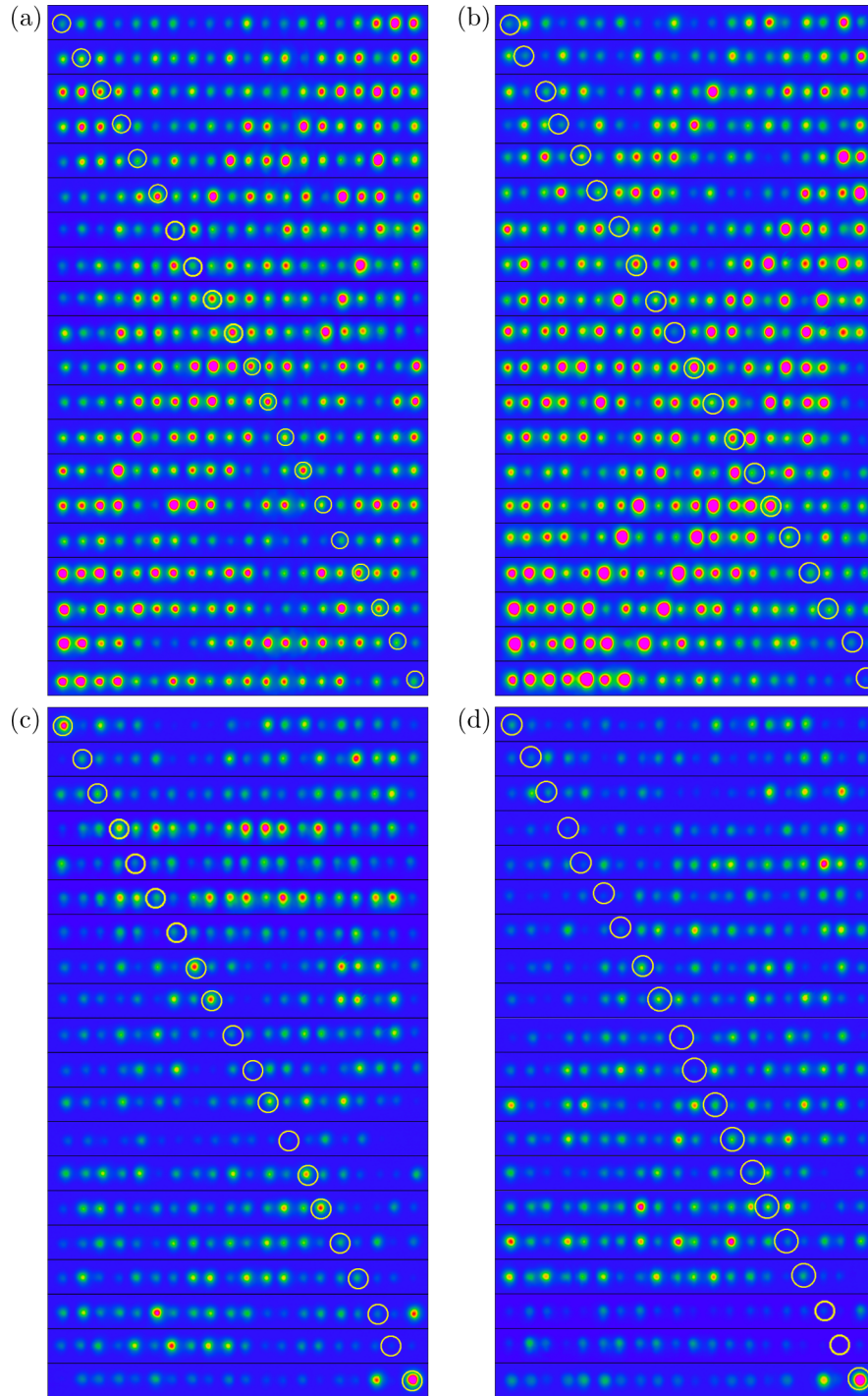
Figure A.1: Experimental results for all insertion points. (a) Results of the tight-binding chain with no loss, from Fig. 4.7a. (b) Results of the topologically trivial chain with no loss, from Fig. 4.7b. (c) Results of the topological chain with no loss, from Fig. 4.7c. (d) Results of the topological chain with loss, from Fig. 4.7d. Figure taken from Ref. [1].
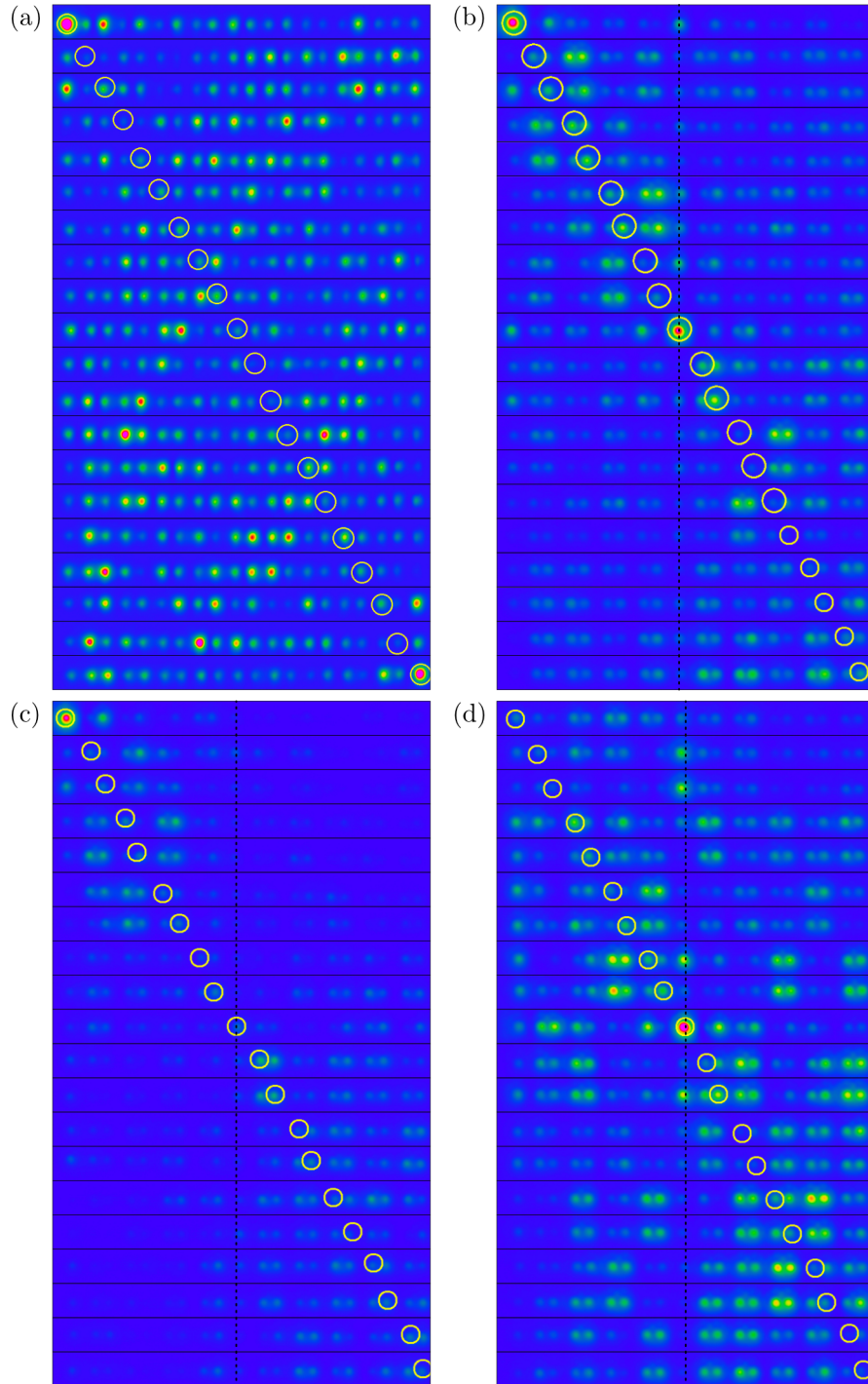
Figure A.2: Experimental results for all insertion points. (a) Results of the topological chain with loss on the "wrong" (far away) side of the lattice, from Fig. 4.8a. (b) Results of the topological defect chain with no loss, from Fig. 4.8b. The position of the topological defect is indicated by a dotted line. (c) Results of the topological defect chain with loss engineered in a way to destroy the defect mode, from Fig. 4.8c. (d) Results of the topological defect chain with loss designed to destroy the left edge mode, from Fig. 4.8d. Figure taken from Ref. [1].

Appendix B

Floquet Time Crystals

The imaginary time crystals discussed in Chapter 6 allow us to measure decay or gain with amplitudes equal to Matsubara modes. However, they pose a problem, in the sense that optical systems do not have a temperature in the way that a fermionic system has a temperature. Because imaginary time is defined on an interval from 0 to $\hbar\beta$, and because Matsubara modes are also controlled by temperature, this is an important distinction. Of course, light can be thermal by black-body radiation, but this is not the same as being in contact with a thermal bath.

B.1 Floquet Theory

As an alternative, we propose using the Floquet formalism. Floquet theory describes periodic driven systems [57, 60]. These systems have a Hamiltonian that is periodic in time with some periodicity T. This Hamiltonian still satisfies the Schrödinger equation:

$$i\hbar\frac{d}{d\mathsf{t}}|\psi(\mathsf{t})\rangle = H(\mathsf{t})|\psi(\mathsf{t})\rangle \quad \text{with} \quad H(\mathsf{t}+T) = H(\mathsf{t}). \tag{B.1}$$

The idea would be that, instead of being periodic in imaginary time, the system would be periodic in real time. The frequency of the drive would then play a similar role as the temperature. Similarly to the solutions to periodic potentials in a crystal, Bloch waves, a periodic potential in time also yields periodic solutions. Except that, instead of being periodic in (quasi-)momentum, these solutions are periodic in quasi-energy. According to Floquet's theorem, the Floquet states satisfy [57]

$$|\psi_n(\mathsf{t}+T)\rangle = e^{-i\epsilon_n T/\hbar}|\psi_n(\mathsf{t})\rangle.$$

Similar to Bloch's theorem, these wavefunctions can also be decomposed into plane waves and a periodic function

$$|\psi_n(\mathsf{t})\rangle = e^{-i\epsilon_n \mathsf{t}/\hbar}|\Phi_n(\mathsf{t})\rangle \quad \text{with} \quad |\Phi_n(\mathsf{t}+T)\rangle = |\Phi_n(\mathsf{t})\rangle. \tag{B.2}$$

The periodic function $|\Phi_n(\mathsf{t})\rangle$ can then also be expanded in terms of Fourier modes (with $\Omega = 2\pi/T$)

$$|\Phi_n(\mathsf{t})\rangle = \sum_m e^{-im\Omega\mathsf{t}}\left|\phi_n^{(m)}\right\rangle. \tag{B.3}$$

Importantly, these Fourier modes $\left|\phi_n^{(m)}\right\rangle$ are not orthogonal and normalized. Inserting Eq. (B.2) into Eq. (B.1) yields

$$\left(\epsilon_n + i\hbar\frac{d}{d\mathsf{t}}\right)|\Phi_n(\mathsf{t})\rangle = H(\mathsf{t})|\Phi_n(\mathsf{t})\rangle,$$

and then applying Eq. (B.3)

$$\left(\epsilon_n + m\hbar\Omega\right)\left|\phi_n^{(m)}\right\rangle = \sum_{m'} H^{(m-m')}\left|\phi_n^{(m')}\right\rangle. \tag{B.4}$$

Here we use the fact that the Hamiltonian can also be expanded in terms of its Fourier coefficients $H(\mathfrak{t}) = \sum_m e^{-im\Omega\mathfrak{t}}H^{(m)}$. This equation allows us to solve for the Floquet modes of the system. Going one step further, we can combine all the Floquet modes in one vector and transform Eq. (B.4) into an eigenvalue problem [57]

$$\mathcal{H}\boldsymbol{\varphi}_n = \epsilon_n \boldsymbol{\varphi}_n, \quad \mathcal{H} = \begin{pmatrix} \ddots & & H^{(-1)} & & H^{(-2)} & \\ H^{(1)} & H_0 - m\hbar\Omega & & H^{(-1)} & & H^{(-2)} \\ H^{(2)} & & H^{(1)} & H_0 - (m+1)\hbar\Omega & & H^{(-1)} \\ & & H^{(2)} & & H^{(1)} & \ddots \end{pmatrix}, \quad \boldsymbol{\varphi}_n = \begin{pmatrix} \vdots \\ \left|\phi_n^{(m)}\right\rangle \\ \left|\phi_n^{(m+1)}\right\rangle \\ \vdots \end{pmatrix}. \tag{B.5}$$

This allows us to solve for the energy of Floquet modes of the system. The different entries of Eq. (B.5) are matrices as well, with sizes depending on the system size. Also note that this matrix extends indefinitly in both directions. As a consequence of this, our quasi-energy space also extends infinitly in both directions. This can be seen in Fig. B.1. However, this poses a problem, as one cannot (always) calculate the solutions to the infitinite eigenvalue problem. Therefore, the Floquet Hamiltonian has to be truncated. For this, we consider the Floquet theory for a harmonically driven system. Therefore, all terms in Eq. (B.5) with $H^{(2)}$ or higher drop out. This leaves a tridiagonal matrix, which is reminiscent of a tight-binding Hamiltonian. Here, the diagonal can be considered as on-site terms, while the off-diagonals correspond to hopping terms, in this case nearest-neighbour hopping only. For a Hamiltonian with the form $H = H_0 + Ve^{i\omega\mathfrak{t}} + V^\dagger e^{-i\omega\mathfrak{t}}$, this yields

$$\mathcal{H} = \begin{pmatrix} \ddots & & V & & 0 \\ V^\dagger & H_0 - m\omega\hbar & & V \\ 0 & & V^\dagger & & \ddots \end{pmatrix}.$$

This equation makes it relatively straightforward to determine a suitable cut-off point for the Floquet Hamiltonian [57]. In this case, either the time-independent Hamiltonian is the dominant factor or the magnitude of the hopping between them, as can be seen in Fig. B.1. The maximum of the norm of both these quantities is the relevant variable to consider. It is given by $\mathcal{W} = \max(||V||, ||H_0||)$. This can be compared to the energy of the drive, given by $\hbar\omega$. As can be seen in Fig. B.1, we should have enough terms in our Floquet Hamiltonian, such that we do not omit any terms which fall into the reachable bandwidth. This yields the result that the size of the Floquet Hamiltonian should be larger than $\mathcal{W}/\hbar\omega$.

B.1.1 Green's Function

To calculate the Floquet Green's function requires a few extra steps over the standard case, due to the periodicity in quasi-energy. Transforming the Green's function of Eq. (6.1) to Floquet space yields

$$\widetilde{G}_{n,m}(\omega) = \left(\frac{1}{-\hbar\omega - \mu + \mathcal{H}}\right)_{(n,m)},$$

where $\mathcal{H}$ is the Floquet Hamiltonian and the indices (n, m) are square matrices with the size of the amount of sites in the unit cell, ω is the frequency, and μ the chemical potential. To transform this equation from the frequency to the time domain requires a special Fourier transform [61],

$$G(\mathfrak{t}_1, \mathfrak{t}_2) = \sum_{n,m} \int_{-\Omega/2}^{\Omega/2} d\omega \widetilde{G}_{n,m}(\omega) e^{-i(\omega+n\Omega)\mathfrak{t}_1 + i(\omega+m\Omega)\mathfrak{t}_2}.$$
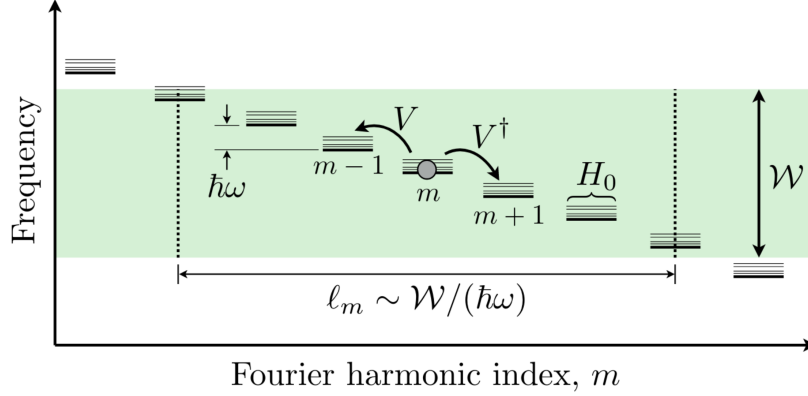
Figure B.1: Quasi-energy of a harmonically driven Floquet system. It is reminiscent of a tight-binding model, with hopping between the Floquet bands. Figure taken from Ref. [57].

B.2   Periodic Gain and Loss

We will now consider the case of a tight-binding model with periodic gain and loss. For this, we consider an SSH model, where the gain and loss alternate.

$$H = -\sum_{n=1}^{N} \left[\left(t_1 a_n^\dagger b_n + t_2 b_n^\dagger a_{n+1} + H.c. \right) + i\alpha \cos(\omega \mathsf{t}) a_n^\dagger a_n - i\alpha \cos(\omega \mathsf{t}) b_n^\dagger b_n \right], \tag{B.6}$$

where N is the number of unit cells, and t_1, t_2 denote, respectively, the inter- and the intra-cell hopping parameter. For simplicity, we assume that they are real. The operators a_n ($a_n^\dagger$) annihilate (create) a particle in sublattice A at the site n (similarly for B). α is the strength of the gain and loss, and ω the frequency of their oscillation. As a consequence, the gain and loss will swap places depending on the time. This gives

$$H_0 = \begin{pmatrix} 0 & -t_1 - t_2 e^{ika} \\ -t_1 - t_2 e^{-ika} & 0 \end{pmatrix} \quad \text{and} \quad V = V^\dagger = \begin{pmatrix} -2i\alpha & 0 \\ 0 & 2i\alpha \end{pmatrix}.$$

The cutoff for the Floquet Hamiltonian is therefore $\mathcal{W} = \max(|t_1 + t_2|, |2\alpha|)/\omega$. Figs. B.2 to B.4 show the spectra for this system, for different driving frequencies. For these, the condition of $M = 2\max(|t_1 + t_2|, |2\alpha|)/\omega$ was met, where M is the size of the Floquet Hamiltonian. These show that the driving frequency ω has a large effect on the spectrum of the system. Generalizing Eq. (B.6) gives

$$H = -\sum_{n=1}^{N} \left[\left(t_1 a_n^\dagger b_n + t_2 b_n^\dagger a_{n+1} + H.c. \right) + i\alpha_l(\mathsf{t}) a_n^\dagger a_n - i\alpha_g(\mathsf{t}) b_n^\dagger b_n \right].$$

This allows for different definitions of the loss, $\alpha_l(t)$, and gain, $\alpha_g(t)$. A different definition of the gain and loss would be to add a constant shift, such that the gain and loss do not swap places depending on time, i.e.

$$\alpha_l(\mathsf{t}) = \alpha_g(\mathsf{t}) = \alpha_0(\cos(\omega \mathsf{t}) + 1). \tag{B.7}$$

This gives

$$H_0 = \begin{pmatrix} -\alpha_0 & -t_1 - t_2 e^{ika} \\ -t_1 - t_2 e^{-ika} & \alpha_0 \end{pmatrix} \quad \text{and} \quad V = V^\dagger = \begin{pmatrix} -2i\alpha & 0 \\ 0 & 2i\alpha \end{pmatrix},$$

and the result of this Floquet system are given in Figs. B.5 to B.7. Furthermore, a system with only loss is defined as

$$\alpha_l(\mathsf{t}) = \alpha_0(\cos(\omega \mathsf{t}) + 1) \quad \text{and} \quad \alpha_g(\mathsf{t}) = 0, \tag{B.8}$$

and the results for this loss distribution are given by Figs. B.8 to B.10.
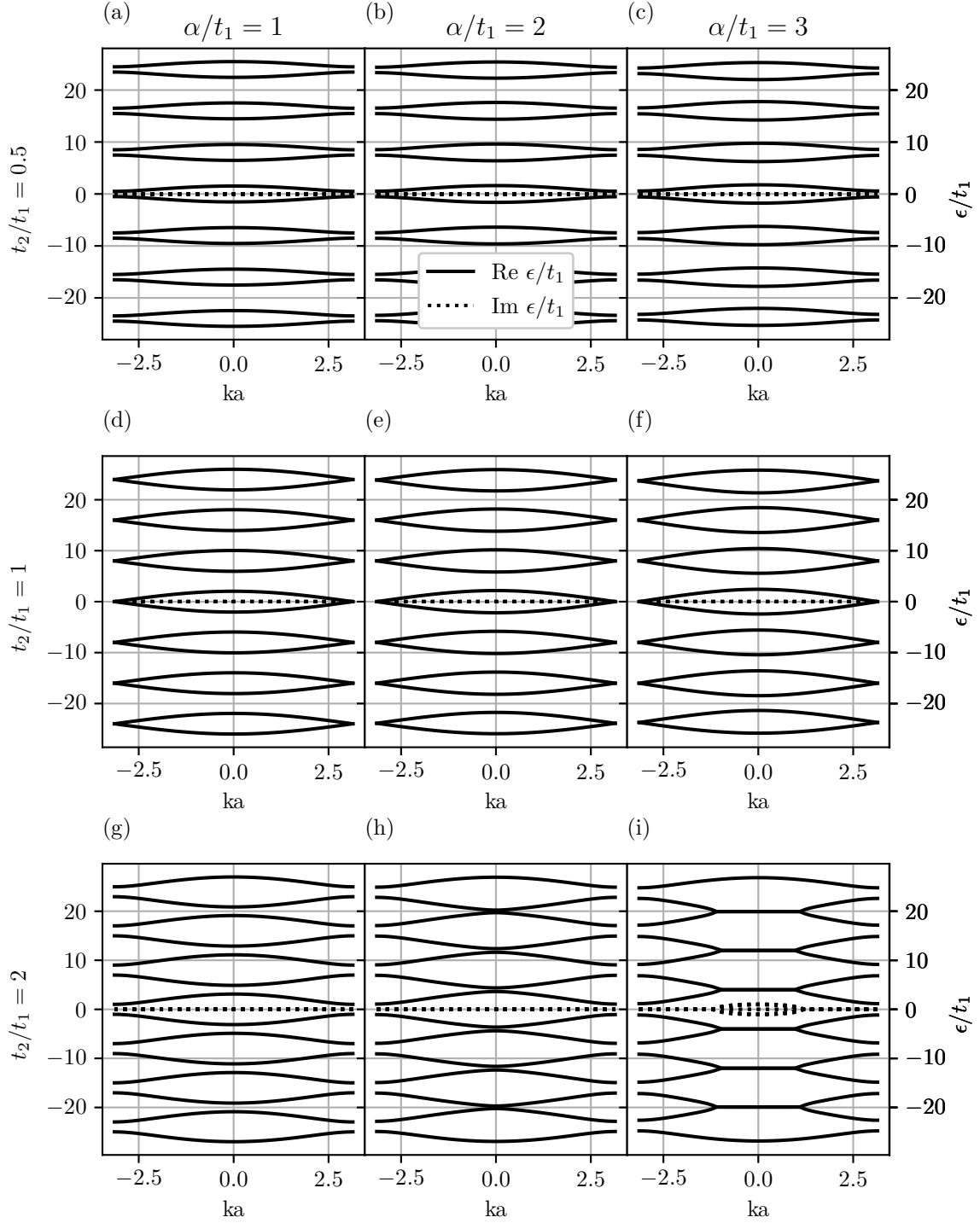
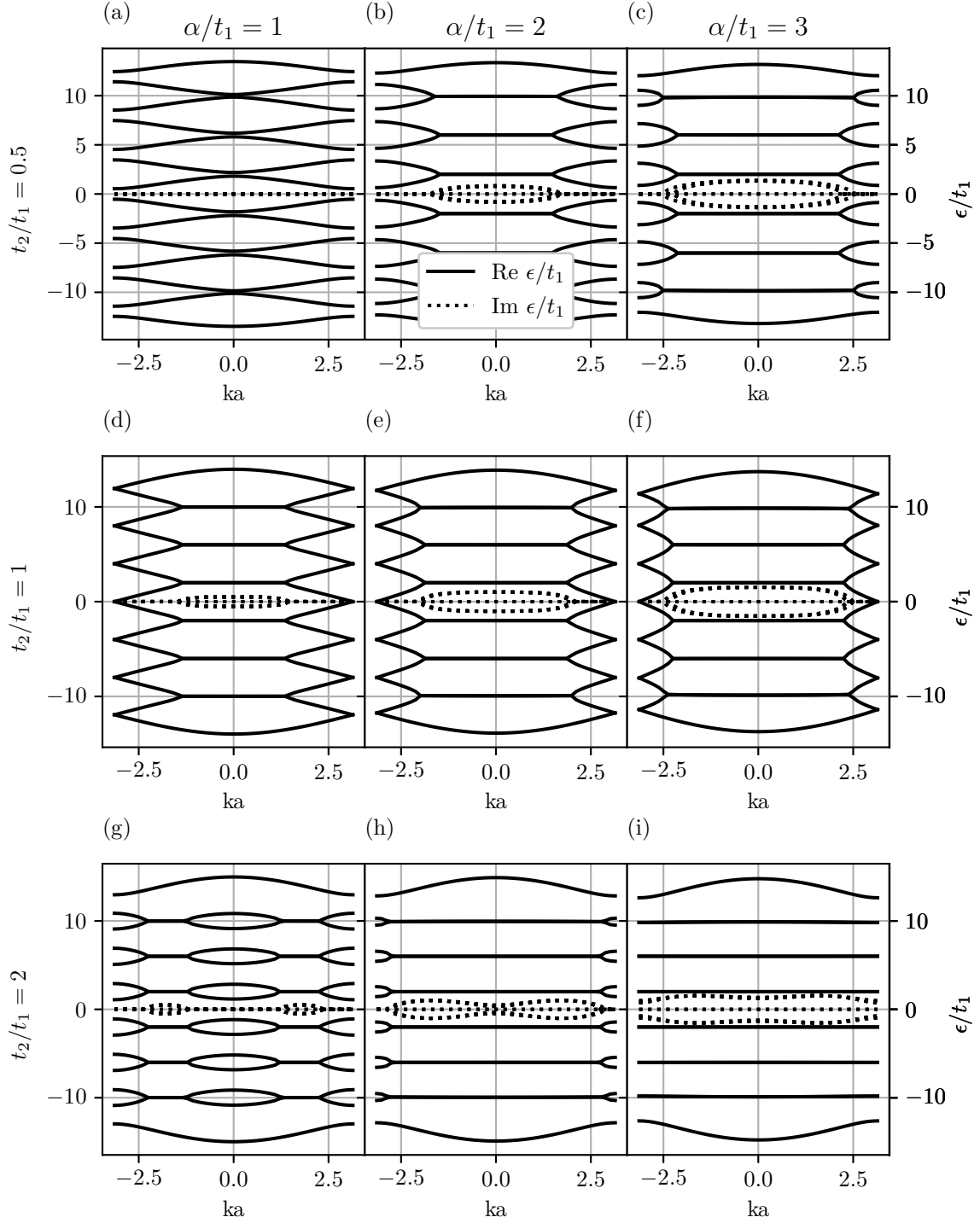Figure B.2: Spectrum for different values of α/t_1 and t_2/t_1 for the gain and loss as defined in Eq. (B.6), and for $\hbar\omega = 8$.

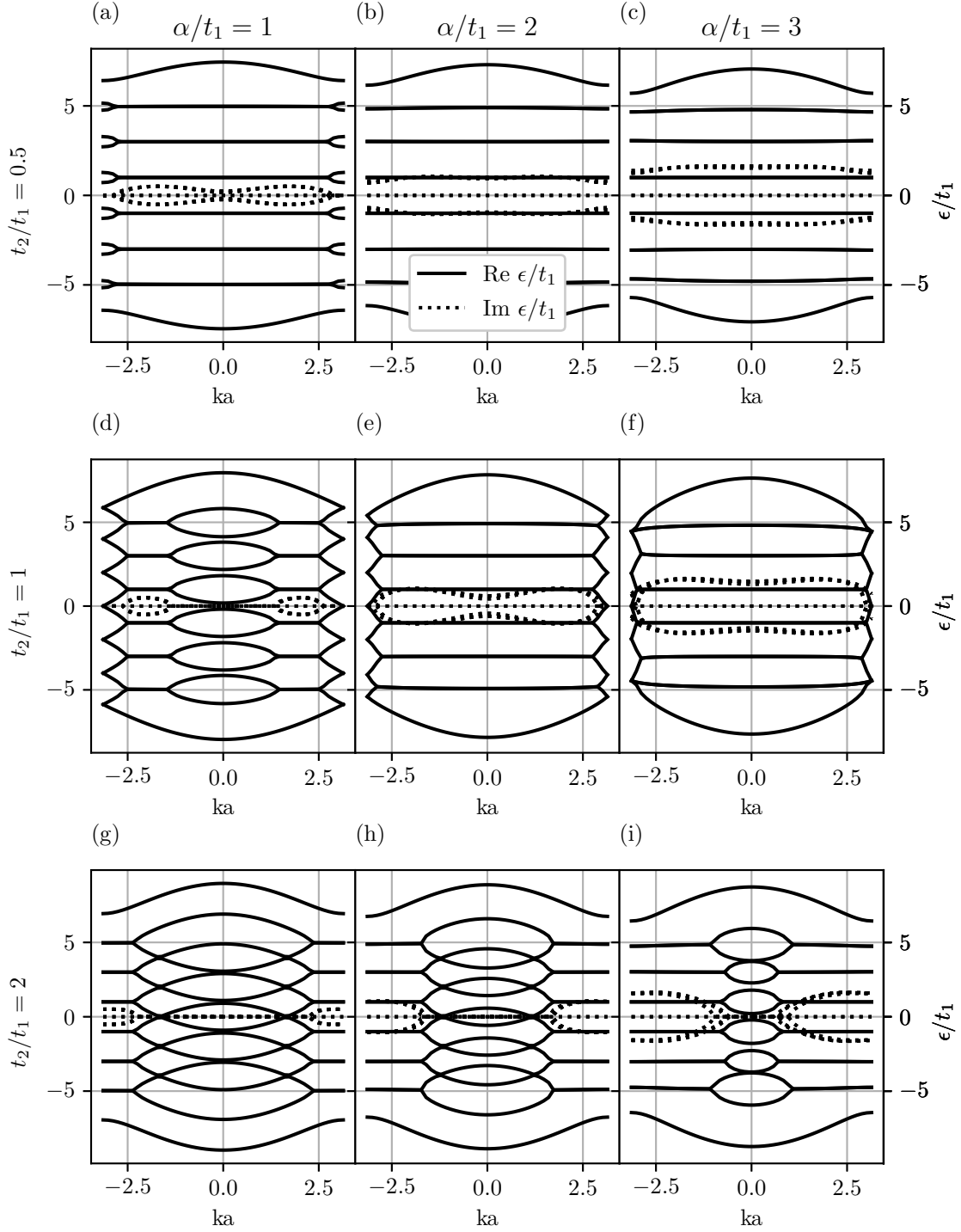*Figure B.3: Spectrum for different values of α/t_1 and t_2/t_1 for the gain and loss as defined in Eq. (B.6), and for $\hbar\omega = 4$.*

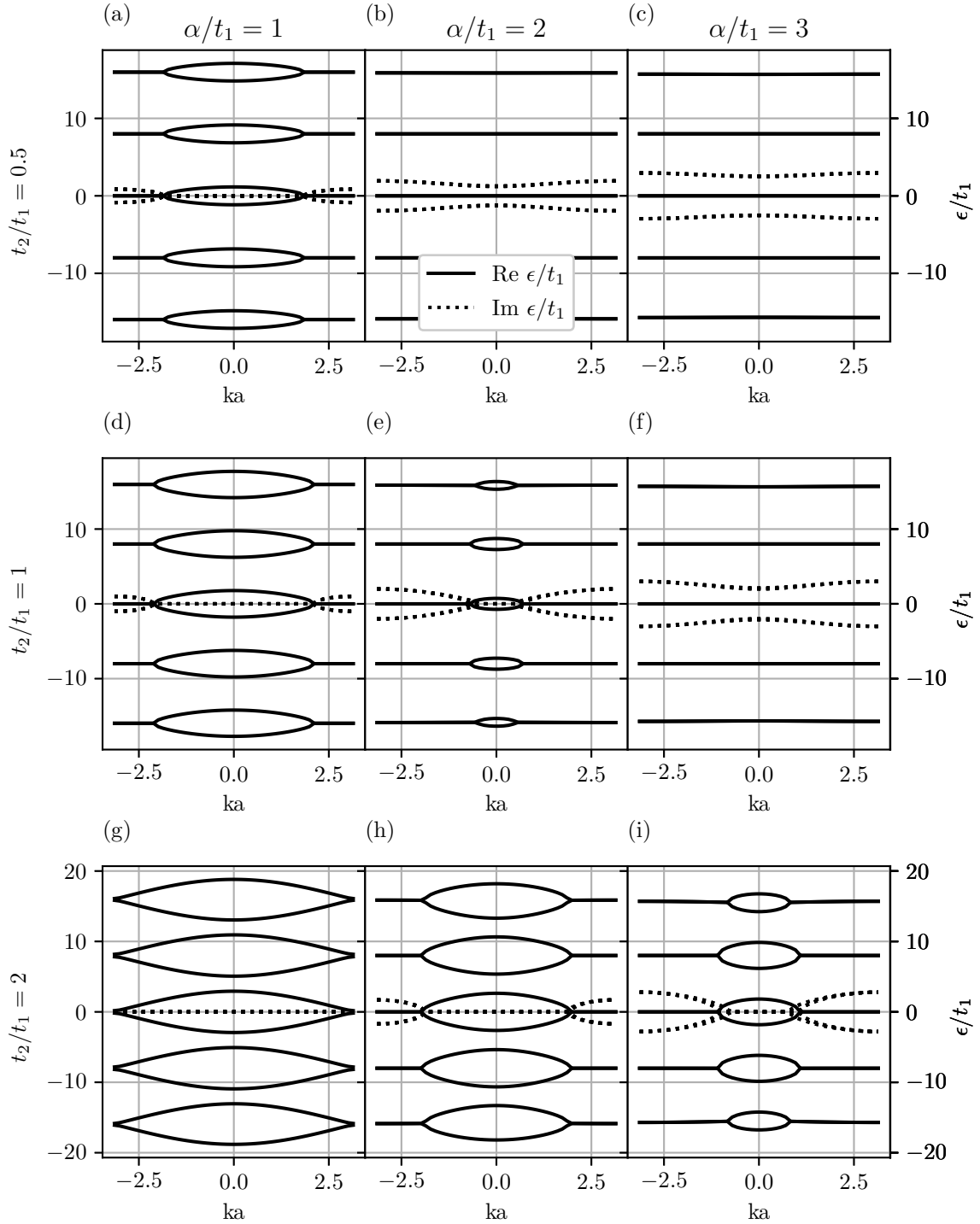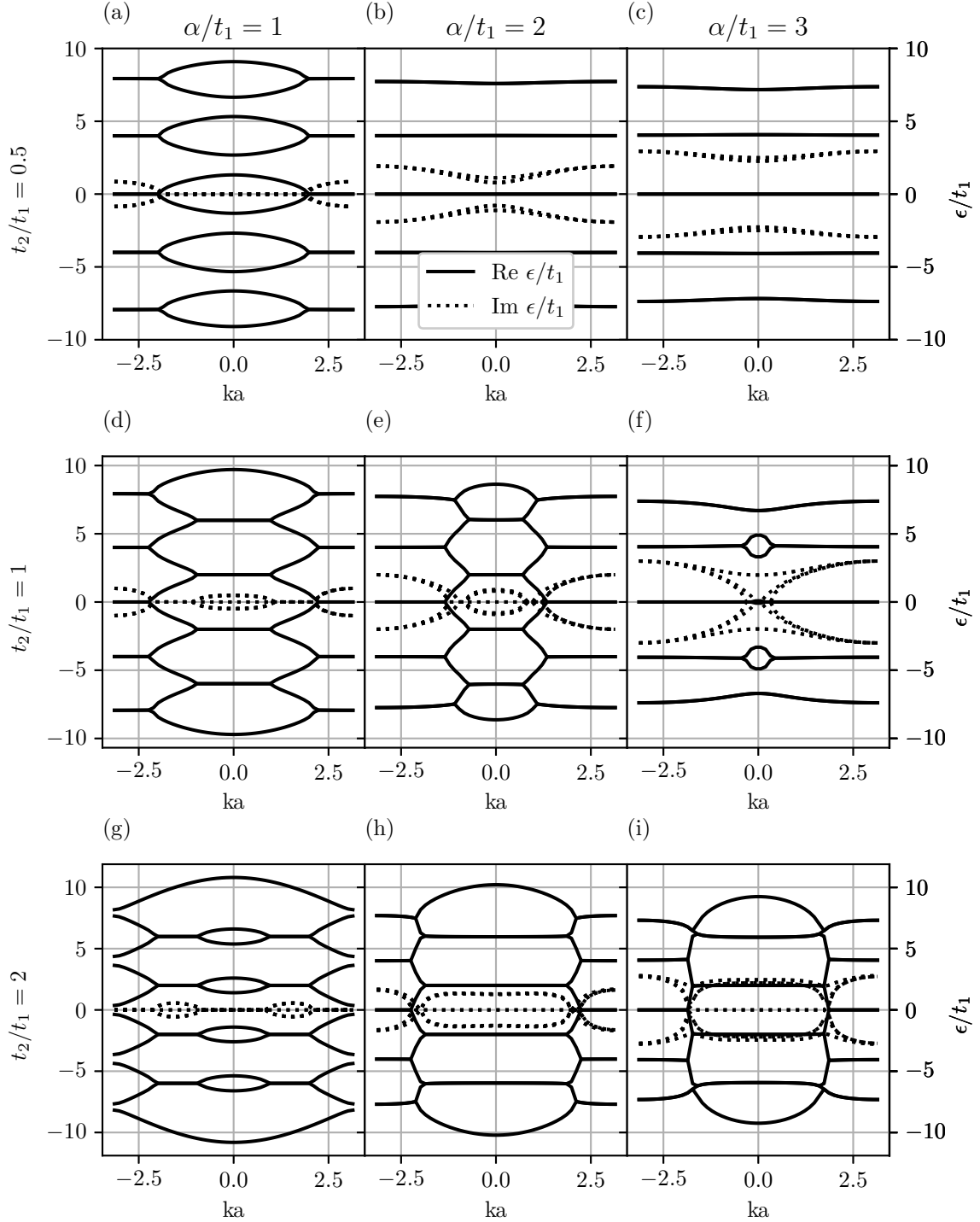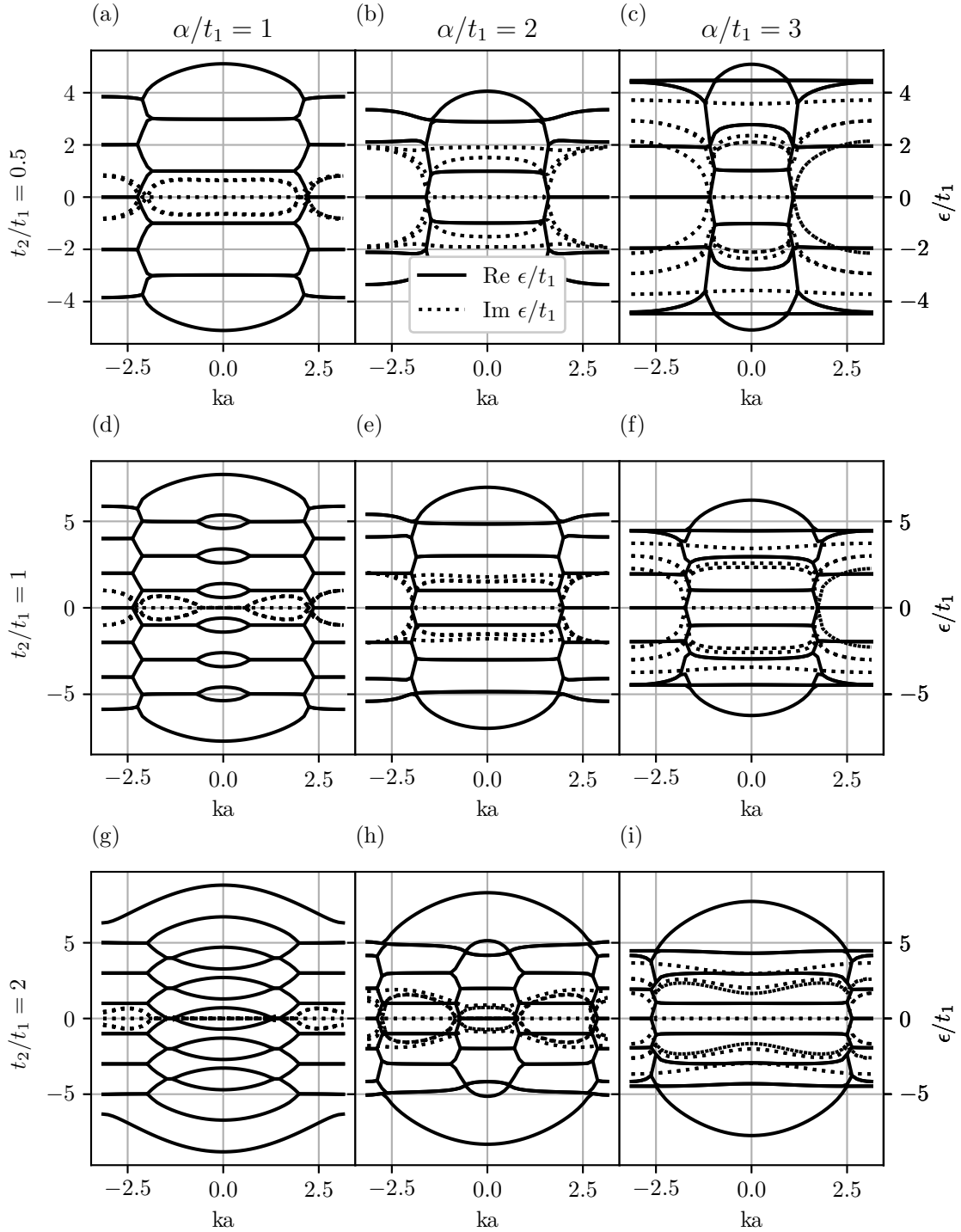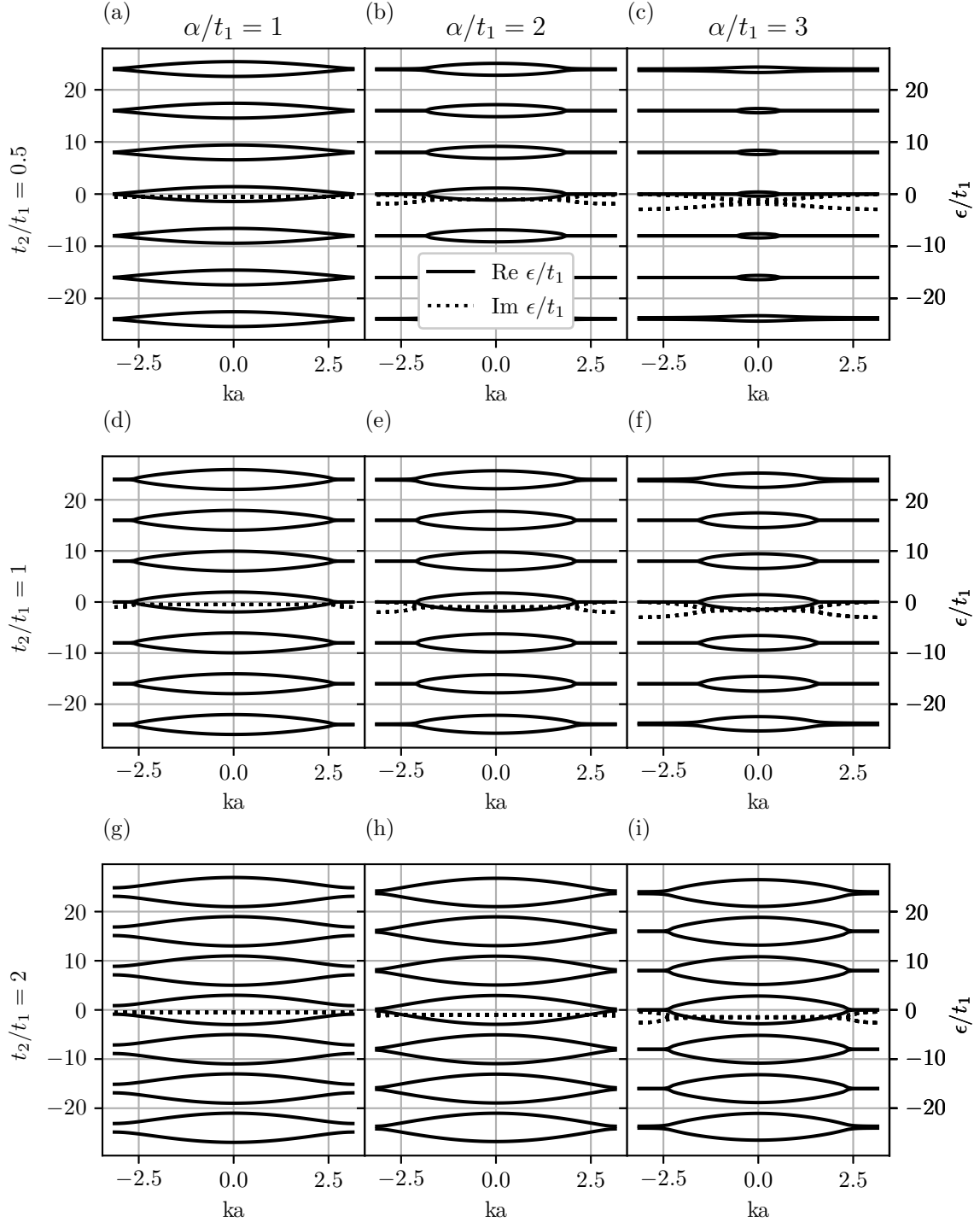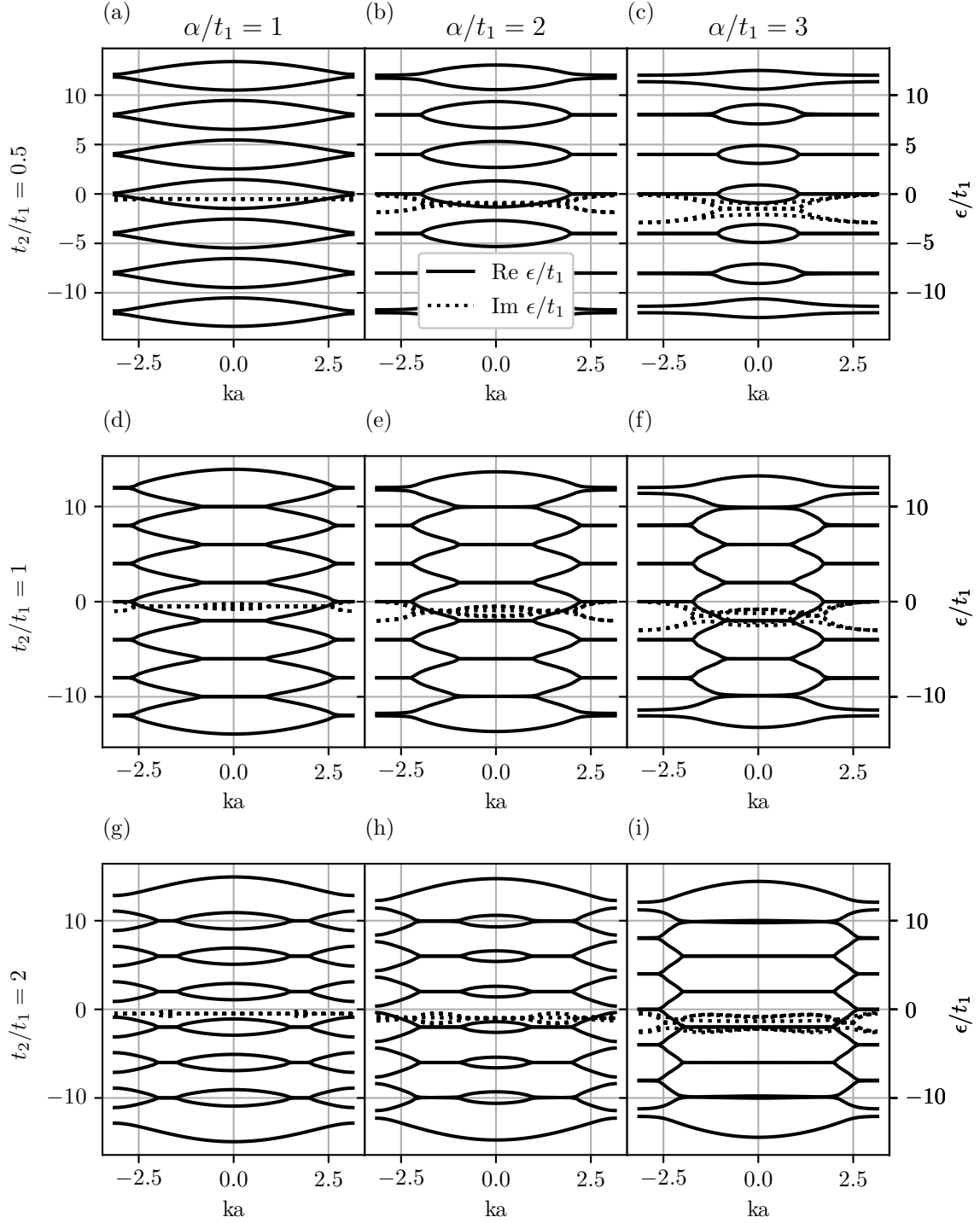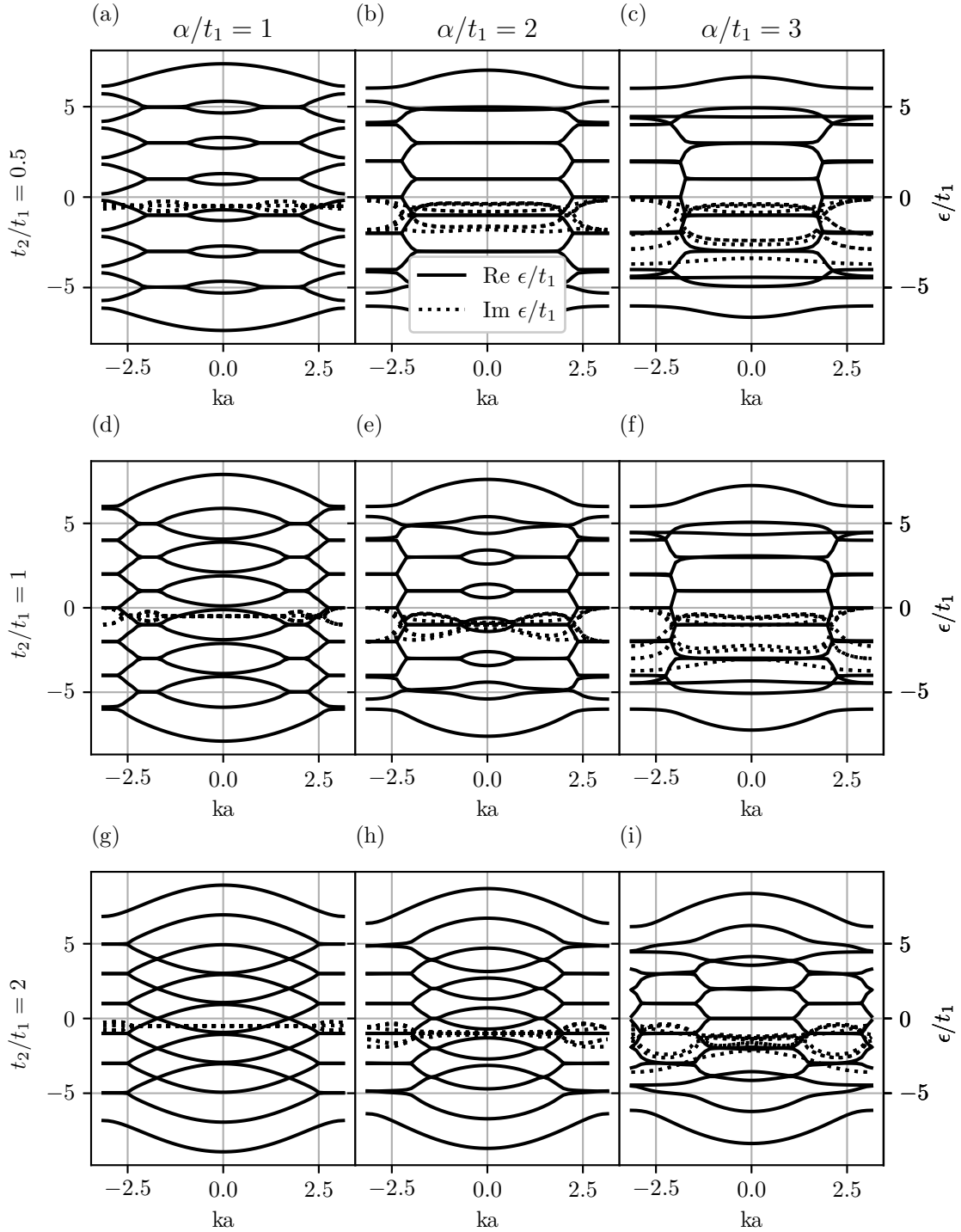*Figure B.4: Spectrum for different values of α/t_1 and t_2/t_1 for the gain and loss as defined in Eq. (B.6), and for $\hbar\omega = 2$.*

Figure B.5: Spectrum for different values of α/t_1 and t_2/t_1 for the gain and loss as defined in Eq. (B.7), and for $\hbar\omega = 8$.

Figure B.6: Spectrum for different values of α/t_1 and t_2/t_1 for the gain and loss as defined in Eq. (B.7), and for $\hbar\omega = 4$.

Figure B.7: Spectrum for different values of α/t_1 and t_2/t_1 for the gain and loss as defined in Eq. (B.7), and for $\hbar\omega = 2$.

Figure B.8: Spectrum for different values of α/t_1 and t_2/t_1 for the gain and loss as defined in Eq. (B.8), and for $h\omega = 8$.

Figure B.9: *Spectrum for different values of α/t_1 and t_2/t_1 for the gain and loss as defined in Eq.* (B.8), *and for $\hbar\omega = 4$.*

Figure B.10: Spectrum for different values of α/t_1 and t_2/t_1 for the gain and loss as defined in Eq. (B.8), and for $\hbar\omega = 2$.

Appendix C

Green's Functions

In Chapter 6, we gave a limited amount of examples for the Green's functions of the different variations on the gain and loss tight-binding models. Here we present all the Green's functions for these models, which were calculated in this thesis.

Alternating Loss
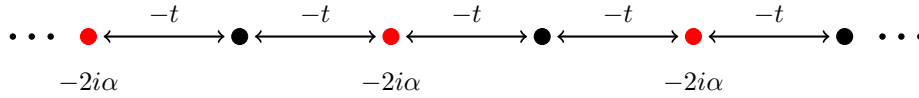
Figure C.1: Schematic overview of a tight-binding chain with alternating loss, as given by the Hamiltonian of Eq. (3.7).

Fig. C.2 shows the Green's functions for the tight-binding system with alternating loss, as depicted in Fig. C.1. As discussed in the main text, Fig. C.2a shows that the pole structure has shifted entirely to the negative Matsubara domain. As a consequence of this, the dominant Matsubara mode in the $G_{2,2}$ term is now at the 0th Matsubara mode (see Fig. C.2a(ii)), which does not yield an imaginary time dependence (Fig. C.2b(ii)).

SSH with Gain and Loss
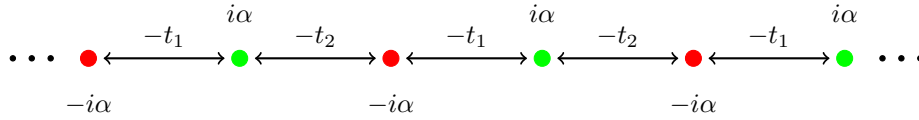
Figure C.3: Schematic overview of the SSH chain with alternating gain and loss.

In Fig. C.4 the Green's functions for the topological ($t_2/t_1 = 2$) SSH with alternating gain and loss, as given by Fig. C.3, are given. Similarly, Fig. C.5 gives the trivial regime. The topological and trivial figures are both for different values of α/t_1, highlighting the fact that their spectrum is different.
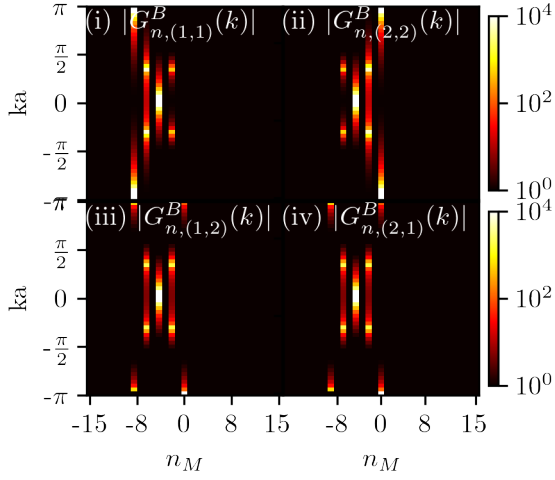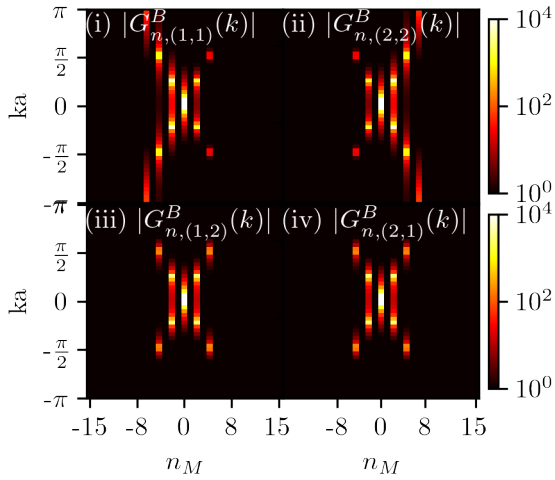
(a) Green's function in Matsubara modes and momentum space. Results are for PBC, bosonic case, $\beta = 2\pi$, $\mu = 0$, $\alpha/t = 2.001$ and for 50 unit cells (and thus also 50 k-points). The top colourbar is for (i) and (ii) and the bottom colourbar is for (iii) and (iv).
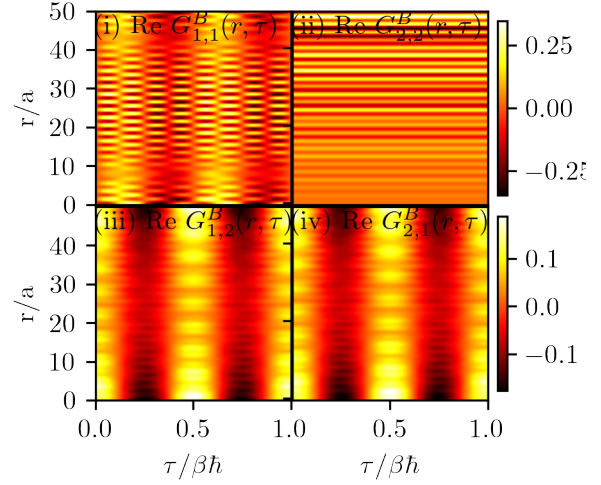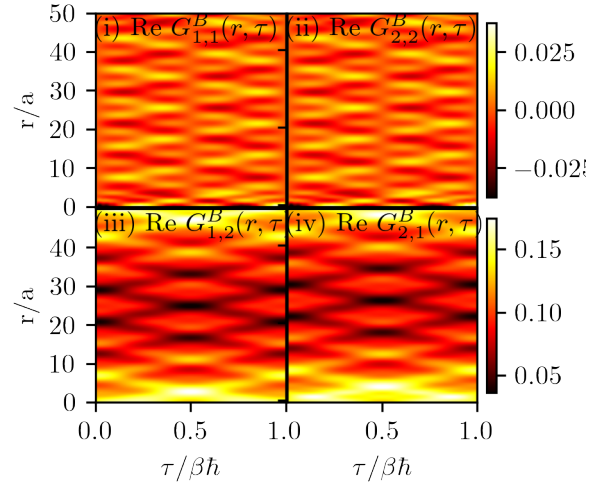
(b) Green's function in imaginary time and real space. Results are for PBC, bosonic case, $\beta = 2\pi$, $\mu = 0$, $\alpha/t = 2.001$ and for 50 unit cells (and thus also 50 k-points). Here, $G(r, \tau)$ is shown as a function of unit cells. The top colourbar is for (i) and (ii) and the bottom colourbar is for (iii) and (iv). Notice how the amplitude in (i) and (ii) is two times higher than (iii) and (iv).

Figure C.2

(a) Green's function in Matsubara modes and momentum space for the topological SSH chain $t_2/t_1 = 2$. Results are for PBC, bosonic case, $\beta = 2\pi$, $\mu = 0$, $\alpha/t_1 = 3.001$ and for 50 unit cells (and thus also 50 k-points). The top colourbar is for (i) and (ii) and the bottom colourbar is for (iii) and (iv).

(b) Green's function in imaginary time and real space for the topological SSH chain $t_2/t_1 = 2$. Results are for PBC, bosonic case, $\beta = 2\pi$, $\mu = 0$, $\alpha/t_1 = 3.001$ and for 50 unit cells (and thus also 50 k-points). Here $G(r, \tau)$ is shown as a function of unit cells. The top colourbar is for (i) and (ii) and the bottom colourbar is for (iii) and (iv). Notice how the amplitude in (i) and (ii) is two times higher than (iii) and (iv).

Figure C.4

(a) Green's function in Matsubara modes and momentum space for the trivial SSH chain $t_2/t_1 = 0.5$. Results are for PBC, bosonic case, $\beta = 2\pi$, $\mu = 0$, $\alpha/t_1 = 1.501$ and for 50 unit cells (and thus also 50 k-points). The top colourbar is for (i) and (ii) and the bottom colourbar is for (iii) and (iv).

(b) Green's function in imaginary time and real space for the trivial SSH chain $t_2/t_1 = 0.5$. Results are for PBC, bosonic case, $\beta = 2\pi$, $\mu = 0$, $\alpha/t_1 = 1.501$ and for 50 unit cells (and thus also 50 k-points). Here $G(r, \tau)$ is shown as a function of unit cells. The top colourbar is for (i) and (ii) and the bottom colourbar is for (iii) and (iv). Notice how the amplitude in (i) and (ii) is two times higher than (iii) and (iv).
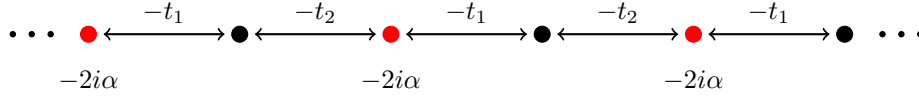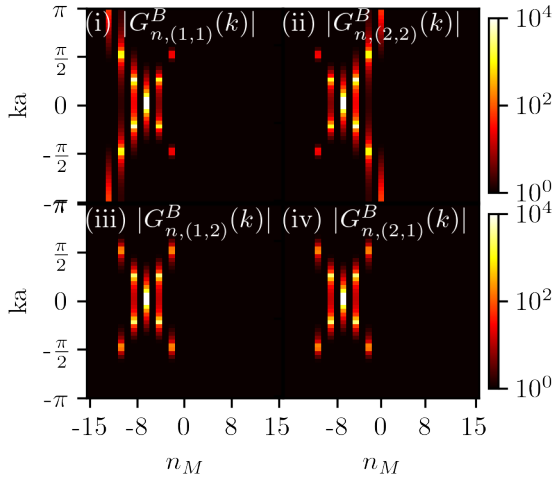
Figure C.5

SSH with Loss

*Figure C.6: Schematic overview of the SSH chain with alternating loss.*

In Fig. C.7 the Green's functions for the topological ($t_2/t_1 = 2$) SSH with alternating gain and loss, as given by Fig. C.6, are given. Similarly, Fig. C.8 gives the trivial regime. The topological and trivial figures are both for different values of α/t_1, highlighting the fact that their spectrum is different. Here, we also given the dependence of these Green's functions on α/t_1, since those were not given in the main text. These can be seen in Figs. C.9 and C.10.

Open Boundary Systems

Figs. C.11 to C.14 show the Green's functions as a function of α/t for different models with open boundary conditions, with loss and gain located near the edge. These suggest that only adding a few gain and loss sites near the edge does not influence the Green's function very much.
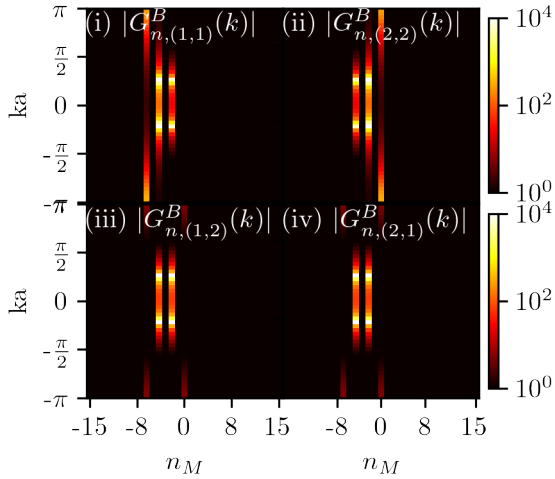
(a) Green's function in Matsubara modes and momentum space for the topological SSH chain $t_2/t_1 = 2$. Results are for PBC, bosonic case, $\beta = 2\pi$, $\mu = 0$, $\alpha/t_1 = 3.001$ and for 50 unit cells (and thus also 50 k-points). The top colourbar is for (i) and (ii) and the bottom colourbar is for (iii) and (iv).
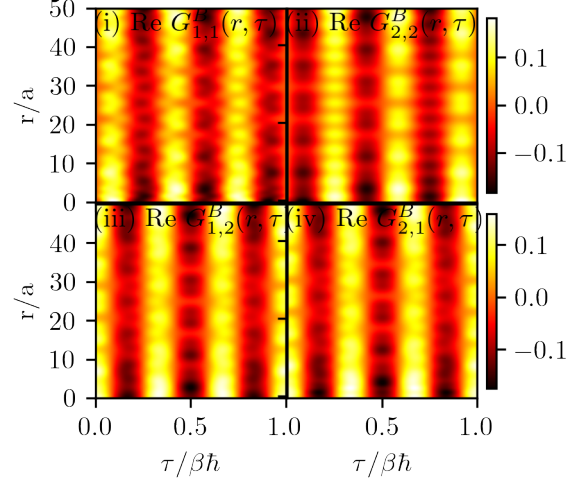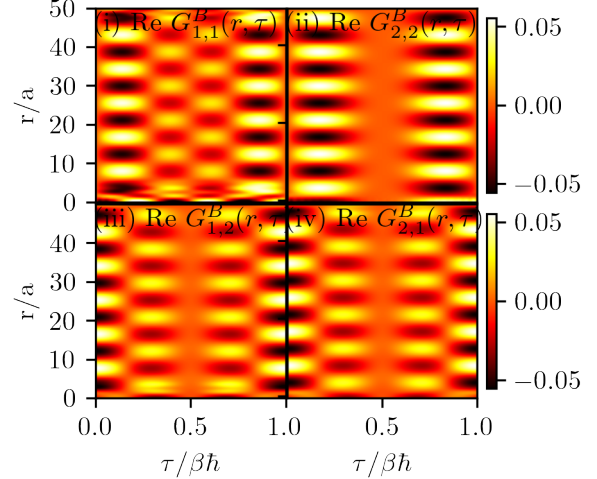
(b) Green's function in imaginary time and real space for the topological SSH chain $t_2/t_1 = 2$. Results are for PBC, bosonic case, $\beta = 2\pi$, $\mu = 0$, $\alpha/t_1 = 3.001$ and for 50 unit cells (and thus also 50 k-points). Here $G(r, \tau)$ is shown as a function of unit cells. The top colourbar is for (i) and (ii) and the bottom colourbar is for (iii) and (iv). Notice how the amplitude in (i) and (ii) is two times higher than (iii) and (iv).

Figure C.7

(a) Green's function in Matsubara modes and momentum space for the trivial SSH chain $t_2/t_1 = 0.5$. Results are for PBC, bosonic case, $\beta = 2\pi$, $\mu = 0$, $\alpha/t_1 = 1.501$ and for 50 unit cells (and thus also 50 k-points). The top colourbar is for (i) and (ii) and the bottom colourbar is for (iii) and (iv).

(b) Green's function in imaginary time and real space for the trivial SSH chain $t_2/t_1 = 0.5$. Results are for PBC, bosonic case, $\beta = 2\pi$, $\mu = 0$, $\alpha/t_1 = 1.501$ and for 50 unit cells (and thus also 50 k-points). Here $G(r, \tau)$ is shown as a function of unit cells. The top colourbar is for (i) and (ii) and the bottom colourbar is for (iii) and (iv). Notice how the amplitude in (i) and (ii) is two times higher than (iii) and (iv).
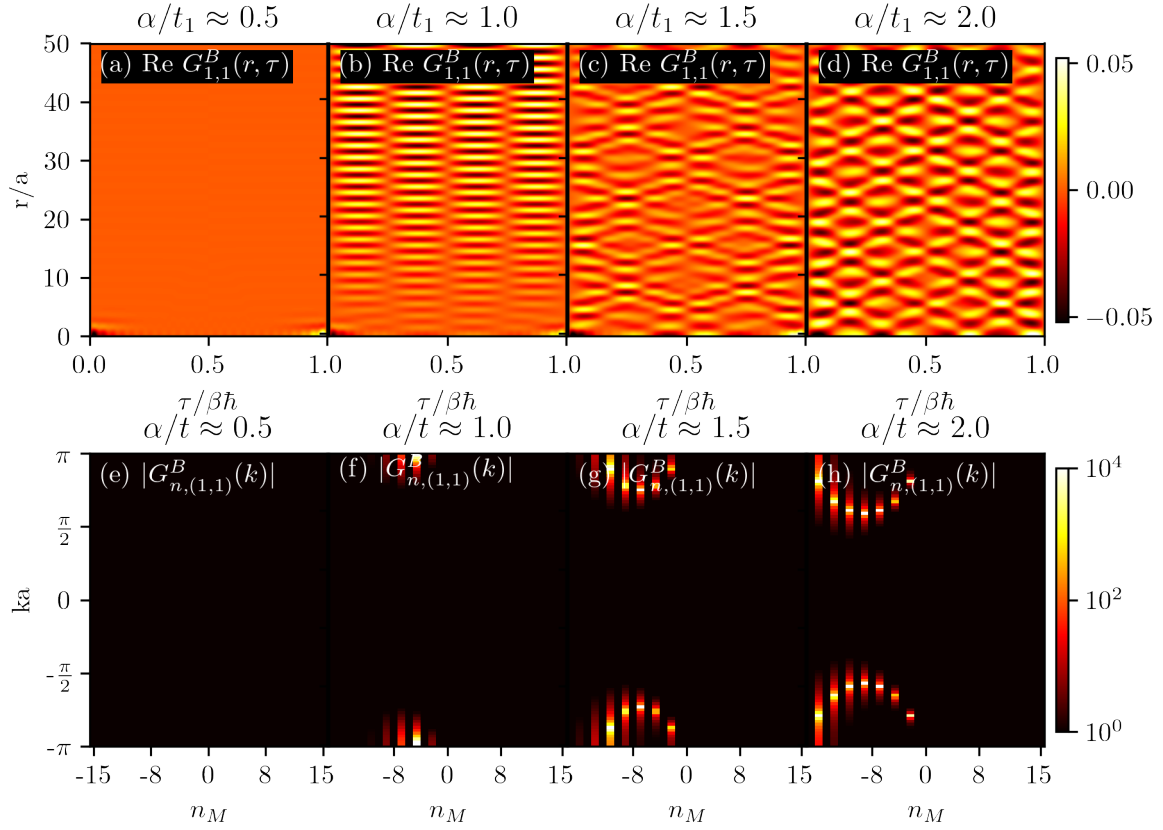
Figure C.8

Figure C.9: The $G_{1,1}^B$ Green's function for different values of α for the topological SSH model with $t_2/t_1 = 2$. Results are for PBC, bosonic case, $\beta = 4\pi$, $\mu = 0$ and for 100 lattice sites (and thus also 100 k-points). This is equivalent to 50 unit cells. We added 0.001 to every α to avoid divergences. (a)-(d) The Green's function as a function of position and imaginary time. (e)-(h) The Green's function as a function of momentum and Matsubara modes.
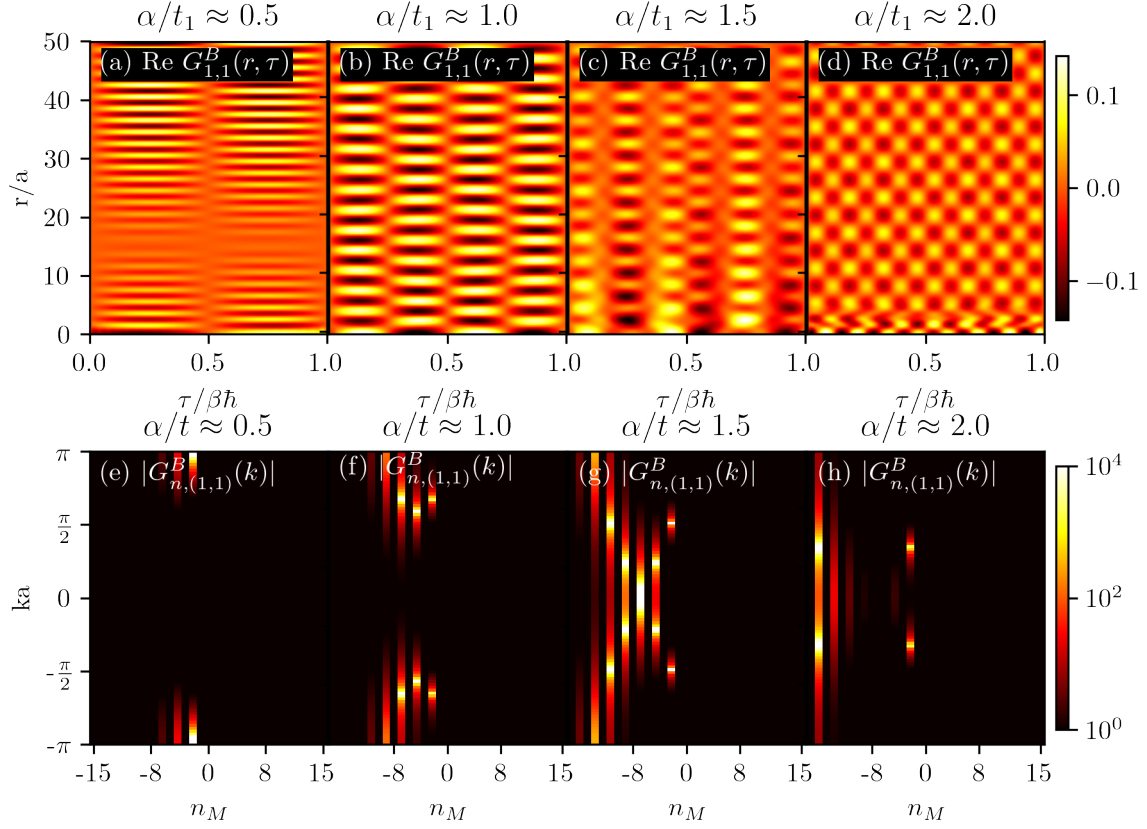
Figure C.10: The $G^B_{1,1}$ Green's function for different values of α for the trivial SSH model with $t_2/t_1 = 0.5$. Results are for PBC, bosonic case, $\beta = 4\pi$, $\mu = 0$ and for 100 lattice sites (and thus also 100 k-points). This is equivalent to 50 unit cells. We added 0.001 to every α to avoid divergences. (a)-(d) The Green's function as a function of position and imaginary time. (e)-(h) The Green's function as a function of momentum and Matsubara modes.
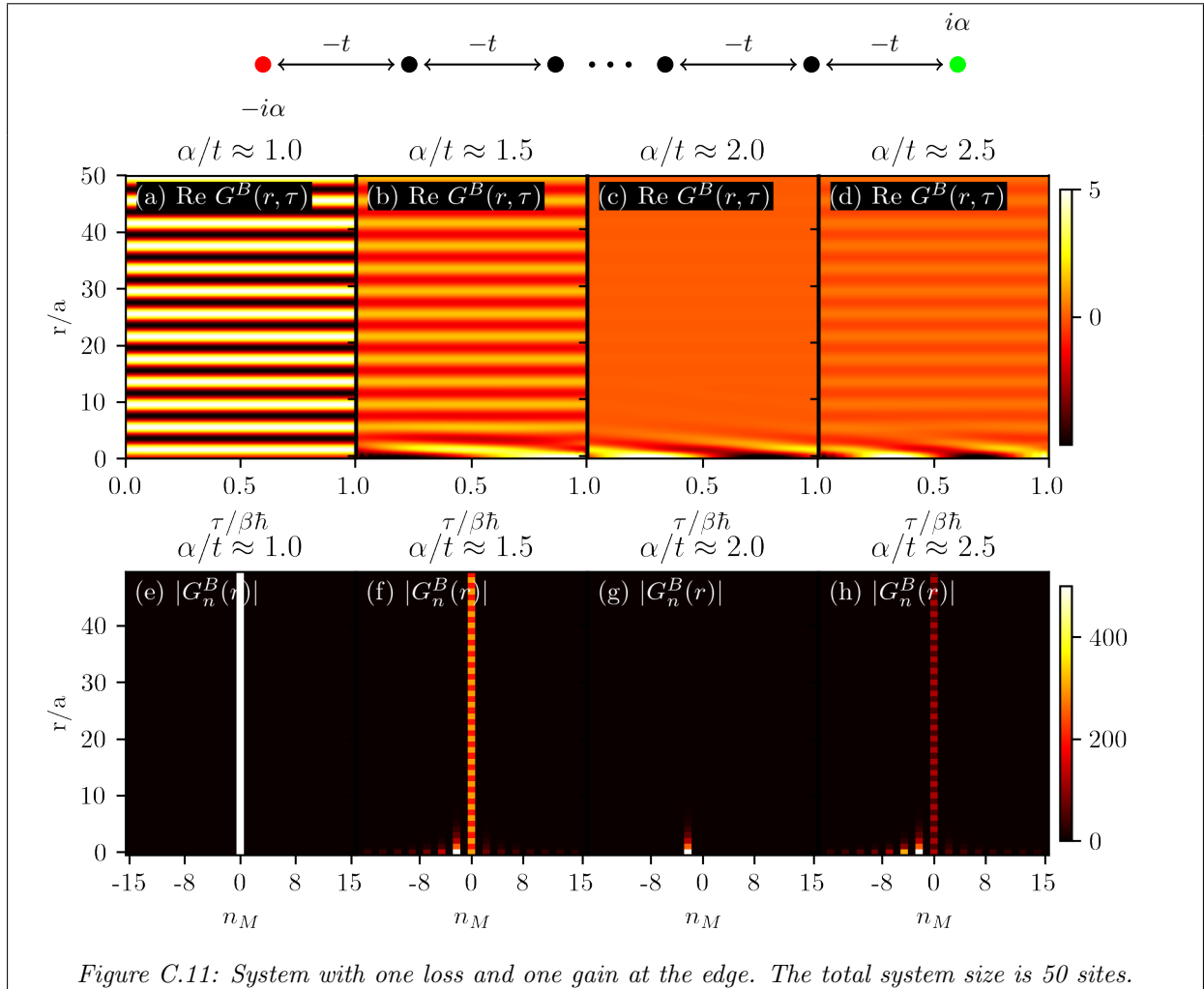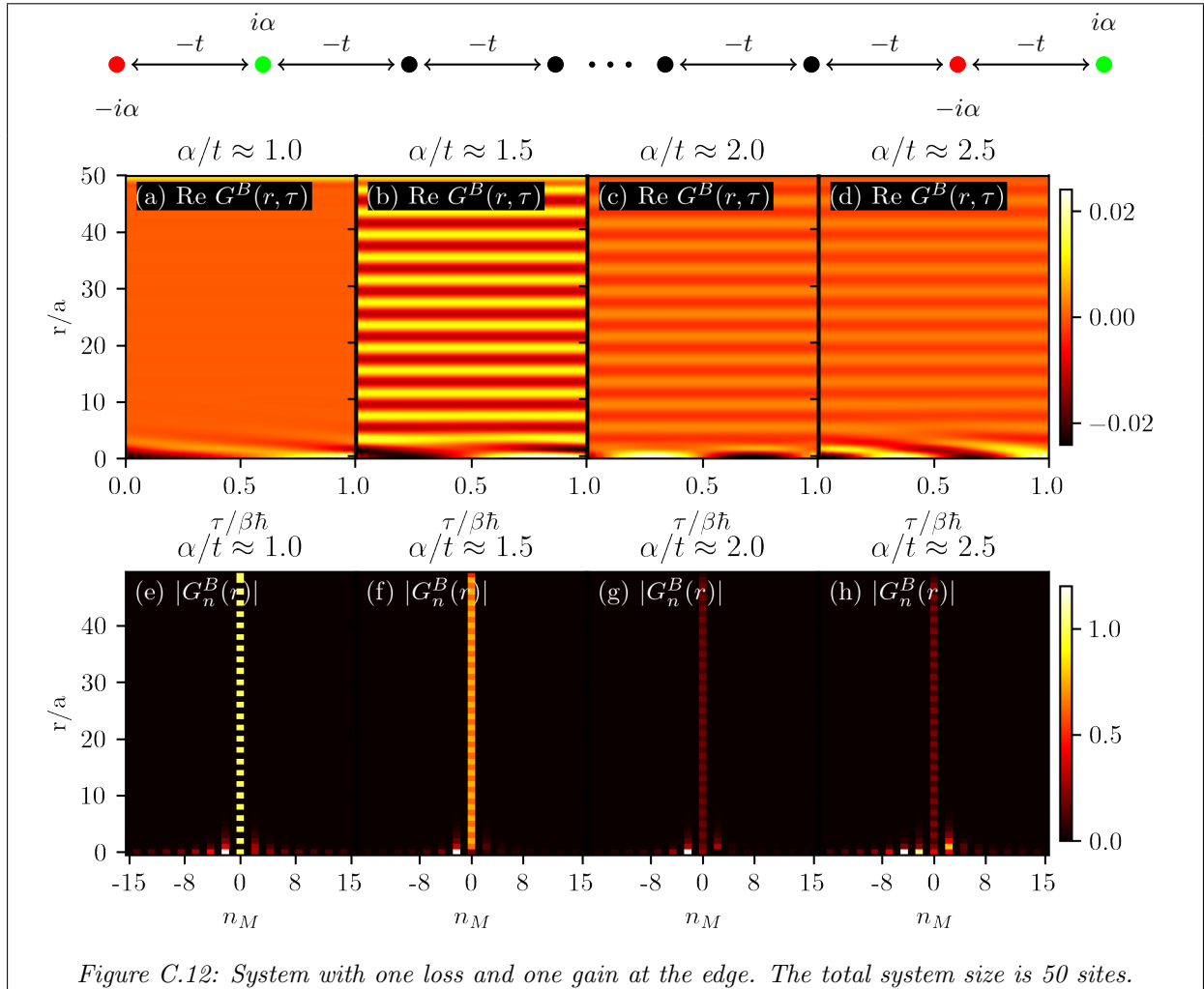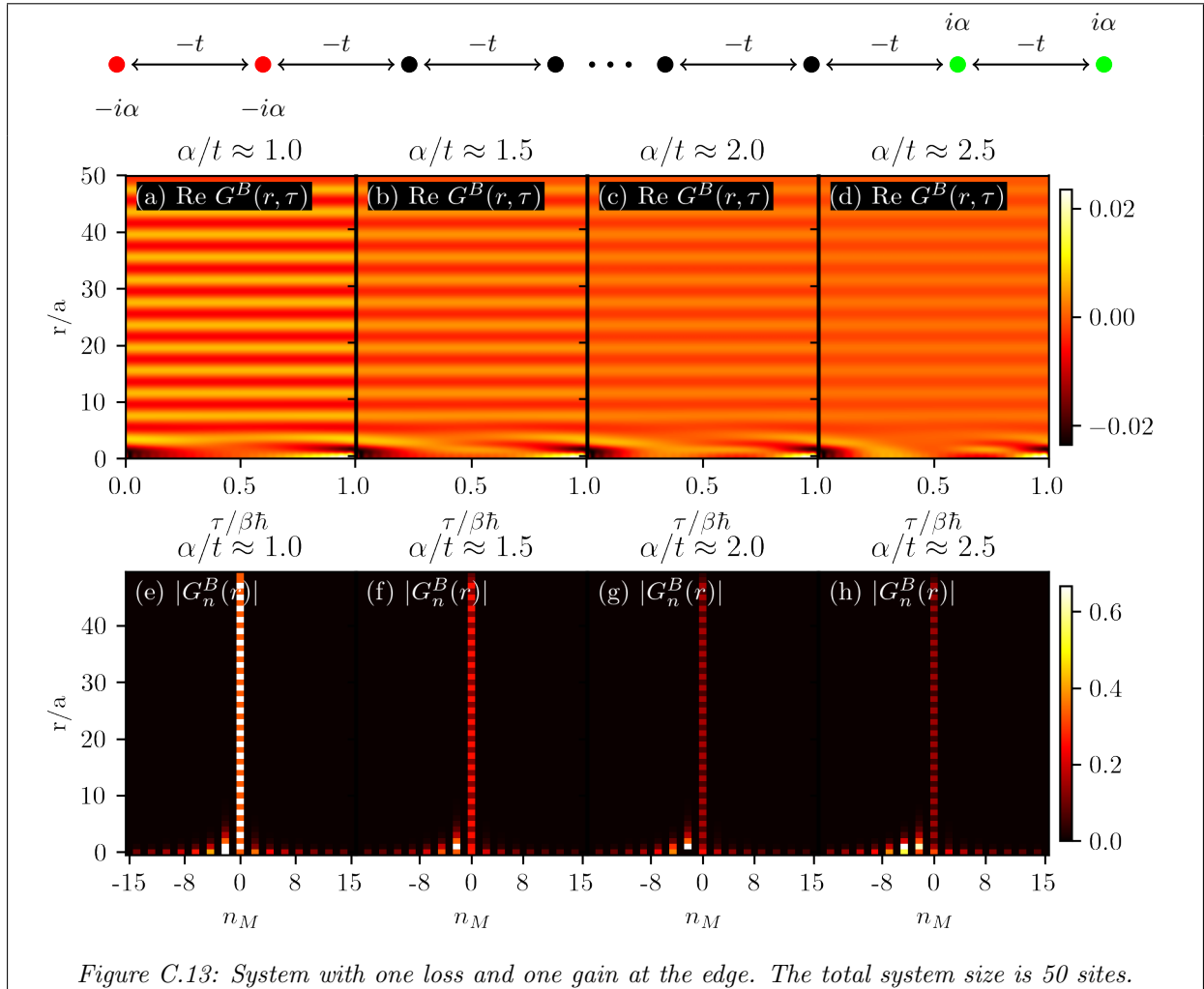
Figure C.11: *System with one loss and one gain at the edge. The total system size is 50 sites.*

Figure C.12: System with one loss and one gain at the edge. The total system size is 50 sites.

Figure C.13: *System with one loss and one gain at the edge. The total system size is 50 sites.*

Figure C.14: *System with one loss and one gain at the edge. The total system size is 50 sites.*
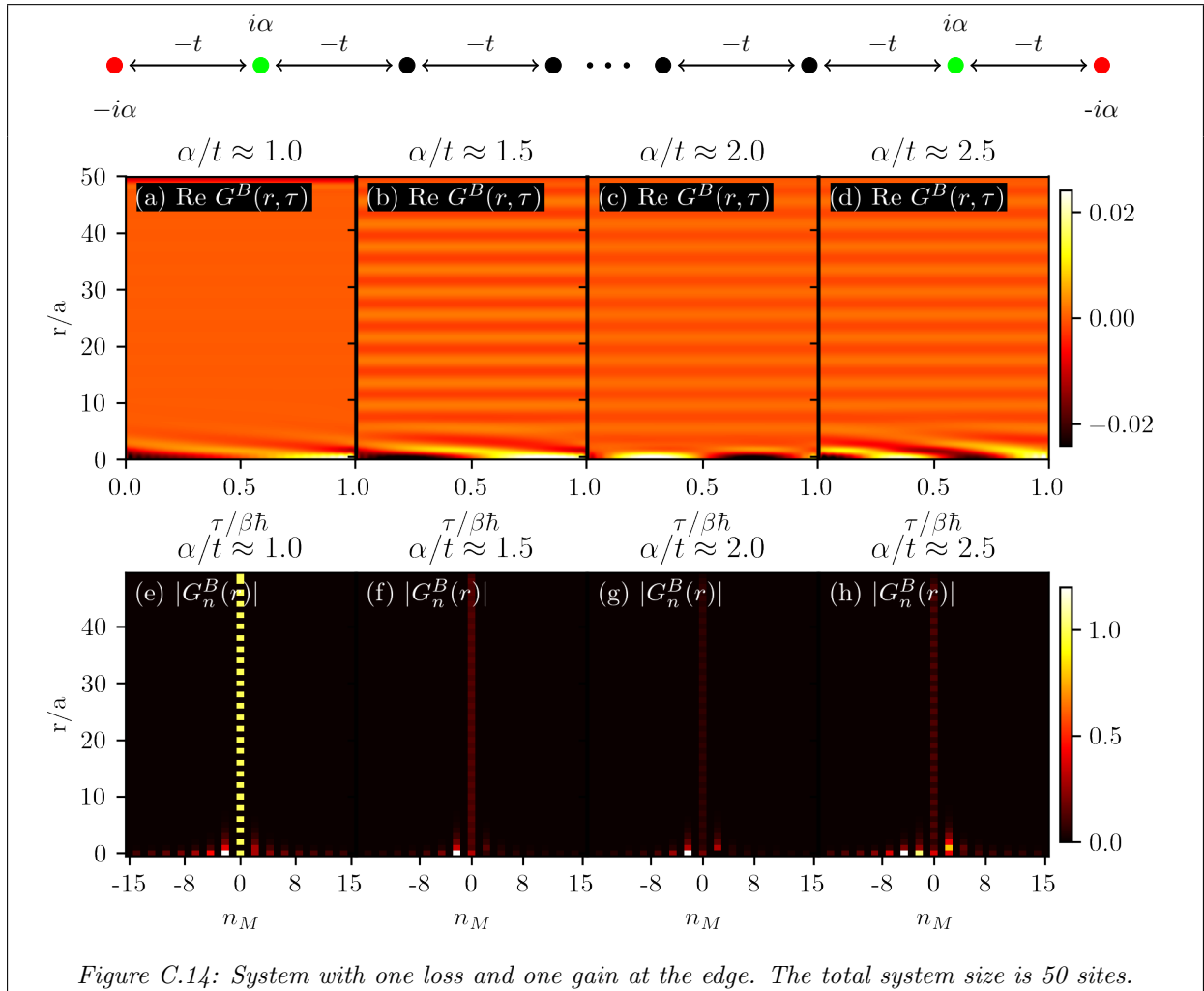
References

[1] E. Slootman, W. Cherifi, L. Eek, R. Arouca, E. J. Bergholtz, M. Bourennane, and C. Morais Smith, "Topological Monomodes in non-Hermitian Systems", Apr. 12, 2023, arXiv:2304.05748, preprint.

[2] T. Yoshida and Y. Hatsugai, "Exceptional rings protected by emergent symmetry for mechanical systems", Physical Review B **100**, 054109 (2019).

[3] J. Schindler, A. Li, M. C. Zheng, F. M. Ellis, and T. Kottos, "Experimental study of active LRC circuits with PT symmetries", Physical Review A **84**, 040101 (2011).

[4] M. Ezawa, "Non-Hermitian higher-order topological states in nonreciprocal and reciprocal systems with their electric-circuit realization", Physical Review B **99**, 201411 (2019).

[5] Y. Aurégan and V. Pagneux, "PT-Symmetric Scattering in Flow Duct Acoustics", Physical Review Letters **118**, 174301 (2017).

[6] R. Fleury, D. Sounas, and A. Alù, "An invisible acoustic sensor based on parity-time symmetry", Nature Communications **6**, 5905 (2015).

[7] A. Murugan and S. Vaikuntanathan, "Topologically protected modes in non-equilibrium stochastic systems", Nature Communications **8**, 13881 (2017).

[8] D. R. Nelson and N. M. Shnerb, "Non-Hermitian localization and population biology", Physical Review E **58**, 1383–1403 (1998).

[9] G. Kerg, K. Goyette, M. P. Touzel, G. Gidel, E. Vorontsov, Y. Bengio, and G. Lajoie, "Non-normal Recurrent Neural Network (nnRNN): learning long time dependencies while improving expressivity with transient dynamics", Oct. 28, 2019, arXiv:1905.12080, preprint.

[10] F. Wilczek, "Quantum Time Crystals", Physical Review Letters **109**, 160401 (2012).

[11] A. Shapere and F. Wilczek, "Classical Time Crystals", Physical Review Letters **109**, 160402 (2012).

[12] H. T. C. Stoof, K. B. Gubbels, and D. B. M. Dickerscheid, *Ultracold Quantum Fields* (Springer Netherlands, Dordrecht, 2008).

[13] Z. Cai, Y. Huang, and W. V. Liu, "Imaginary Time Crystal of Thermal Quantum Matter*", Chinese Physics Letters **37**, 050503 (2020).

[14] R. Arouca, E. C. Marino, and C. Morais Smith, "Non-Hermitian quantum gases: a platform for imaginary time crystals", Quantum Frontiers **1**, 1–11 (2022).

[15] W. P. Su, J. R. Schrieffer, and A. J. Heeger, "Solitons in Polyacetylene", Physical Review Letters **42**, 1698 (1979).

[16] D. J. Griffiths and D. F. Schroeter, *Introduction to quantum mechanics* (Cambridge university press, 2017).

[17] D. C. Brody, "Biorthogonal quantum mechanics", Journal of Physics A: Mathematical and Theoretical **47**, 035305 (2013).

[18] Y. Ashida, Z. Gong, and M. Ueda, "Non-Hermitian Physics", Advances in Physics **69**, 249–435 (2020).

[19] F. Roccati, G. M. Palma, F. Ciccarello, and F. Bagarello, "Non-Hermitian Physics and Master Equations", Open Systems & Information Dynamics **29**, 2250004 (2022).

[20] B. H. Bransden and C. J. Joachain, *Quantum Mechanics*, 2nd ed. (Pearson Education, 2000).

[21] E. J. Bergholtz, J. C. Budich, and F. K. Kunst, "Exceptional topology of non-Hermitian systems", Reviews of Modern Physics **93**, 015005 (2021).

[22] B. Gardas, S. Deffner, and A. Saxena, "Non-hermitian quantum thermodynamics", Scientific Reports **6**, 1–8 (2016).

[23] C. M. Bender, "Making Sense of Non-Hermitian Hamiltonians", Reports on Progress in Physics **70**, 947–1018 (2007).

[24] L. Jin and Z. Song, "Solutions of PT symmetric tight-binding chain and its equivalent Hermitian counterpart", Physical Review A **80**, 052107 (2009).

[25] H. P. Breuer and F. Petruccione, *The Theory of Open Quantum Systems* (Oxford University Press, 2007).

[26] V. Kozii and L. Fu, "Non-Hermitian Topological Theory of Finite-Lifetime Quasiparticles: Prediction of Bulk Fermi Arc Due to Exceptional Point", Aug. 19, 2017, arXiv:1708.05841, preprint.

[27] M.-A. Miri and A. Alù, "Exceptional points in optics and photonics", Science **363**, eaar7709 (2019).

[28] W. Chen, Ş. K. Özdemir, G. Zhao, J. Wiersig, and L. Yang, "Exceptional points enhance sensing in an optical microcavity", Nature **548**, 192–195 (2017).

[29] N. Hatano and D. R. Nelson, "Localization Transitions in Non-Hermitian Quantum Mechanics", Physical Review Letters **77**, 570–573 (1996).

[30] G. J. Tee, "Eigenvectors of block circulant and alternating circulant matrices", New Zealand Journal of Mathematics **36**, 195–211 (2007).

[31] S. Noschese, L. Pasquini, and L. Reichel, "Tridiagonal Toeplitz matrices: properties and novel applications", Numerical Linear Algebra with Applications **20**, 302–326 (2013).

[32] C. H. Lee and R. Thomale, "Anatomy of skin modes and topology in non-Hermitian systems", Physical Review B **99**, 201103 (2019).

[33] L. Li, C. H. Lee, S. Mu, and J. Gong, "Critical non-Hermitian skin effect", Nature Communications **11**, 5491 (2020).

[34] F. K. Kunst, E. Edvardsson, J. C. Budich, and E. J. Bergholtz, "Biorthogonal Bulk-Boundary Correspondence in Non-Hermitian Systems", Physical Review Letters **121**, 026808 (2018).

[35] N. W. Ashcroft and N. D. Mermin, *Solid State Physics* (Brooks/Cole, Cengage Learning, 1976).

[36] E. Edvardsson and E. Ardonne, "Sensitivity of non-Hermitian systems", Physical Review B **106**, 115107 (2022).

[37] B. A. Bernevig and T. L. Hughes, *Topological insulators and topological superconductors* (Princeton University Press, Princeton, 2013).

[38] M. Z. Hasan and C. L. Kane, "Colloquium : Topological insulators", Reviews of Modern Physics **82**, 3045–3067 (2010).

[39] S. Weimann, M. Kremer, Y. Plotnik, Y. Lumer, S. Nolte, K. G. Makris, M. Segev, M. C. Rechtsman, and A. Szameit, "Topologically protected bound states in photonic parity–time-symmetric crystals", Nature Materials **16**, 433–438 (2017).

[40] F. Dangel, M. Wagner, H. Cartarius, J. Main, and G. Wunner, "Topological invariants in dissipative extensions of the Su-Schrieffer-Heeger model", Physical Review A **98**, 013628 (2018).

[41] W. A. Benalcazar and A. Cerjan, "Bound states in the continuum of higher-order topological insulators", Physical Review B **101**, 161116 (2020).

[42] A. Cerjan, M. Jürgensen, W. A. Benalcazar, S. Mukherjee, and M. C. Rechtsman, "Observation of a Higher-Order Topological Bound State in the Continuum", Physical Review Letters **125**, 213901 (2020).

[43] A. Cerjan and T. A. Loring, "Local invariants identify topology in metals and gapless systems", Physical Review B **106**, 064109 (2022).

[44] A. El Hassan, F. K. Kunst, A. Moritz, G. Andler, E. J. Bergholtz, and M. Bourennane, "Corner states of light in photonic waveguides", Nature Photonics **13**, 697–700 (2019).

[45] R. Cheng, "Quantum Geometric Tensor (Fubini-Study Metric) in Simple Quantum System: A pedagogical Introduction", Apr. 5, 2013, arXiv:1012.1337, preprint.

[46] M. Kolodrubetz, V. Gritsev, and A. Polkovnikov, "Classifying and measuring geometry of a quantum ground state manifold", Physical Review B **88**, 064304 (2013).

[47] S.-J. Gu, "Fidelity approach to quantum phase transitions", International Journal of Modern Physics B **24**, 4371–4458 (2010).

[48] L. Wang, Y.-H. Liu, J. Imriška, P. N. Ma, and M. Troyer, "Fidelity Susceptibility Made Simple: A Unified Quantum Monte Carlo Approach", Physical Review X **5**, 031007 (2015).

[49] S. Peotta and P. Törmä, "Superfluidity in topologically nontrivial flat bands", Nature Communications **6**, 8944 (2015).

[50] C. C. Ye, W. L. Vleeshouwers, S. Heatley, V. Gritsev, and C. Morais Smith, "Quantum Geometry of Non-Hermitian Topological Systems", May 30, 2023, arXiv:2305.17675, preprint.

[51] R. Arouca, C. H. Lee, and C. Morais Smith, "Unconventional scaling at non-Hermitian critical points", Physical Review B **102**, 245145 (2020).

[52] P. Bruno, "Impossibility of Spontaneously Rotating Time Crystals: A No-Go Theorem", Physical Review Letters **111**, 070402 (2013).

[53] H. Watanabe and M. Oshikawa, "Absence of Quantum Time Crystals", Physical Review Letters **114**, 251603 (2015).

[54] D. V. Else, C. Monroe, C. Nayak, and N. Y. Yao, "Discrete Time Crystals", Annual Review of Condensed Matter Physics **11**, 467–499 (2020).

[55] V. Khemani, R. Moessner, and S. L. Sondhi, "A Brief History of Time Crystals", Oct. 23, 2019, arXiv:1910.10745, preprint.

[56] K. Sacha, *Time Crystals*, Vol. 114, Springer Series on Atomic, Optical, and Plasma Physics (Springer International Publishing, Cham, 2020).

[57] M. S. Rudner and N. H. Lindner, "The Floquet Engineer's Handbook", Mar. 18, 2020, arXiv:2003.08252, preprint.

[58] T. Löthman, C. Triola, J. Cayao, and A. M. Black-Schaffer, "Efficient numerical method for evaluating normal and anomalous time-domain equilibrium Green's functions in inhomogeneous systems", Physical Review B **104**, 125405 (2021).

[59] W. Cherifi, J. Carlström, M. Bourennane, and E. J. Bergholtz, "Non-Hermitian Boundary State Distillation with Lossy Waveguides", Apr. 7, 2023, arXiv:2304.03016, preprint.

[60] M. S. Rudner and N. H. Lindner, "Band structure engineering and non-equilibrium dynamics in Floquet topological insulators", Nature Reviews Physics **2**, 229–244 (2020).

[61] J. Cayao, C. Triola, and A. M. Black-Schaffer, "Floquet engineering bulk odd-frequency superconducting pairs", Physical Review B **103**, 104505 (2021).